EFFECTS OF MICROTEXTURAL INTERACTIONS OF ORGANICS AND SILICA ON SILICA DIAGENESIS

A Thesis
Submitted to
the Temple University Graduate Board

In Partial Fulfillment
of the Requirements for the Degree
MASTER OF SCIENCE
OF GEOLOGY

---

by
Justin James Morris
August 2020

Examining Committee Members:

Dr. Steven Chemtob, Earth and Environmental Sciences
Dr. Alexandra Krull Davatzes, Earth and Environmental Sciences
Dr. Bojeong Kim, Earth and Environmental Sciences

ABSTRACT

Opaline silica (opal-A) is thermodynamically unstable at surface conditions and readily transitions into opal-CT and at higher temperatures and pressures, quartz. Past work has used the temperature dependency of this phase transition for paleothermometry in opal-bearing sedimentary rocks. Those works determined that bulk concentrations of silica, organic material, and detrital minerals influenced the phase transition temperature. However, previous work only addressed the influence of these impurities on a macroscale and ignore potential microtextural interactions of silica and organic material. In this thesis, I present a set of experiments designed to characterize the effect of organic matter distribution on the opal-A to opal-CT transition in siliceous sedimentary rocks. Silica, humic acid, and mock seawater solution were loaded into Parr hydrothermal vessels as bulk sediments or in defined physical configurations (stratified or intermixed) and were heated at 200°C for up to 14 weeks. The solid products of these experiments were analyzed using X-Ray diffraction (XRD), Raman spectroscopy and Fourier-transform infrared (FTIR) spectroscopy. In organic-free experiments, the broad opal-A diffraction peak at 22° 2θ narrowed over the course of 14 weeks, suggesting increased internal ordering. FT-IR spectra showed changes in the position of the Si-O-Si stretching mode peak at 1060 cm^{-1} with silica diagenesis. Opal-CT may have been observed to occur sporadically in some stratified experiments and associated controls, but apparently did not occur in intermixed configurations. In stratified experiments, no correlation was observed between opal-A full-width half maximum and proximity to the humic acid

layer. Similarly, no trend was observed between FT-IR peak positions and proximity to humic acid. These results suggest that the presence of organic matter does play a role in inhibiting the internal ordering of opal; however, the configuration might not be a primary factor in this transition. The results of this study may be applicable to the Monterey Formation and other hydrocarbon-bearing siliceous sedimentary formations. Our results suggest that the maturation of oil reservoirs in the Monterey Formation may be constrained solely on the silica phases present.

Dedicated to the late Paxon “Pax” Morris

ACKNOWLEDGMENTS

The vast amount of support through the process of this experimentation and my time at Temple University is unmatched. Firstly, I would like to thank my academic advisor Dr. Steven Chemtob, for providing me guidance through this research and my time at Temple University, I am grateful for the opportunity to work with him on this research. I'd like to thank my committee members, Dr. Bojeong Kim and Dr. Alix Davatzes for supporting me in the construction of my experiments, as well as the speedy editing of this document. A special shoutout to the American Chemical Society Petroleum Research Fund for funding my research. I'd also like to acknowledge Dr. Jesse Thornburg for his help in the construction of my latter stages of my experiments and guidance in the Rock Lab. Additionally, I'd to thank Jim Ladd for his help with just about every problem I sent his way. I would like to give a special thank you to the Dr. Nancy Pleshko and No'Ad Shanas for their help with troubleshooting the imaging FT-IR. I'd like to recognize Colin Fitzpatrick for his help analyzing my sample through Raman Spectroscopy. To Tim Davis, I would like to thank you for the morning talks and coffee runs, they made every day at Temple University a wizard day. To Shelah Cox for the morning sanity check and making sure I never had to worry about any paperwork, an enormous thank you! A special pea soup related thank you to Paula Arenada for her help in the lab, field, and during backpacking trips. A special thank you to Katrina Souders for dragging across the finish line and helping me through the final days of my thesis. To all the graduate students from the previous year and the new graduate students, a special thank you for all the memories shared during my tenure. Finally, I'd like to make a special thank you to my fellow Masters' students, John Gallucci, Nolan Barrette and Alex Roccaro, as well as Ashleigh Kirker for the memories, laughs and dollar bets over the last two years, without all of your support this document would never have been completed.

TABLE OF CONTENTS

Page

LIST OF TABLES

LIST OF FIGURES

CHAPTER 1

INTRODUCTION

Amorphous opal (opal-A) is a silica phase lacking a defined crystallographic structure, commonly produced biogenically as the siliceous skeletons of organisms such as radiolarian and diatoms (Simpson and Volcani, 1981; MacKinnon, 1989; Heaney, 1994; Elzea et al., 1994; Liesegang and Tomaschek, 2020). Abiotically, amorphous opal-A can form as sinters from hydrothermal fluids rich in dissolved silica, via crystallization of subaqueous siliceous magma, or though volcanic ash or tuff (O'Keefe, 1984; MacKinnon, 1989; Heaney, 1994; Elzea et al., 1994; Rodgers et al., 2004, Liesegang and Tomaschek, 2020**)**. After burial, opal-A forms into an amorphous sphere from the diatom skeleton (Heaney, 1994). Opal-A then transitions into a more highly ordered crystalline structure known as opal-CT (Heaney, 1994; Tatzel et al., 2015; Liesegang and Tomaschek, 2020*)*. The transition from opal-A to opal-CT and at higher pressures and temperatures, quartz, has been shown to be a useful paleo-thermometer by using temperatures of silica phase transitions as a marker of previous environment conditions (Keller and Isaacs, 1985; Bennett et al. 1990; Behl, 1999).

Low energy environments allow for the deposition and preservation of siliceous organisms and their organic material, altering them into biogenic shales (Murata and Nakata 1974; Murata and Larson, 1975; Isaacs and Petersen, 1987; Behl, 1999). Due to the possibility of hydrocarbon repositories associated with these shales, biogenic shale formation is an ongoing topic of study as a potential economic resource (Murata and

Nakata, 1974; Murata and Larson, 1975; Isaacs and Petersen, 1987; Behl, 1999**)**. This interest is no less the case for the Miocene-aged Monterey Formation in California (Bramlette, 1946; Ingle, 1981; Behl, 1999). The Monterey Formation and overlying Sisquoc Formation are rich in diatomaceous shales and contain all phases of silica as well as hydrocarbon reservoirs (Bramlette, 1946; Ingle, 1981; Isaacs and Petersen, 1987; Dunkel and Piper, 1997; Behl, 1999).

To determine the diagenetic history of siliceous shales, many researchers have attempted to constrain the temperatures at which silica phase transitions occur, roughly between 18°C to 110°C (Kastner et al., 1977; Keller and Isaacs, 1985; MacKinnon, 1989; Bennett et al., 1990; Hinman, 1990; Lynne and Campbell, 2003). Initial studies only considered temperature and pressure as significant factors in silica diagenesis (Kastner et al., 1977; Keller and Isaacs, 1985; Bennett et al., 1990); however, evidence shows organic matter impedes the transitions from opal-A to opal-CT by acidifying the solution (Kastner and Gieskes, 1983; Isaacs 1982; Hinman 1990; Lynne and Campbell, 2003). Additionally, carbonates act as a buffer to acidification of pH allowing for less inorganic alkalinity utilization (Hinman, 1990). These previous studies focused on diagenetic changes on the bulk scale, ignoring potential microtextural variability in silica phase transitions due to heterogeneity in the distribution of organic matter.

Due to opal-CT precipitation filling void spaces of opal-A, porosity has been shown to decrease during diagenesis, with opal-A rich rocks having a porosity of 35-65%, which decreases to a porosity of 25-39% in opal-CT rich rocks (Isaacs, 1981; Hinman, 1990; Compton, 1991). The formation of quartz further reduces this porosity,

due to infilling of opaline void space and a tighter mineralogical packing (Isaacs, 1981; Hinman, 1990; Compton, 1991). Two points, however, are less clear: how distribution of organics within siliceous sediment affects diagenesis, and how organics affect the porosity of the medium on the microscale. These distributions can range from evenly distributed organics in black shale to coarse organic particulates in fluvial environments (Behl, 1999). A better understanding of microtextural interactions of organics and silica during diagenetic processes can help constrain paleo-thermometry and allow for an improved inference of hydrocarbon reservoir maturity.

1.1 Purpose of Experimentation

To better constrain the controls on silica diagenesis in the natural environment, a better understanding is required of the mechanism of silica and organic matter interaction on the microscale. This study seeks to illustrate in what way organic matter influences silica phase transitions in different physical configurations. Greater knowledge of how different organic/silica configurations influence the temperature required for phase transition will lead to a more robust interpretation of paleo-thermometry and could aid in the analysis of hydrocarbon reservoir maturation. Better understanding of these principles will allow for fine tuning of oil reservoir mapping, producing better expectations of yields from reservoirs.

In this thesis, I conducted a set of laboratory experiments designed to track the transition of opal-A in incremental timesteps through diagenesis before opal-CT precipitation has occurred. To do this, silica and a proxy for sedimentary organic matter,

in this case humic acid, were heated undisturbed for 12 weeks at 200°C in two different endmember distributions (stratified and intermixed). This setup allowed for spatially resolved mapping of silica changes with proximity to organic material. This mapping will provide a better understanding of how changes to the opal internal structure occurs before transition to opal-CT. Products of these experiments were analyzed using multiple diffraction and spectroscopy techniques to detect various signatures of diagenesis. These analyses will determine which method is most sensitive to fine changes in silica structure. Finally, this study will explore the effects of diagenetic conditions on the humic acid molecular structure.

CHAPTER 2

BACKGROUND

2.1 Silica Mineralogy

Skeletons of siliceous organisms, such as radiolarians, diatoms, and sponges, are comprised entirely of hydrous amorphous opal (opal-A) (MacKinnon, 1989; Elzea et al., 1994; Liesegang and Tomaschek, 2020). Opal-A rich sedimentary formations occur due to deposition of these skeletons of diatoms and radiolarians (Simpson and Volcani, 1981; Elzea et al., 1994; Rodgers et al., 2004; Liesegang and Milke, 2014; Liesegang and Tomaschek, 2020). After the death of these siliceous organisms, if waters are significantly undersaturated, layers of opal-A can form. Biogenic silica is also produced and recycled through plant processes on the surface (Drees et al, 1989; Heaney, 1994). These processes include the uptake of silica for plant cellular structure, with sequential release upon decay, and silica depolymerizing by some hearty grasses (Weiss and Herzog, 1978; Sangster and Hodson; 1986, Heaney, 1994). Abiotic silica can form in obsidian through quenching of highly siliceous magmas at interfaces with air or water (O'Keefe, 1984; Heaney, 1994, Elzea et al., 1994; Rodgers et al., 2004). Additional abiotic formation can be seen in tektites associated with impact events and geyserite from highly siliceous geyser fluid, as well as volcanic ash (Glass,1984; O'Keefe, 1984; Heaney, 1994).

Opal-A is classified as almost exclusively silica spheres of 1500-3000 Å in diameter or amorphous silica glass network (Jones et al., 1964; Rodgers et al., 2004;

Liesegang and Milke, 2014). Opal-A can be categorized as either hydrous opal-AG or a gel like opal-AN, also known as hyalite (Jones and Stignant, 1971; Flörke et al., 1973; Sanders, 1980; Graetsch, 1994; Rodgers et al., 2004; Curtis et al., 2019). Amorphous silica contains molecular water and hydroxl groups incorporated into their structure up to 12 weight percent (Murray and Sanders, 1980; Knauth and Epstein, 1982; Knauth, 1994; Rodgers et al., 2004; Day and Jones, 2008; Curtis et al. 2019). Opal-AG, or precious opal, is defined as repeated stacked silica spheres with molecular water groups incorporated in interspace between spheres (Jones et al., 1964; Graetsch, 1994; Rodgers et al., 2004). Regular arrangement of these spheres interference colors, leading to the visual appeal of precious opal (Sanders, 1964,1968; Graetsch, 1994 Liesegang and Milke, 2014). Hyalite, or opal-AN, incorporates the water groups into its structure during quenching of siliceous melt, forming an amorphous siliceous glass (Flörke et al. 1973; Graetsch, 1994.)

Upon burial, opal-A starts to form a microcrystalline form of opal, mineralogically comparable to silica phases cristobalite and tridymite, known as opal-CT (Heaney, 1994; MacKinnon, 1989; Tatzel et al., 2015; Liesegang and Tomaschek, 2020). Cristobalite's crystalline structure shows an alternation of three hexagonal rings, which are comprised of silica tetrahedrons (Wyckoff, 1925; Heaney, 1994). Tridymite displays a similar crystalline pattern to cristobalite; however, it alternates two hexagonal rings, creating a tunnel in the crystalline structure (Wyckoff, 1925; Heaney, 1994). Opal-CT is paracrystalline and commonly forms aggregates of lepispheres, with blades of tridymite after precipitation (see figure 1**)** (Kastner, et al. 1977; Hinman, 1990, Heaney, 1994;

Liesegang and Tomaschek, 2020). Upon precipitation of opal-CT, structural water content is dropped to about ten weight percent, with most of the water content incorporated as molecular water (Graestsch, 1994; Day and Jones, 2008).

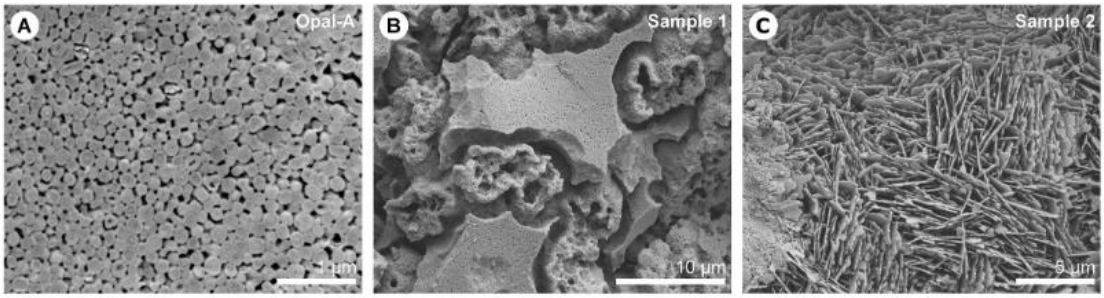

Figure 1: SEM images of: A: opal-A spheres, B: stacking of precious opal, C: lepisphere blades during the formation of opal-CT (Liesegang and Tomaschek, 2020).

After complete crystallization, opal-CT converts into highly ordered quartz, with a tighter silica tetrahedral spiral structure (Heaney, 1994). This highly packed structure is dehydrated compared to its opaline predecessors, with a water content of approximately 0.2–0.9 weight percent (Graetsch, 1994; Day and Jones, 2008).

2.2 Opal Diagenesis

Amorphous opal (opal-A) is thermodynamically unstable at surface conditions and readily changes with burial due to the increase in pressure and temperature (Simpson and Volcani, 1981; MacKinnon, 1989; Heaney, 1994; Elzea et al., 1994; Liesegang and Tomaschek, 2020). During burial, the water content of the opal is partially removed, thereby allowing for the formation of opal-CT (MacKinnon, 1989). Magnesium

hydroxide has been shown to allow nucleation of opal-CT, through attraction of the silanol group to magnesium on dissolved silica (Kastner and Gieskes, 1983; Hinman, 1998). Other heavy metal ions can also facilitate this nucleation, but they are present at low abundances in ocean waters and their effects are negligible (Kastner and Gieskes, 1983; Hinman, 1998). Using phase transition temperatures of the silica phases, researchers have attempted to utilize this diagenetic process as a system for reconstructing past geothermal temperatures (Keller Isaacs, 1985; Bennett et al., 1999). These ranges have been reported as 18°-56°C for opal-A to opal-CT, although Bennett et al. (1999) suggested a lowered initial transition to this range at 5°C, and 31°-110°C for opal-CT to quartz, with higher temperatures required when less overall biogenic silica is present in the rock (figure 2) (Keller and Isaacs, 1985; Bennett et al., 1990). Additionally, previous work has shown that further ordering of the opal-CT, as demonstrated by reduced d-spacing of the ~4.0 Å XRD peak, occurs with additional heat and time, allowing for more control on paleo-thermometry (Keller and Isaacs, 1985; Bennett et al., 1999).

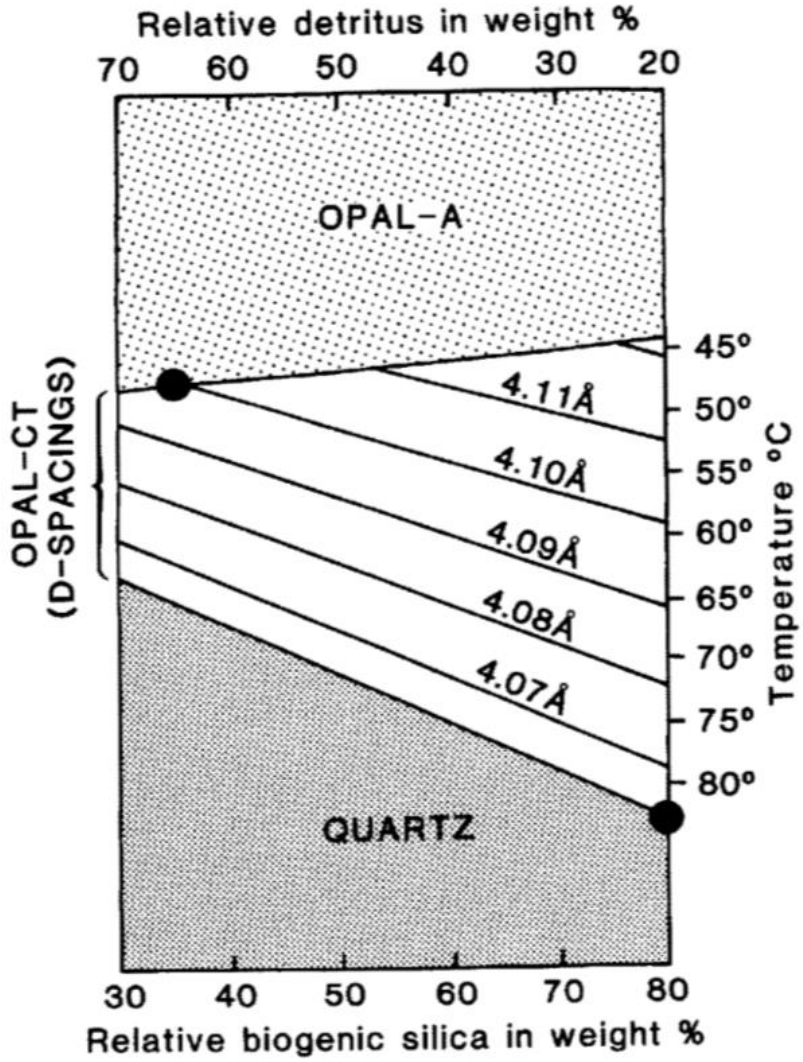

Figure 2: Transitions of opal-A to opal-CT and quartz as a function of detritus content and biogenic silica (Keller and Isaacs, 1985).

Kastner et al. (1977) demonstrated that the rate of silica diagenesis is not strictly controlled by burial pressure and temperature. The degradation of organics result in acidification of the solution, creating an environment that favors silica dissolution but not precipitation, resulting in opal diagenesis slowing in the presence of organics (Lewin, 1961; Siever and Scott, 1963; Kastner et al., 1977; Isaacs 1982; Hinman 1990; Behl,

2011). Hinman (1990) demonstrated that the addition of organic material not only inhibits the initial precipitation of opal-CT, but results in the formation of a more highly ordered opal-CT. The presence of carbonates has been shown to increase the rate of opal diagenesis (Kastner et al., 1977) as carbonates when dissolved counteract solution acidity during dissolution (Hinman, 1990).

2.3 X-Ray Diffraction Signatures of Silica Phases

X-ray Diffraction (XRD) patterns of opal-A are identified by their broad hump at 4.0 Å (figure 3) (Flörke et al, 1991; Elzea et al., 1994; Rodgers et al., 2004; Ghisoli and Marinoni, 2010; Curtis et al., 2019; Liesegang and Tomaschek, 2020). During diagenesis, this peak narrows as the opal becomes more structurally ordered (Keller and Isaacs, 1985; Liesegang and Tomaschek, 2020). Peak fitting on XRD diffractograms show that the peak usually exhibits a full-width half maximum (FWHM) of approximately 0.53 Å, with no notable difference between opal-AG and opal-AN (Curtis et al., 2019). After the formation of opal-CT, an additional peak occurs at 2.5 Å, and the broad hump at 4.0 Å narrows (Flörke et al, 1991; Elzea et al., 1994; Rodgers et al., 2004; Ghisoli and Marinoni, 2010; Curtis et al., 2019; Liesegang and Tomaschek, 2020). During further diagenesis, ordering of the opal-CT structure continues, further narrowing the peak at 4.0 Å (Keller and Isaacs, 1985; Elzea et al., 1994; Curtis et al., 2019; Liesegang and Tomaschek, 2020). However, Curtis et al. (2019) suggest opal-CT may a range of XRD patterns due to the varying complexities of opal-CT crystallography (figure 4). This

further classification suggests an additional peak may be present at 4.28 Å, as either a standalone peak or a shoulder to the 4.0 Å peak (Elzea et al., 1994; Curtis et al., 2019). Peak FWHM decreases when moving from simple opal-CT to more complex opal-CT, representing more ordering in the crystal structure (Keller and Isaacs, 1985, Rodgers et al., 2004; Curtis et al., 2019). Additionally, the 2.5 Å peak shows narrowing and is more easily distinguished from the background as the structure develops more complexity (Elzea et al., 1994; Rodgers et al., 2004; Curtis et al., 2019).

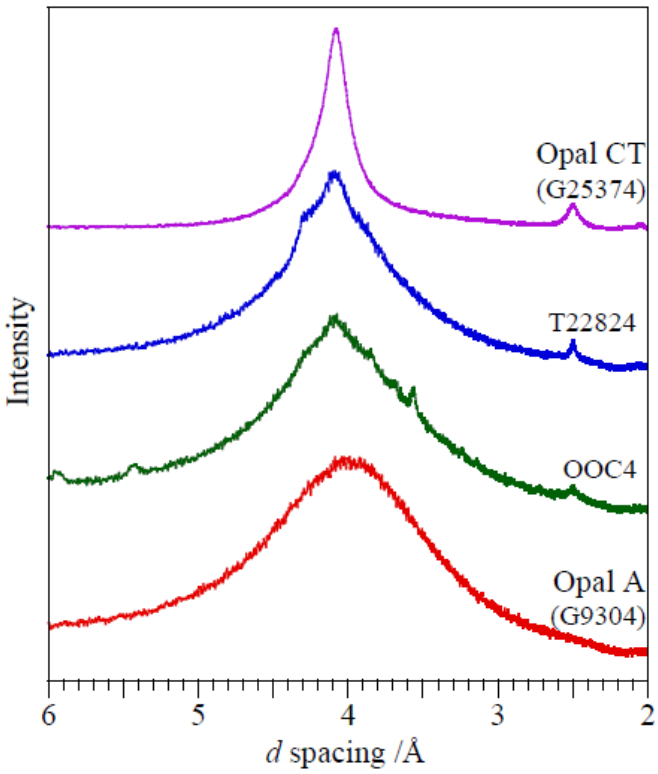

Figure 3: XRD patterns of pure opal-A to pure opal-CT. Transitional silica phases are indicated by OOC4 and T22824, with higher opal-CT content in T22824 and lower opal-CT content in OOC4.

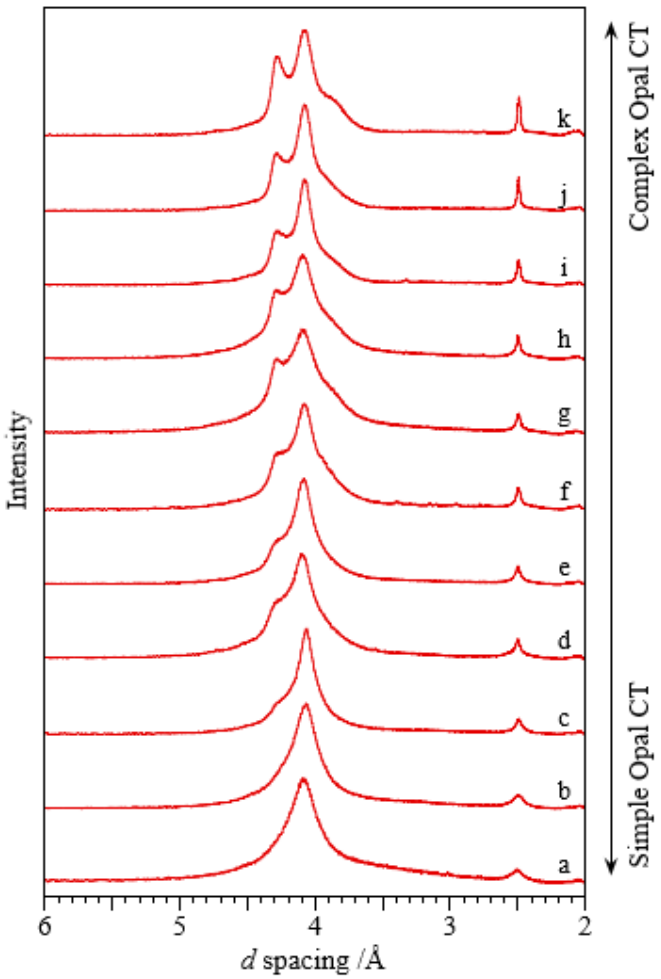

Figure 4: XRD patterns of the range of opal-CT studied by Curtis et al. (2019).

2.4 Fourier-Transform Infrared Spectroscopy

Opal-A has a characteristic peak at 1100 cm^{-1}, representing the Si-O-Si stretching mode, and a peak at 500 cm^{-1}, representing the Si-O bending modes (Lippincott et al., 1958; Rice et al., 1995; Curtis et al., 2019). Rice et al. (1995) suggest that the transition of opal-A to opal-CT in FT-IR can be indicated by a shifting of the peak centered around 470 cm^{-1} in opal-A toward a opal-CT peak located at 625 cm^{-1}, associated with

cristobalite mineralogy (Rice et al., 1995; Sodo et al., 2016; Curtis et al., 2019). However, additional work by Curtis et al. (2019) suggests this shifting is more related to the disappearance of the 530 cm^{-1} peak and is incorporated into the shoulder of the newly formed 500 cm^{-1} peak (see figure 5). All forms of opal show a peak around 789 cm^{-1} associated with the Si-O symmetrical stretch band (Rice et al., 1995; Sodo et al., 2016; Curtis et al., 2019). Both silica phases exhibit the same Si-O-Si stretch peak at 1100 cm^{-1} but at lower intensity in opal-CT (Rice et al., 1995; Sodo et al., 2016; Curtis et al., 2019). Additional bands are also associated with O-H of incorporated water in the far IR around 3480 cm^{-1} and 3650 cm^{-1} (Rice et al., 1995; Sodo et al., 2016).

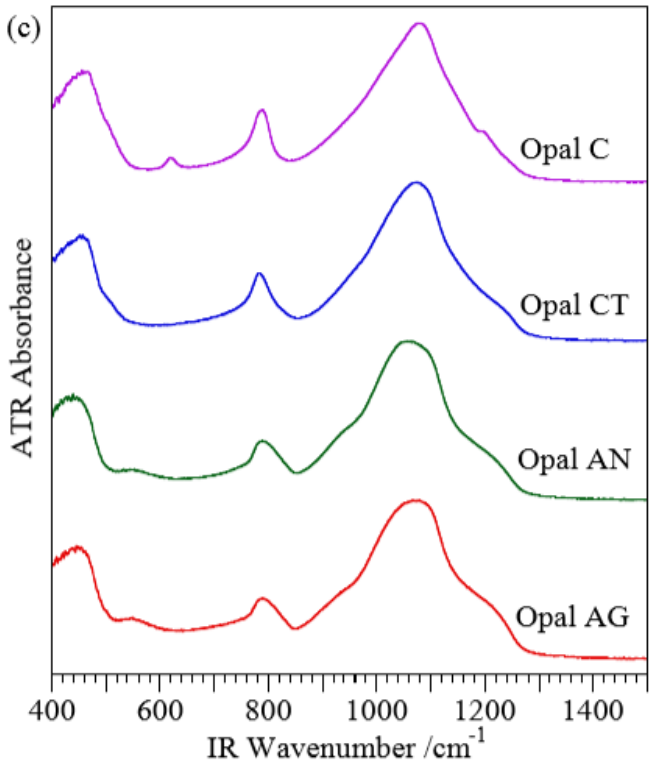

Figure 5: Mid infrared spectroscopy of various forms of opal. Opal-A groups show a broad peak around 530 cm^{-1} that is removed upon transformation into opal-CT. Opal-CT/C's 625 cm^{-1} peak replaces opal-A's 470 cm^{-1} peak after phase transition. Inclusion of a 635 cm^{-1} peak differentiates opal-CT and opal-C (Curtis et al., 2019).

2.5 Raman Spectroscopy

Raman signatures of opal peaks have proven difficult to obtain due to the high transmissive nature of opal, which causes misleading peaks due to fluorescence and oversaturation (Smallwood et al., 1997, Ostrooumov et al., 1999; Curtis et al., 2019). Silica phases generally display Raman peaks at wavenumbers of less than 1800 cm^{-1}, with a notable exception of the O-H stretching of the incorporated water near 3300 cm^{-1} (Smallwood et al., 1997). One main peak for silica phases is found between 200-600 cm^{-1}, due to Si-O-Si bending modes (Smallwood et al., 1997; Ostrooumov et al., 1999; Sodo et al., 2016, Curtis et al., 2019). These peaks shift depending on the phase, with opal-CT having a peak center at 335 cm^{-1} and opal-A having a peak center around 370-430 cm^{-1} (Smallwood et al., 1997; Ostrooumov et al., 1999; Sodo et al., 2016, Curtis et al., 2019). Smallwood et al. (1997) notes that origins of the silica content (sedimentary versus volcanic) influences peak sharpness, with volcanic opals exhibiting sharper Raman peaks. All phases of silica exhibit a symmetrical stretching of the Si-O band at 790 cm^{-1} (Smallwood et al., 1997; Sodo et al., 2016).

2.6 Porosity Changes During Diagenesis

Porosity of opal is significantly reduced after each diagenetic phase. Opal-A-rich sedimentary rocks have a porosity of 35-65%, which decreases of porosity to 25-39% in opal-CT-rich rocks (Isaacs, 1981a; MacKinnon, 1989, Herdiantia et al., 2000). Porosity

reduction from opal-A to opal-CT is attributed to the filling in of pore spaces by newly precipitated cement. With additional burial, porosity of the silica phase is further reduced to 10-15% in quartz-dominated rocks (Isaacs, 1981a; 1981b). This reduction of porosity is the result of precipitation of new silica phase, opal-CT and quartz, in void spaces within the opal-A structure (Isaacs, 1981a; 1981b). Additionally, compaction of the diatom frustule framework during diagenesis results in structural collapse, which fills-in pore space (Isaacs, 1981a; 1981b). Porosity changed during diagenesis has been shown to be independent of environment temperatures (Isaacs, 1982; Compton, 1991).

2.7 Humic Acid

Although characterized as a subdivision of humic substances, humic acid is a broad term for a complex organic compound grouping that is found throughout the natural environment (Pollack et al., 1971; Gerasimowicz et al., 1986; Fründ et al., 1989; Sirotiak and Bartošová, 2016). Humic acids can be present in many different marine sediments, including coals and shales, although they are generally found in low concentrations of 1-5% (Gerasimowicz et al., 1986; Sirotiak and Bartošová, 2016).

FT-IR analysis of humic acid is difficult due to the complex nature of the molecule. Near-IR spectra of humic acids generally display numerous peaks between 400-1000 cm^{-1}, commonly associated with C-H vibrational modes of aromatic rings, but due to the complexity of the molecule, classification has proven difficult (Naidja et al., 2002). Naidja et al. (2002) suggest that motion of the 462 cm^{-1} to 476 cm^{-1} peaks are

likely due to the shift in stretching vibration after aromatic ring breakdown. After heating of humic acid molecules, additionally formed peaks in the near infrared are the result of the aromatic ring breakdown (Naidja et al., 2002). Sirotiak and Bartošová (2016) suggest that peaks in the 600-900 cm^{-1} range shift towards higher wavenumber with humic acid breakdown. Additional z-dimensional C-H bending modes of the broken down humic acid aromatic structure are thought to be found within near 950 cm^{-1} (Gerasimowicz et al., 1986). Unrelated to the aromatic ring, carbonyl and amide bands of humic acid are present between 1720-1500 cm^{-1} (Gerasimowicz et al., 1986). Various C-H bonding modes are present in far-IR, with notable peaks around 3000 cm^{-1} (Gerasimowicz et al., 1986).

X-ray diffraction is a commonly used method to characterize materials with fixed repeating structures, resulting in general use on inorganic compounds. Organic compounds, such as humic acid, have complex structures that are broad and non-fixed, resulting in difficultly when attempting to characterize organic compounds (Pollack et al., 1971; Gerasimowicz et al., 1986; Fründ et al., 1989; Sirotiak and Bartošová, 2016). However, some have attempted to characterize these compounds using this technique (Pollack et al., 1971; Chang et al., 2006). Most notable are the peaks located at 2.89 Å, 4.34 Å, 5.29 Å, which are generally associated with the aromatic structures of humic acid (Pollack et al., 1971; Chang et al., 2006).

CHAPTER 3

GEOLOGICAL BACKGROUND

3.1 Monterey Formation

The Monterey Formation is a diatomaceous outcrop located in the greater part of the southern California basin and along the California coast (Bramlette, 1946; Ingle, 1981; Behl, 1999) (Figure 6). This mid-Miocene Monterey Formation is commonly studied for its economic value and for the presence of each diagenetic phase of silica (Ingle, 1981; Behl, 1999). After recognition of the extent of the formation's natural resources, a surge of interest in the formation increased exponentially during the 1970's, mostly in the form of oil reservoir studies (Behl, 1999). Stratigraphy of the Monterey Formation includes many examples of analogous environments to the work of this research, making it a key location to apply results of our experimentation (Bramlette, 1946; Behl, 1999).

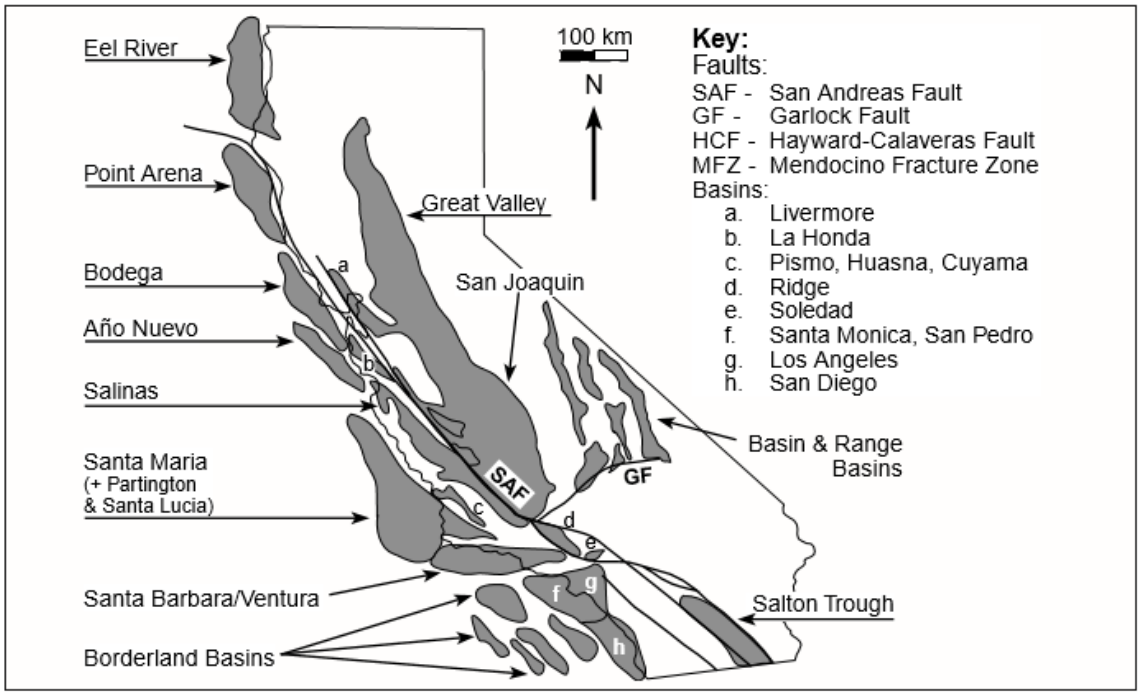

Figure 6**:** Location of Monterey Formation outcrops and tectonic zones in the greater part of California (Behl, 1999).

3.2 Formation and Locality

The Monterey Formation is typically thought to have formed from 20 Ma to 10 Ma when tectonic shifts of the North American plate transitioned the convergent boundary into a transform boundary, due to the subduction of the Mendocino triple junction (Ingle, 1981; Graham and William, 1985; Behl, 1999). Typical sediment deposition is thought to have occurred between 17 Ma and 5 Ma, with the oldest recorded sediment of the Monterey Formation (17.8 Ma) located at Naples Beach, California and the youngest recorded strata located in Verdes Hills, California, with a recorded age of ~5 Ma (Woodring et al., 1946; Ingle, 1981; Obradovich and Naeser, 1981; DePaolo and Finger, 1991; Behl, 1999). The formation exhibits alternating zones of high biogenic

productivity and detrital input, reflecting the detrital input and surface conditions favorable for siliceous life (Isaacs, 1985; 1999; Behl, 1999). Most of the siliceous input in these systems was sourced from radiolarians and diatoms in near surface waters (Isaacs, 1985; Behl, 1999). Additional inputs include organic material in the form of kerogen and marine algae and carbonates from deposited diatoms and foraminiferas (Isaacs, 1985; Isaacs and Petersen, 1987; Behl, 1999).

A key feature of the Monterey Formation is its wide variation in the compositions of silica and carbonates (Isaacs, 1985; Behl, 1999). This variation results in splitting the classification between the formation's more opal-pure coastal outcrops and more detrital-rich inland outcrops within the San Joaquin Basin (Graham and William, 1985; Behl, 1999). This high amount of silica impurity leads to a differentiation of the detrital-poor Monterey Formation located in outcrops along the coast, and the detrital-rich Monterey Formation located in the San Joaquin Basin (Graham and William, 1985). Figure 7 shows this wide variability of the composition of the Monterey Formation in the Santa Barbara and Santa Maria Basins (Isaac, 1985; Behl, 1999).

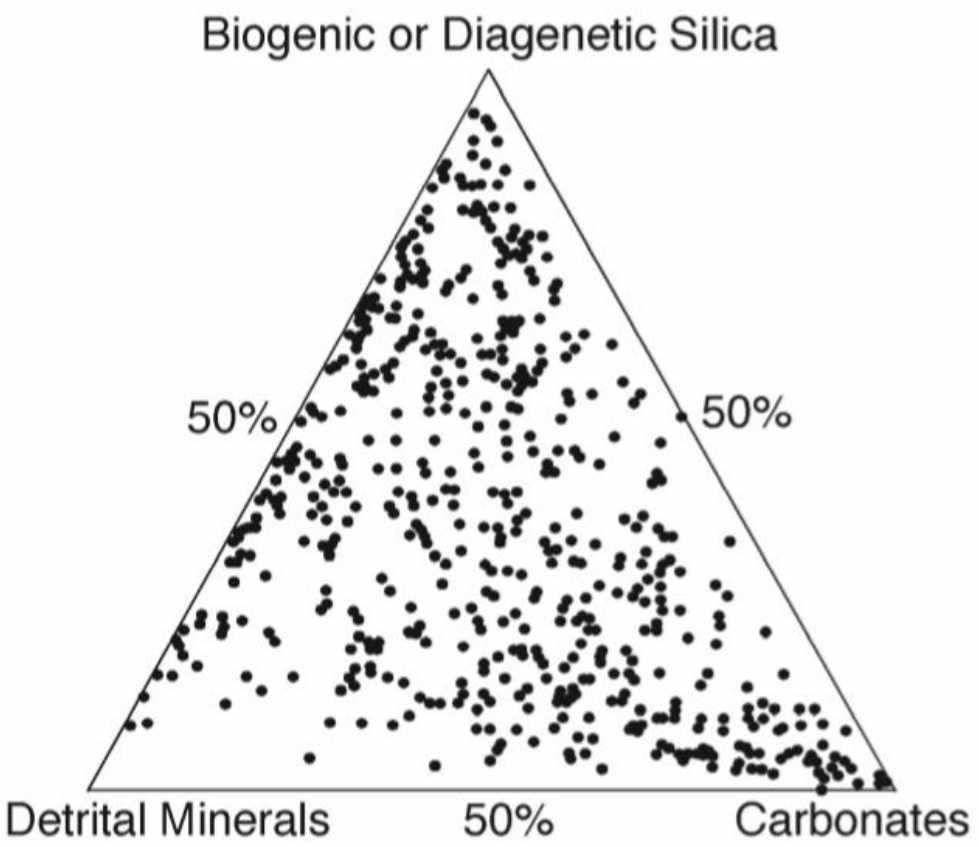

Figure 7: Sedimentary composition variation of rocks in the Monterey Formation in the Santa Maria and Santa Barbara Basins (Isaacs, 1985; Behl, 1999).

Most of the Monterey Formation was deposited in the bathyal plane, with the majority deposited in the middle bathyal (1500-2300 m) to the upper middle bathyal (500-1500 m) zone/plane (Ingle, 1973; 1980; Isaacs, 1990; Behl, 1999). Non-annual varve-like laminations with preserved organic material are commonly found throughout the Monterey Formation (Ingle, 1973; 1980; Isaacs, 1990; Behl, 1999). These laminations appear to be rhythmic, suggesting fluctuations of oxygen levels with increasing frequency upward through the Monterey Formation (Behl and Kennett, 1996; Behl, 1999). The preservation of this material and additions of anaerobic foraminifera indicate periods of anoxic conditions in the Monterey Basin, allowing for preservation and burial of

hydrocarbons (Ingle 1973; 1980; Isaacs, 1990; Behl, 1999). This upward trend suggests a depletion of the oxygenated waters and a shallowing of the basin (Isaacs et al., 1996; Behl, 1999).

3.3 Economic Value

A key economic component of the Monterey Formation is its ability to store hydrocarbons; in some sections, total organic carbon is as high as 23% (Isaacs and Petersen, 1987; Behl, 1999). Most of the Monterey Formation, however, averages around 2% to 5% total organic carbon, with 2% being the minimum organic carbon for feasible drilling (Isaacs and Petersen, 1987; Behl, 1999). Additionally, petroleum reservoirs occur within the Monterey formation through the migration of tar and asphalt seeps in the fracturs of the strata (Bodnar, 2018). Exploitation of these reservoirs occurs mostly in the San Joaquin Basin, as well as at onshore and offshore drilling in the Santa Maria Basin (Crawford, 1971; Behl, 1999). These basins are ideal for extraction because of the highly porous nature of opal-A sediments (Behl, 1999). Although highly studied, it is estimated that an additional 5.96 billion barrels of oil, or 6.32 trillion cubic feet of natural gas, are undiscovered in the formation in the outer continental shelf region (Dunkel and Piper, 1997; Behl, 1999).

Most organic compounds found in the Monterey Formation are predominantly marine algae with some input of kerogen (Magoon and Isaacs, 1983, Graham and Williams, 1985; Behl, 1999). However, due to the marginal maturity of the hydrocarbons

in the Monterey Formation as well as the presence of kerogen and migration of hydrocarbon reservoirs, determining the maturation level of the hydrocarbons in the formation has proven difficult (Dunham et al., 1991; Behl, 1999). In addition, some reservoirs are not utilized due to high carbonate input or large sandstone interfinger in proximity to the reservoir (Behl, 1999).

3.4 Silica Diagenesis in the Monterey Formation

The Monterey Formation contains the entire diagenetic sequence of silica, making the formation an ideal environment for the research of silica diagenesis (Bramlette, 1946; Behl, 1999). Although individual zones of each silica phase are present in the Monterey Formation, most phase transitions occur through large sections of the strata (< 300 m) (Isaacs, 1982; Behl, 1999). These massive sections exhibit interbedding of various silica phases and lithologies through these transitional zones (Isaacs, 1982; Behl, 1999). On a macroscale, these zones lack lateral continuity, indicating highly variable depositional environments (Bramlette, 1946; Murata and Larson, 1975; Behl, 1999). Figure 8 illustrates the lithological phase differences through the Monterey Formation along the Santa Barbara Coastline (Behl, 1999). Finally, purity of silica in the Monterey Formation has been recorded in sections that are marked by mature diagenesis of siliceous material (Bohrmann et al., 1994; Behl, 1999).

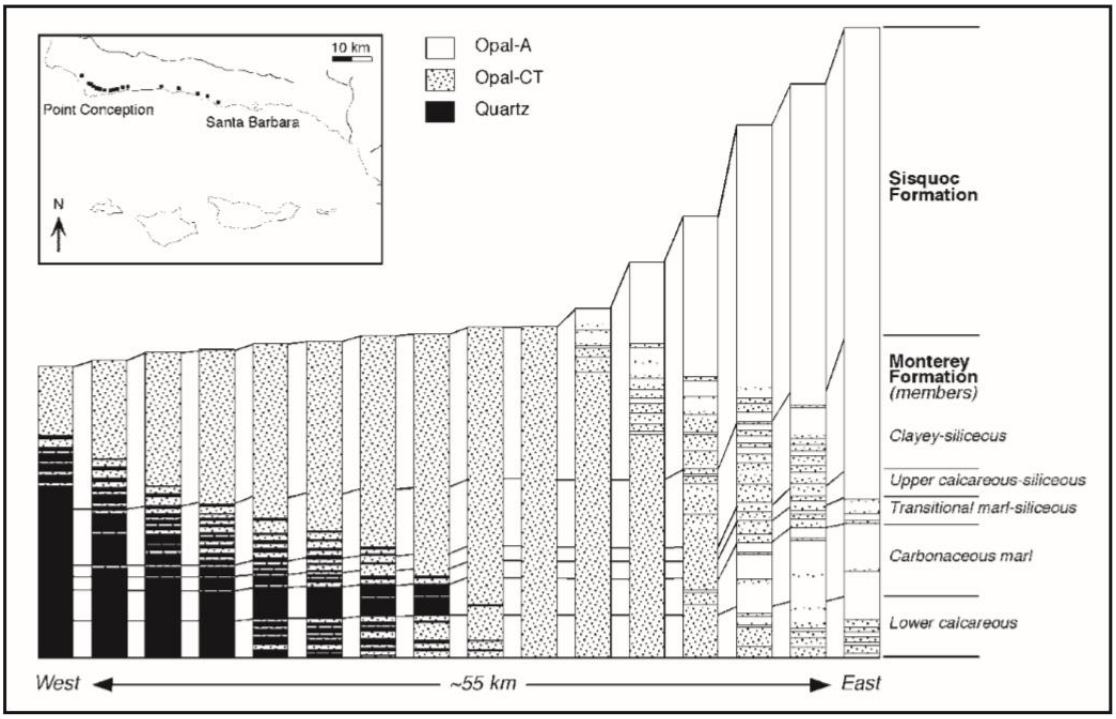

Figure 8: Silica phase distribution across the Monterey Formation outcrops along the Santa Barbara Coast (Behl, 1999).

CHAPTER 4

HYPOTHESES

1. Opal dissolution-reprecipitation reactions will be hindered by its proximity to organic material, leading to microtextural heterogeneity in organic-bearing siliceous sediments. Specifically, we hypothesize that:
    a. In stratified experiments, less opal-CT precipitation will occur in locations closer to the organic layer, compared to locations distal from the organic layer.
    b. Due to the immediate interactions with organic material, intermixed experiments will exhibit less overall opal-CT precipitation compared to stratified experiments.
2. Ordering of the opal-A 4.0 Å XRD peak in stratified experiments will occur more readily at locations most distal from organic material. Additionally, intermixed examples will demonstrate less order of the opal-A 4.0 Å peak compared to stratified experiments.
3. Opal-CT precipitation occurring in stratified experiments will exhibit more initial ordering of the 4.0 Å peak at locations closest to organic material, compared to more distal locations. Intermixed opal-CT precipitation will have more initial ordering compared to stratified opal-CT.

CHAPTER 5

METHODS

5.1 Bulk Silica Diagenesis Experiments

To determine the diagenetic window for opal-A to opal-CT, a set of seven individual bulk hydrothermal experiments was designed in the absence of organic matter. These experiments were conducted in Parr hydrothermal vessels (Parr Bomb), which can withstand high temperatures and pressures. Alfa Aesar 230-400 mesh silica gel was weighed to either 0.325 g or 0.600 g for the 23 ml or 45 ml Parr Bomb, respectively. Once properly weighed, the silica gel was gently poured into the Parr Bomb and submerged in 16 ml or 30 ml of mock seawater solution for the 23 ml or 45 ml Parr Bomb, respectively. Mock seawater, with a 50:1 fluid to cation ratio, was synthesized to mimic the solution used by Hinman (1990). As described in Hinman (1990), the cations, magnesium and sodium, are essential for the precipitation of opal-CT. This was achieved by adding 27.9 g of Acros Organics $MgCl_2$ *$6H_2O$ and 10.98g of Fisher Chemical NaCl to 1 L of MilliQ water. The combination was then shaken vigorously to dissolve and homogenize the solution. The pH of the solution, tested using an Orion Star A11 pH Meter by Thermo Fisher, was determined to be 6.85. The Parr Bombs were then tightened to ensure no evaporated solution escaped from the container during experimentation.

Samples were then placed in a Lindberg Blue M vacuum oven and allowed to gradually heat to 200°C over the duration of a day. The experiments remained heated and undisturbed at 200°C for various time frames ranging from one week to 14 weeks, where one of the seven individual experiments were removed at various timesteps. Upon completion of the experiment, the Parr Bombs were removed from the oven and allowed to cool to room temperature over the course of one to two days.

Centrifuging was performed to separate the solids from the experimental solution and to attempt to remove most precipitated salts that may have formed during heating. To accomplish this task, the silica gel and solution were extracted and placed into 20 mL centrifuge containers. These containers were then placed in an Allegra X-30R centrifuge using the F850 rotary. Samples were then centrifuged at 11400 RPMs at room temperature for 30 minutes. Upon completion of centrifuging, an additional 15 minutes was allotted to allow settling of any dissolved silica. The supernatant was then gently pipetted out of solution and replaced with 5 mL of milliQ water. This centrifuging process was repeated two more times with fresh milliQ water for each iteration.

Upon removal of solution after final centrifuging, the sample was poured into a weighing boat and covered to allow for overnight air drying. Once the powder was dried, it was poured into a labeled glass vial for storage. This powder was analyzed on bulk FT-IR and XRD to determine characteristic changes in the silica gel and to determine if opal-CT precipitated.

5.2 Spatially Resolved Diagenesis Experiments

The goal of this experimental series was to investigate of the effects of humic acid distribution on silica and organic diagenesis. This experimental goal required a setup where introduction and removal of fluid at the beginning and end of the experiment did not alter the configuration of the experimental solid. While all these experiments featured the same humic acid and silica bulk ratio, two endmember distributions were employed to investigate effects of heterogeneity. In one set of experiments, referred to as "stratified" below, organics and silica were arranged in separate horizontal layers. In another set of experiments, referred to as "intermixed", the silica and organic material were intimately mixed, creating a near homogenous distribution. Both setups had an organic free sample referred to as "control".

Experiments were constructed to maintain a closed environment, in which silica and organic matter were subjected to high temperatures and pressure, through the duration of the trials. This setup was first achieved by cutting polytetrafluoroethylene tubes (hereafter referred to as Teflon) into 2-inch segments using a pipe cutter. Teflon was chosen to withstand the high temperature and pressures required to conduct these experiments. Teflon tubing (1/4" ID) was used to create three different experimental vessels: intermixed silica and organics, stratified silica and organics, and a controlled experiment (silica gel only).

To maintain constant fluid submergence for the experiments during experimental setup, filter caps were constructed for each end of the experimental tubes. These filters were fashioned by using two open tube caps and adhering a Whatman 2-micron diameter

filter paper between each piece, using pressure to keep the caps together during adhesion. After the caps were adhered together, a layer of glue was applied around the outer diameter of the contact point to create a sealant around the filter (Figure 9). Using a straight-edge razor blade, the end of the filter caps was shortened to approximately 1/5" to reduce loss of silica during experimental setup while also ensuring enough cap to create a strong seal around the Teflon tubing.

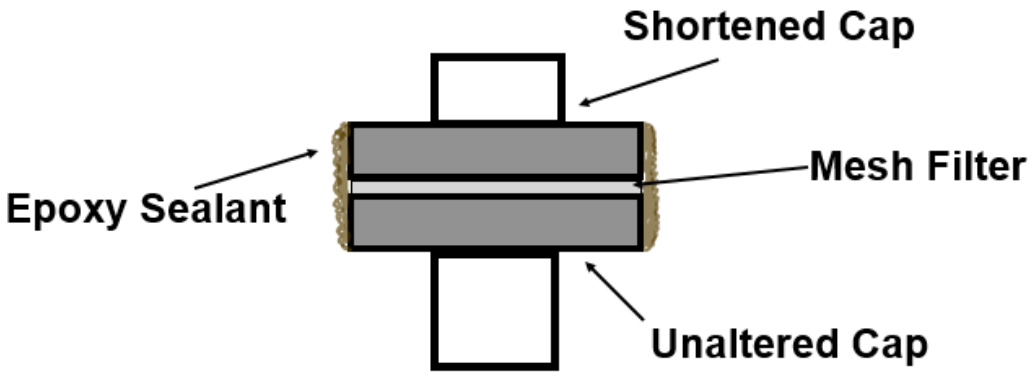

Figure 9: Filter caps used at the ends of the experiments. A 2-micron diameter filter mesh was glued between each end cap to filter only fluid out of the experiment. Additional epoxy was applied around the outside of the cap to ensure no leaking occurred.

After the equipment was assembled, initial setup of experiments started with one end of the Teflon tubing capped with a filter and leaving the other end exposed to open atmosphere. To prevent any leaking, a thick layer of parafilm was wrapped around the base of the experiment. Alfa Aesar 230-400 mesh silica gel was weighed to approximately 0.552g, or enough to fill more than half of the Teflon tubes during experiments. In the control and stratified experiments, this silica gel was poured into the Teflon tubing and tamped down with a metal tamping device. For stratified experiments,

additional organic material, in the form of Frontier Scientific 98% humic acid, was added to the top of the silica and tamped down. This organic material was weighed to equal approximately 10% of the combined mass of the silica gel and organic material. In intermixed experiments, silica and organic material were weighed identically to methods previously stated; however, they were mixed intimately before being added to the Teflon tubing (Figure 10).

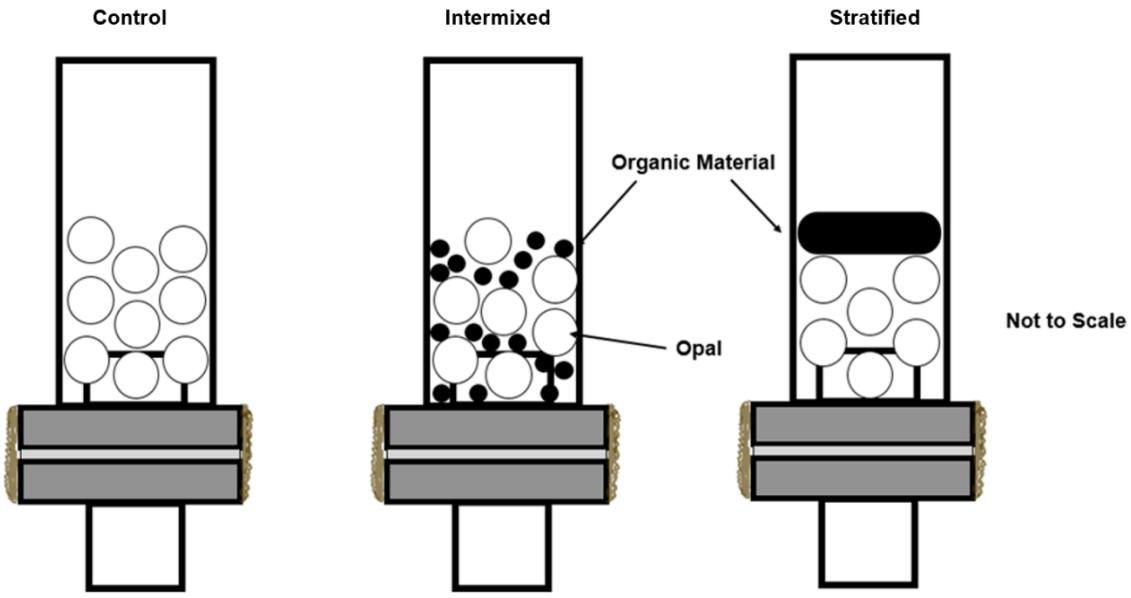

Figure 10: Experimental setup of three different arrangements. Control experiments were only silica gel. Intermixed experiments contained intimate mixture of silica gel and organic material. Stratified experiments have a layer of humic acid layered over silica gel.

After initial setup, a luer-lock plug was added to each experiment and wrapped in parafilm. Mock seawater solution was added to a luer-lock syringe and locked into the

luer-lock cap (Figure 11). The solution was gently pushed through the experiment at a steady and controlled pace. Once bubbles formed through the filter on the bottom of the experiment, solution pushing was stopped, and the syringe was removed. The parafilm covering the luer-lock was cut using a razor and the luer-lock cap was gently removed using a wiggling motion. A high temperature rubber cap was then placed over the experiment by squeezing the cap before adding to the tube in order to prevent bubbles.

The filter was removed from the base of the experiment by inverting the vial and gently removing the filter. Due to the nature of silica expansion in water, the removal of this filter does not cause silica to pour out of the tubing, and no noticeable shift occurred. Using the same squeezing technique described above, the rubber cap was added to the exposed end of the experiments and inverted back to its original orientation to create a sealed experiment (Figure 12). This process resulted in a slight loss of silica (10-15% silica loss by mass) in the filter cap at the base of the experiment due to silica expansion around the cap. This silica loss was negligible for this experiment as the area of interest was the contact between the silica and organic material, which was distal to this loss.

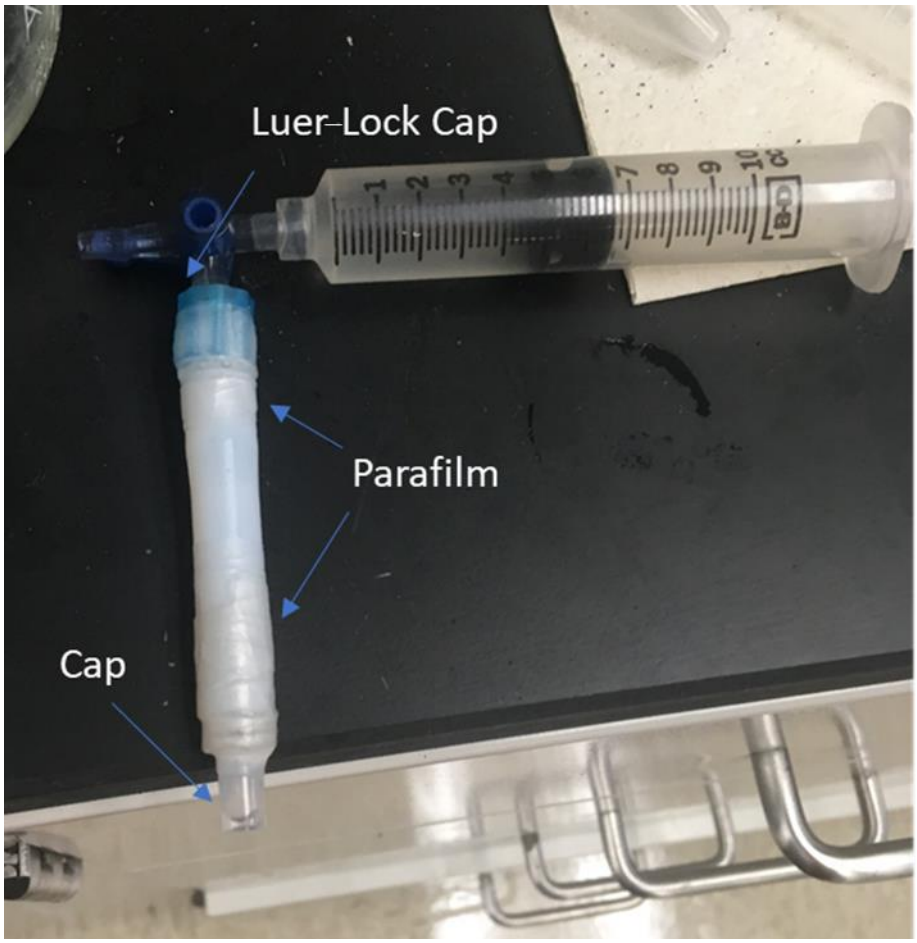

Figure 11**:** Experimental setup with luer-lock on top of experiment. Parafilm was wrapped on both ends of the experiments to prevent leaking of solution during fluid pushing. Fluid was pushed through until bubbles formed at the base of the cap.

Using a razor blade, an up direction was etched into the Teflon tubing, as well as a letter to identify the experiment. An etched “C” indicated a controlled experiment and an etched “S” and “I” indicated stratified and intermixed experiments, respectively.

Two of the assembled tubes (a control and a stratified/intermixed) were placed into a 40 ml Teflon-lined Parr Bomb and submerged in 20ml of mock seawater solution. The Parr Bombs were then sealed tightly to prevent off-gassing of solution in each experiment. These experiments were gradually heated in a Lindberg oven to 200°C over a

24-hour period. The experiments were then allowed to remain heated at 200°C for 12 weeks.

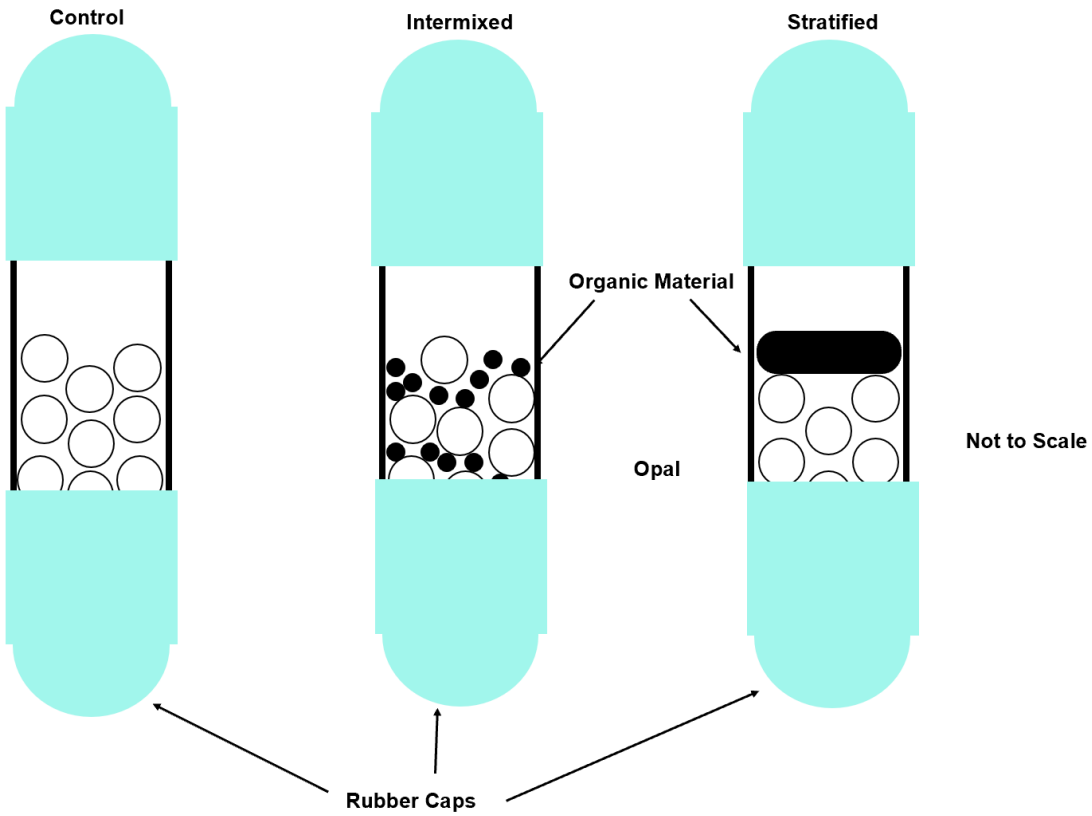

Figure 12: Completed experimental setups. Rubber caps closed each end of the experiments. Three different experimental setups were created: control, intermixed, and stratified.

5.2.1 Preparation of Half Section Mount of Experiments

Upon completion of experiments, Teflon-lined Parr Bombs were pulled from the oven and allowed to cool at room temperature. Samples from each container were delicately removed using tweezers and placed into a Styrofoam™ tray. Original orientation of each experiment was preserved by placing the experiments upright, and the

tray was marked with the experiment name and which Parr Bomb they were removed from. The rubber caps of each experiment were gently removed and discarded.

The samples were then placed in a freezer, allowing the solution to crystallize over a 24-hour period. This crystallization freezes the experiment in place and allows for the now frozen setup to be manipulated without disturbing the spatial resolution of the silica and organic configurations. Upon completion of freezing, a single experiment was removed from the tray and placed horizontally in a vice clamp to hold in it in place. The experiment was placed so that half of the Teflon was exposed above the vice (See figure 13).

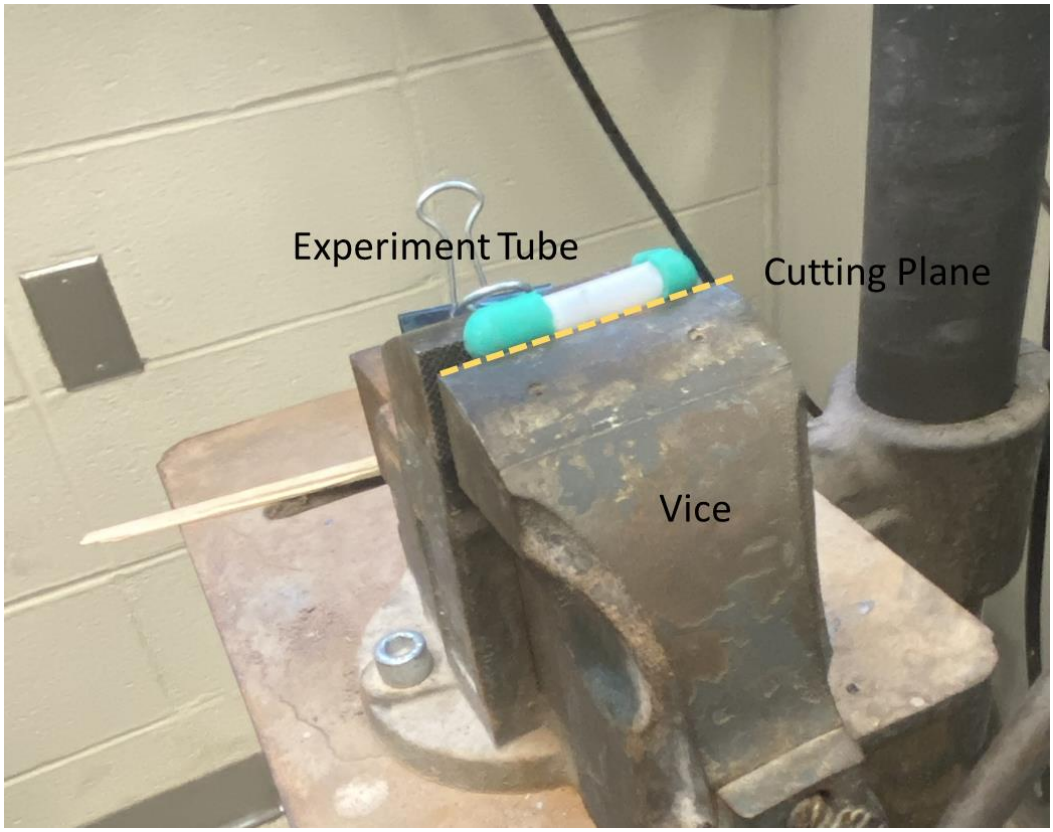

Figure 13: Experimental tubes in vice clamp before cutting sample. Sample were loaded into the clamp, while solution was still frozen, then gently cut across the cutting plane, exposing both halves.

A straight-edge razor was then delicately guided along the clamp for the length of the Teflon, cutting the tube evenly and exposing two open faces of the experiment. Each half of the experiment was placed in a premade mold of the Teflon tubes to prevent shifting. Due to the experiment being frozen before processing, the silica and organic configuration was held in place during the cutting procedure however, haste was needed during this processing due to quick thawing of the ice which could have resulted in shifting of the experiment setup. The experiment ID was marked on the mold of the experiments. One of the experiment halves was marked for XRD analysis and processed immediately, while the other half was dried in a Quincy Lab 40 E Lab Oven at 100°F for two days and was used for Raman analysis. Excess frozen solution above the experiments were gently removed, and cranoacrylate glue was used to "close off" each end of the tubing, preventing shifting during analysis. In stratified experiments, the contact between silica gel and humic acid was marked as 0.0 cm. Additional markings in the stratified experiments were made at 0.1cm, 0.2 cm, 1.0 cm, and 2.0 cm from the contact in the silica gel.

Half of the experimental solids were dedicated for use in bulk XRD and FTIR spectroscopy. Samples were removed at various locations in proximity to the humic acid layer. Sampling was done by pipetting, in a slow clockwise motion, approximately 0.2 µm of silica (and organic material in intermixed experiments), resulting in a 1 mm-diameter crater in the silica gel. These samples were then transferred to a small 2 ml glass vial and allowed to dry in a Quincy Lab 40 E Lab Oven at 100°F overnight. In intermixed

and control experiments, material was pipetted from two centralized locations of the experiment. In stratified experiments, material was pipetted from the center of the humic acid layer, from the organic-silica interface, and 0.1 cm, 0.2 cm, 1.0 cm, and 2.0 cm from the silica-organic interface. After samples were removed, the remaining samples were then placed in the Quincy Lab 40 E Lab Oven at 100°F overnight to dry.

To obtain better resolution of the silica and organic interaction, more precise analysis near the interface of the silica gel and humic acid layer was later required. Three additional samples were collected for each experiment: one at the contact, one at 5 mm, and one at 10 mm. These were collected with a 1 µL pipette tip and via gentle "scraping" of the dry power at each increment.

5.3 Raman Spectroscopy

Due to the transparent nature of silica, Raman spectroscopy proved to be difficult for characterizing heterogeneity in the experimental products. This difficulty manifested in the form of artifacts of any holding tray used underneath the silica gel and green and near-ultraviolet wavelengths. It was determined, however, that using the 1 µm spot size of 785 nm laser (red), coupled with a non-Raman active copper plate, gave a measurement of silica and nearby silica gel, allowing for an averaged reading over the scanned area. This was determined to be sufficient for the scope of this study.

Analysis of initial silica and silica from bulk experiments was completed by using a Horiba LabRam. A 785 nm laser with an acquisition time of 30 seconds over through six accumulations was used for each sample. Bulk silica samples were placed on a piece of copper and analyzed over a range of 100–1500 cm^{-1}. Scans were completed for each iteration of samples (1-week, 4-week, 6-week, 8-week, 10-week, and 12-week) to map the changes in the Raman signatures during diagenesis. Oversaturation was an issue for some samples and therefore required the intensity of the laser to be reduced to 50%.

5.4 X-Ray Diffraction Analysis

X-Ray Diffraction was performed on a Bruker d8 Cu Kα sourced X-ray diffractometer. Initial silica and samples from bulk diagenetic experiments were placed into a zero-background Si sample holder flush with the sample tray to prevent artifacts during analysis. A sample fin was added to prevent air scattering of x-rays during analysis at low angles. Each sample was examined for 2935 one-second steps between 10 and 70 2θ. XRD experiments used a Soller slit and Ni filter to reduce interference. Background removal was completed using the DIFFRAC.EVA software package.

Due to the low volume of materials produced from the spatially resolved diagenetic experiments, a zero-background silicon sample holder was used for XRD analysis. These experiments used the same setup with a Soller slit, Ni filter, and sample fin. Fine adjustment of the sample fin was needed to prevent oversaturation of the x-ray detector whilst also allowing for analysis at low two-theta measurements. These experiments were performed over the same 2θ range of 10°-70° 2θ, but for 2935 2.5-

second timesteps. These significantly longer timesteps allowed for improved signal-to-noise ratios at the cost of increased analysis times.

5.5 Attenuated Total Reflectance Fourier-Transform Infrared

Bulk analysis of samples on Fourier Transform-Infrared was completed on a Nicolet iS50 FT-IR using the attenuated total reflectance (ATR) setting. Sample powder was placed on the ATR diamond crystal to create a film of approximately 1 mm of powder. The sample compressor was then lowered until a firm contact was made with the sample. ATR was completed after 32 scans using a resolution of 16. Sample backgrounds were collected and removed from resulting experiments to ensure a pure signature. Automated alignment of the ATR mirrors was required before each analysis to prevent artifacts from appearing in the desired collection area.

5.6 XRD Data Processing

To determine how opal-A's crystal structure was changing over time, peak fitting was employed on XRD patterns to determine the FWHM of the large opal hump at 22° 2θ in each experiment. Peaks were fitted as a Gaussian-Lorentzian curve, allowing for adjustment of bell shape. Peaks were adjusted first by hand and then fine-tuned with the use of Microsoft Excel's solver add-on under guided parameters intended to constrain the peak locations and intensities. Additional filtration functions were used in diffractograms with large halite peaks to remove those peaks, allowing for analysis of the broader opal features.

In spatially resolved diagenetic experiments, the total mass of experimental solids was low and precipitated salts could not be removed by centrifugation. This lack of filtration resulted in large halite peaks that overwhelm opal diagenetic signals, resulting in the need to remove peaks for a clearer signal of opal diagenesis. Halite peaks at 27° 2θ, 31° 2θ, 45° 2θ, and 56° 2θ were removed by masking the peak signal with background values. Other notable halite peaks of 54° 2θ and 67° 2θ were not removed in resulting diffractograms due to their low intensity.

CHAPTER 6

RESULTS

6.1 Bulk Diagenetic Experiments

6.1.1 X-Ray Diffraction Results

The FWHM values of the broad opal-A peak centered near 22° 2θ for each sample are presented in table 1. The stock silica gel exhibited a FWHM of 6.98° 2θ. This FWHM is reduced by 0.56° 2θ after one week of heating to 6.42° 2θ. This reduction is furthered over the following three weeks by 0.20° 2θ to 6.23° 2θ after four weeks of heating. After an additional two weeks of heating, the peak is slightly broadened to 6.45° 2θ. Finally, over the remaining six weeks, narrowing of the peak continues until 12 weeks, where the FWHM becomes 5.51° 2θ. Additional two weeks of heating results in a further narrowing of the peak to 5.47° 2θ at 14 weeks. The shortening of the FWHM can also be seen in figure 14**,** with an associated trendline, with an R^2 of 0.82, illustrating values shifting toward a FWHM. Due to the lack of broad 22° 2θ peak in a pure opal-CT standard the FWHM was not determined for that sample.

Time	FWHM	Δ FWHM
Opal-A	6.98	0.00
Week 1	6.42	-0.56
Week 4	6.23	-0.20
Week 6	6.45	0.23
Week 8	6.40	-0.05
Week 10	6.04	-0.36
Week 12	5.51	-0.53
Week 14	5.47	-0.04

Table 1**:** Full-width half maximum (FWHM) of each experimental result. Changes in FWHM is compared to the previous week's iteration, with negative values indicating narrowing and positive values indicating broadening.

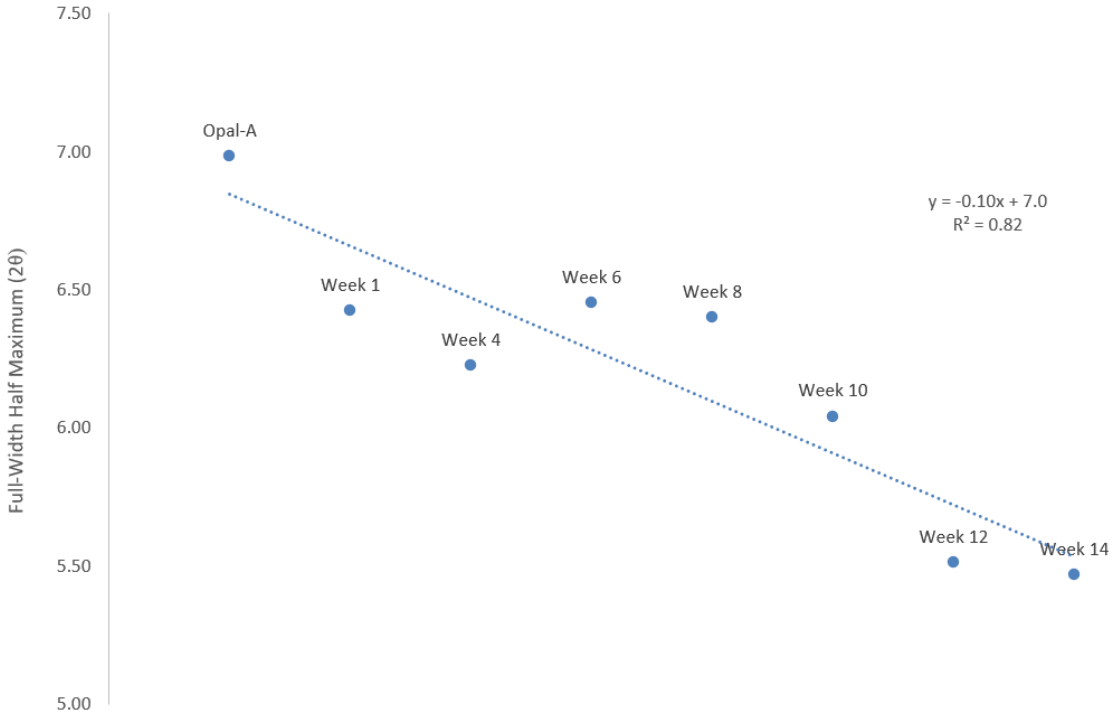

Figure 14**:** Full-width half maximum of the 22° 2θ of each sample. Trendline gives an R^2 value of 0.8, with values trending toward narrowing peaks.

6.1.2 Fourier-Transform Infrared Results

FT-IR spectra of all analyzed silica samples featured peaks near 445 cm^{-1}, 800 cm^{-1}, and 1060 cm^{-1}, corresponding to the Si-O bending mode, Si-O symmetrical stretching mode, and Si-O-Si stretching mode, respectively. Modest shifts in the positions of these peaks were observed with increasing lengths of diagenesis. Stock silica gel featured a peak corresponding to the Si-O bending mode at 444.5 cm^{-1}. After heating has occurred, most values range from 445 cm^{-1} to 449 cm^{-1} with a slight deviation toward high wavenumbers for the 10-week sample at 452 cm^{-1} and the 14-week sample at 441 cm^{-1}. These values can be compared to the opal-CT collected from Venture Hill California, which was provided by George Rossman of the California Institute for Technology, a 468.6 cm^{-1} for the first peak. These trends can also be seen in figure 15 and are present in table 2. Individual graphs of each measurement and compiled graphs are presented in appendix C.

The silica gel standard displays the second symmetrical stretching mode peak at 796 cm^{-1}. After heating of the samples from 1-10 weeks, samples do not appear to show any initial trend toward the opal-CT, with a peak located at 786 cm^{-1}. After 12 weeks of heating, there is a slight shift toward shorter wavenumbers to 793 cm^{-1} but is reverted at 14-weeks. These values are presented in table 2 and are also present in figure 16. Individual graphs of sample measurements are presented in appendix C.

The Si-O-Si stretching mode occurs at approximately 1060 cm^{-1}. The opal-A standard has the Si-O-Si stretching peak location at 1051 cm^{-1} compared to the diagenetic opal-CT with a peak position at 1070 cm^{-1}. After a week of heating the silica gel, the peak location shifts to 1058 cm^{-1}. After further heating, this peak shifts again to 1063 cm^{-1} and stabilizes for the next eight weeks. After 12- and 14-weeks of heating, the sample shifts to lower wavenumbers to 1054 cm^{-1}, reversing the trend. These values are presented in table 2 and are displayed in figure 17. Individual graphs of sample measurements and compiled results are presented in appendix C.

Peak Locations	450 cm^{-1}	800 cm^{-1}	1060 cm^{-1}
Opal-CT	469	787	1070
Opal-A	445	796	1051
Week 1	448	795	1058
Week 4	448	796	1063
Week 6	449	796	1062
Week 8	448	796	1062
Week 10	452	797	1062
Week 12	449	793	1054
Week 14	441	795	1054

Table 2**:** Peak locations of heated samples compared to opal-A and opal-CT standards. Peak locations were located around approximately 450 cm^{-1}, 800 cm^{-1}, and 1060 cm^{-1}.

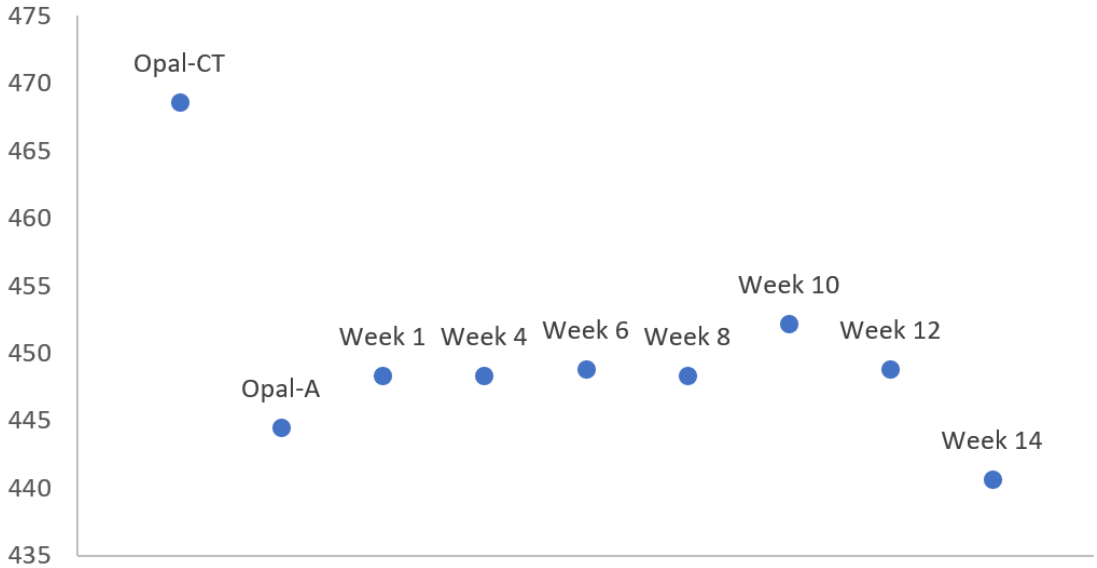

Figure 15**:** Bending mode peak locations for each sample iteration.

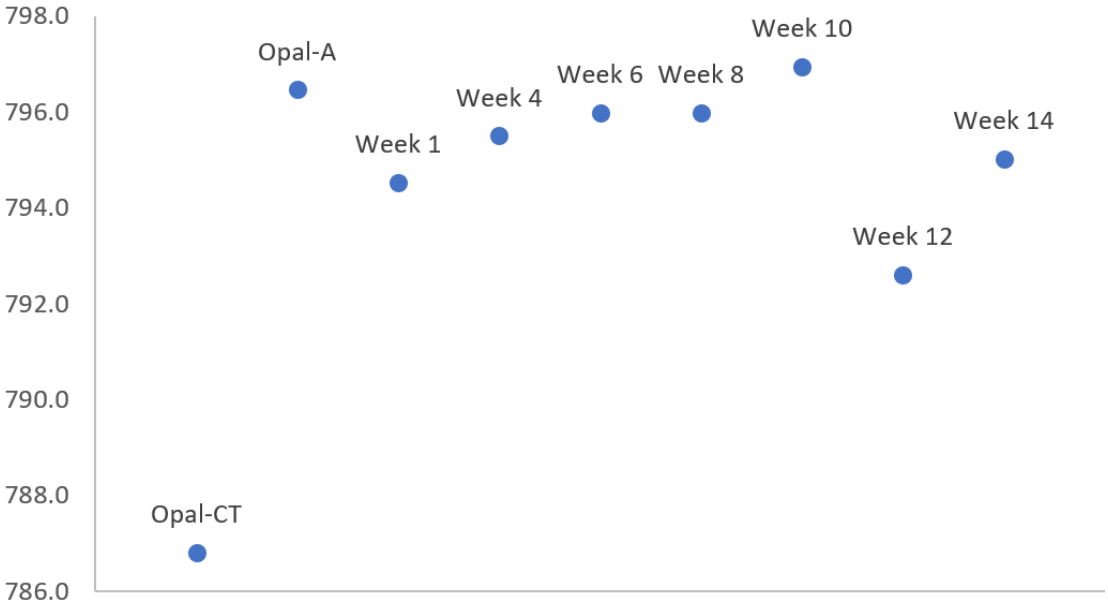

Figure 16**:** Si-O symmetrical stretch mode peak locations for each sample iteration.

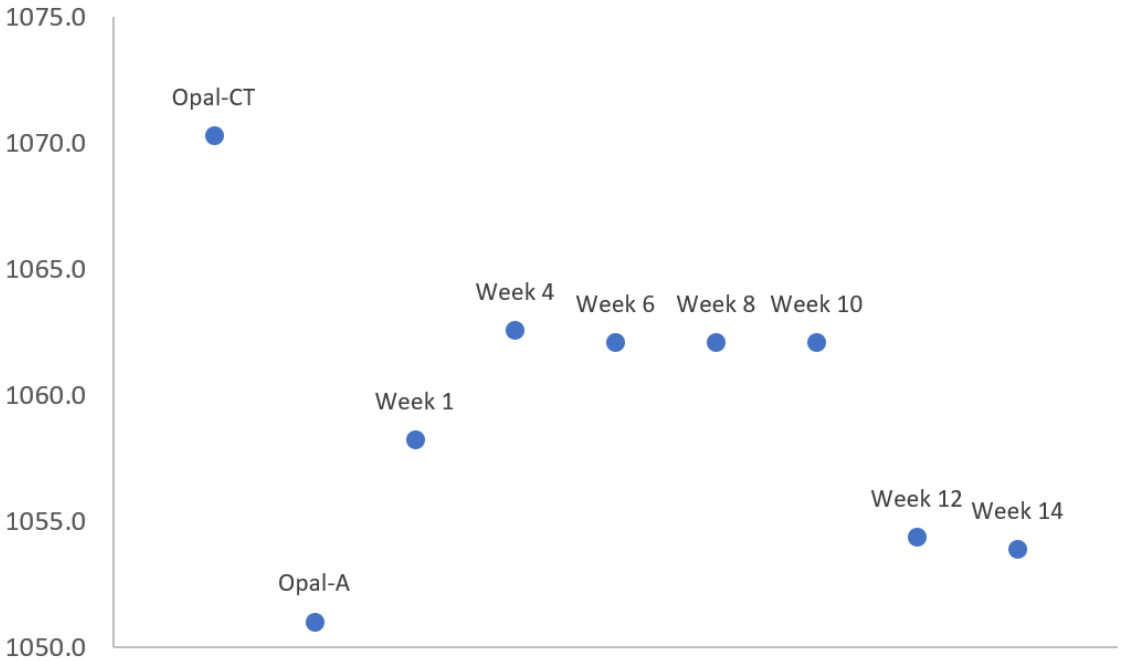

Figure 17**:** Si-O-Si stretching mode peak locations for each sample iteration. Samples appear to shift toward opal-CT peak location until a decline occurs at the 12- and 14-week sample.

6.1.3 Raman Spectroscopy Results

Red laser Raman spectroscopy (785 nm) was employed to determine how silica gel changed over the course of diagenesis. Due to the high fluorescent nature of silica gel, only four samples were analyzed through Raman: a stock silica gel (opal-A standard), an opal-CT standard, and the 10- and 12-week heated samples. Raman spectroscopy produces broad bands throughout the scanned wavelength. Three notable features appeared, a broad hump centered around 370 cm^{-1} with a noticeable peak located in the center in non-opal-CT samples, a small peak located around 620 cm^{-1}, and a shoulder/peak cluster around 800 cm^{-1} to 900 cm^{-1} in non-opal-CT samples. These features can be seen in figure 18. The 800 cm^{-1} and 900 cm^{-1} double peaks appear to

combined and shift into a singular peak located at 790 cm^{-1} in opal-CT. Additionally, most peaks appear to shift toward opal-CT values at all locations after heating has occurred. Individual peak locations for both samples are presented in Table 3. Individual spectroscopy is presented in appendix D.

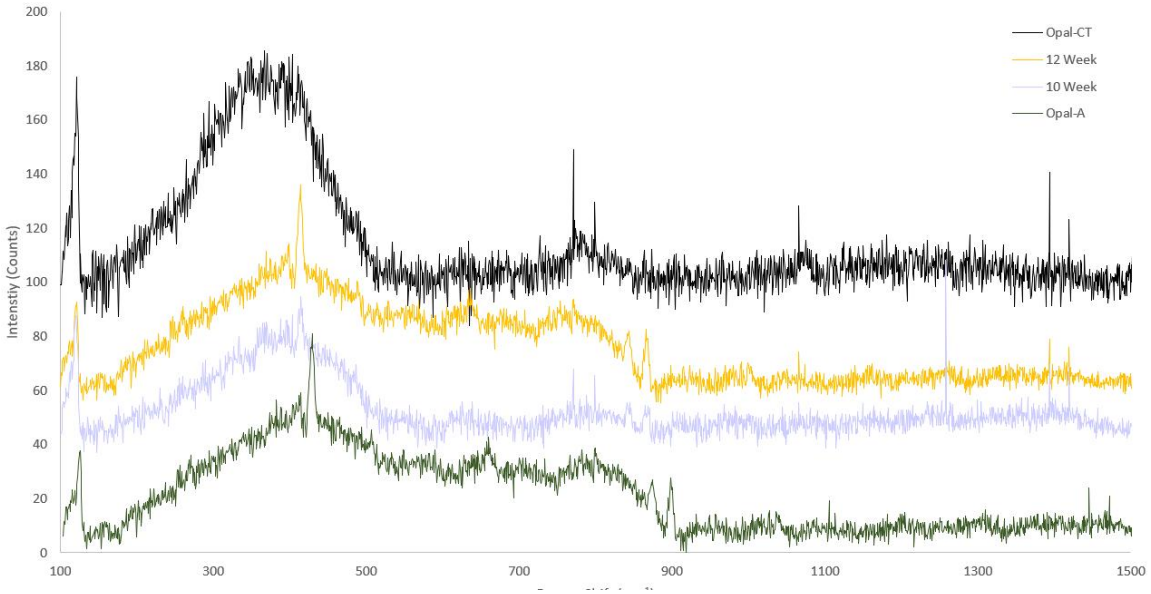

Figure 18**:** Raman signatures of opal standards and 10- and 12-week results. Results are offset in the vertical to show individual characteristics. Opal-CT presents more broad humps where opal-A and heated samples present peaks.

Sample	Bending (cm^{-1})	Symmetrical Stretch (cm^{-1})	Si-O-Si Stretching 1 (cm^{-1})	Si-O-Si Stretching 2 (cm^{-1})
Opal-A	430	665	877	900
10-Week	417	627	845	870
12-Week	416	635	846	870
Opal-CT	375	622	790	N/A

Table 3**:** Vibrational modes of Raman results. In the opal-CT standard, the peak associated with the second Si-O-Si stretching mode was not observed.

6.2 Spatially Resolved Experiments Results

6.2.1 Qualitative Analysis of Samples

Visual inspection of the completed stratified experiments shows shifting of the organic material was minimal, as seen in figure 19(A). Silica and humic acid are relatively isolated from one another and apparently maintained zones created during experimental setup. A light amount of smearing occurred during sample cutting; however, the appearance of spread humic acid in silica sections is superficial. Motion of humic acid away from silica is likely a result from the solidification of the ice during cooling. Location of silica appears to remain unmoved through experimentation and solidification, due to expansion of silica when in solution.

Inspection of the intermixed experiment show the extent to which silica and organics are homogenized. No apparent zoning of exclusive humic acid or silica is present within the sample, suggesting humic acid migration did not occur during experimentation. Figure 19(B) demonstrates the lack of shifting of the top section of the experiments during heating.

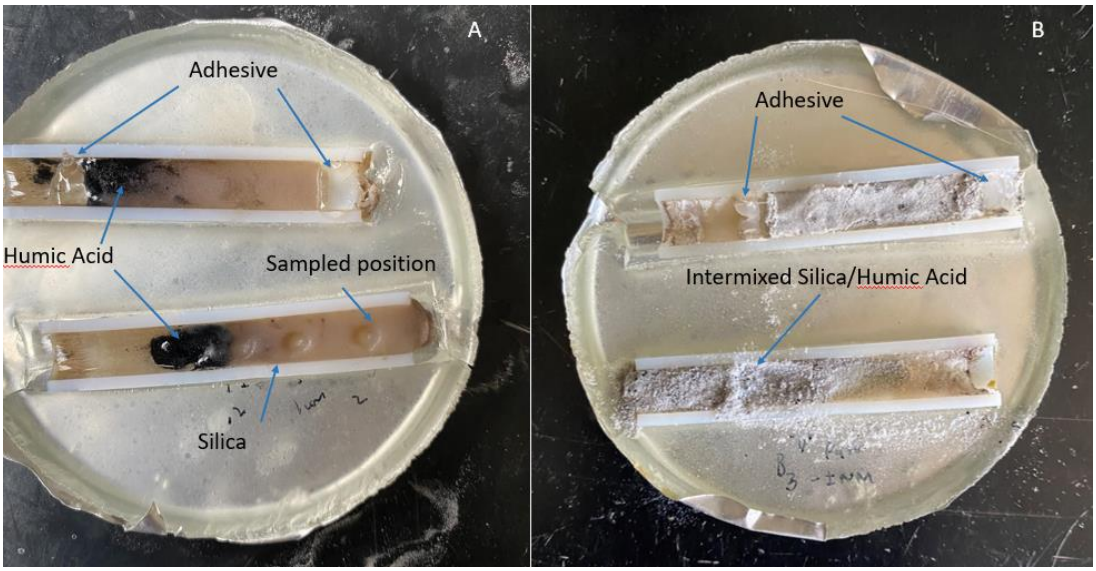

Figure 19. Cut halves of a stratified (A) and intermixed (B) silica experiment. The top section on both samples used adhesive on each end to prevent shifting during drying, while the bottom was used to extract silica immediately after cutting. The solution is still in a semisolid state when the photo was taken in the stratified experiment (A), while the intermixed experiment was dried through heating (B).

.

6.2.2 X-Ray Diffraction Results

XRD patterns from spatially resolved experiments, before and after masking of halite peaks, are located in appendices E and F. Stratified experiments were labeled “B2” and “B4” with coordinating controls being identified as “D2” and “D4”, respectively. Intermixed experiments were labeled “B1” and “B3” with corresponding controls labeled as “D1” and “D3”, respectively. All experiments (stratified, intermixed, and control) show similar diffractograms with large humps at 22° 2θ and large halite peaks at 27° 2θ, 31° 2θ, 45° 2θ, 56° 2θ and 66° 2θ. However, several of the analyzed spots in the stratified experiments and one control experiment show XRD evidence for newly precipitated

opal-CT. Stratified experiments “B2” (at position 0.1 cm and 2.0 cm) as well as “B4” at position 2.0 cm show the appearance of a 36° 2θ peak that may be associated with opal-CT. (see appendix F). Control experiment “D2” also shows this inclusion. Other diffraction features associated with opal-CT, including sharpening and splitting of the broad 22° peak (as seen in Figure 4), were not observed. In both stratified examples (labeled “B2” and “B4”), additional peaks at 54° 2θ and 60° 2θ are present only in both experiments at the most distal position from the organic layer at 2.0 cm.

Stratified experiment “B2” showed minor variations in the FWHM of the 22° 2θ opal-A beak across the tube. At positions 0.1 cm, and 0.2 cm, the FWHM was 5.3° 2θ and 5.00° 2θ, respectively. This 22° 2θ peak narrows further at 1.0 cm with a FWHM of 4.97° 2θ, before slightly broadening to 5.02° 2θ at position 2.0 cm. The equivalent controls “D2” exhibits a FWHM value of 5.08° 2θ and 4.92° 2θ at the 22° 2θ peak (Table GH). Figure 20 displays the relative thickness of the 22° 2θ peak for stratified experiment “B2” and its relative control. No apparent correlation appeared to be present between the 22° 2θ peak FWHM and distal position from organic layer. Due to the high amount of organic content collected at the silica-humic acid interface (0.0 cm), a FWHM could not be determined for this sample. These data are presented in table 4.

Stratified (B2)	FWHM (2θ)
0.1 cm	5.30
0.2 cm	5.00
1.0 cm	4.97
2.0 cm	5.02
Control (D2)	5.08
Control (D2) - 2	4.92

	FWHM (2θ)
Intermixed 1 (B1)	6.00
Intermixed 1 (B1) - 2	5.46
Intermixed 2 (B3)	4.10
Intermixed 2 (B3) - 2	5.60
Control (D1)	4.29
Control (D1) - 2	5.12
Control (D3)	4.22
Control (D3) - 2	5.10

Stratified (B4)	FWHM (2θ)
0.0 cm	4.72
0.1 cm	4.18
0.2 cm	4.50
1.0 cm	5.08
2.0 cm	4.95
Control (D4)	4.04
Control (D4) - 2	4.81

Table 4: Full-Width Half Maximum (FWHM) of 22° 2θ at locations distal from the organic-silica interface in stratified experiment (labeled "B2" and "B4") and intermixed experiments (labeled "B1" and "B3"). Additional corresponding controls were also measured to determine peak form.

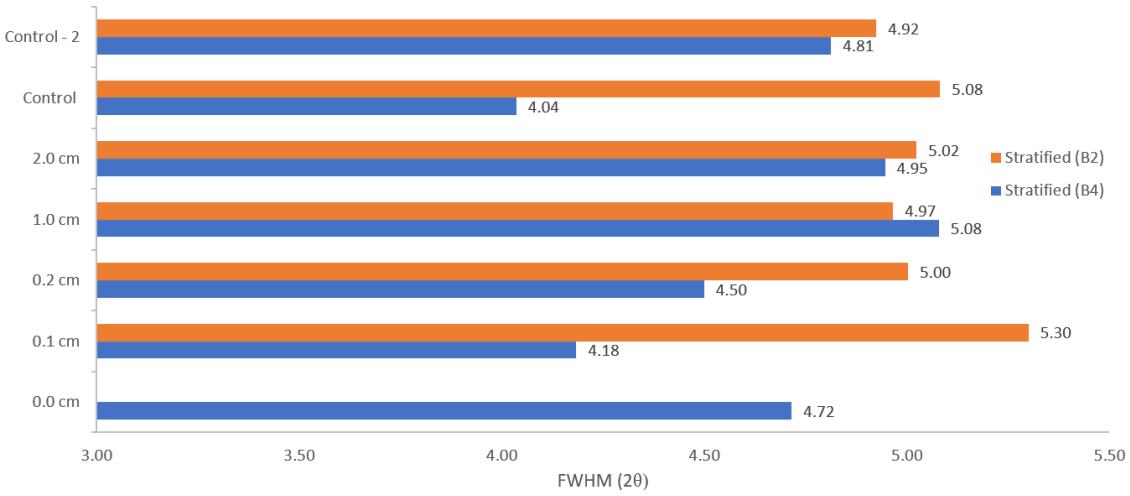

Figure 20: Full-width half maximum (FWHM) of sample collected from stratified experiments (labeled "B2" and "B4"). Distances reported are from the silica-organic layer contact. Corresponding control (labeled "D2" and "D4") values are also reported. "B2" sample has no coordinating 0.0 cm sample due to high humic acid input.

The silica-organic interface in stratified experiment “B4” displayed a FWHM of 4.72° 2θ. This width is narrowed to 4.18° 2θ at 0.1 cm from that interface. The 0.2 cm position shows a broadening to 4.50° 2θ. This peak continues to broaden to 5.08° 2θ at 1.0 cm, then narrows further to 4.95° 2θ at the most distal 2.0 cm. The corresponding controlled experiment “D4” displays a FWHM at the 22° 2θ peak of 4.04° 2θ and 4.81° 2θ. These values are presented in table 4 and can also be observed in figure 20, which shows the relative results of stratified experiment “B4” and its corresponding controls.

Two samples were collected from each of the intermixed experiments and their coordinating controls. Unlike the stratified experiments, neither intermixed experiment showed a 36° 2θ peak associated with opal-CT. Experiment “B1” showed a FWHM of 6.00° 2θ and 5.46° 2θ for both samples collected. The coordinating controls “D1” had a FWHM of 4.29° 2θ and 5.12° 2θ. Intermixed experiment “B3” showed a FWHM of 4.10° 2θ and 5.60° 2θ with its coordinating control “D1” showing a FWHM° of 4.22° 2θ and 5.10° 2θ. These values are presented in table 4 and can also be seen in figure 21. Figure 22 displays the variability of the control experiments’ FWHM with values ranging from 4.04° 2θ to 5.08° 2θ. Additionally, variability of all controls throughout the experiments can be seen in figure 21. Some differences were observed between controls and intermixed experiments; intermixed experiments demonstrate less ordering, potentially suggesting that the presence of organics inhibits opal-A internal ordering.

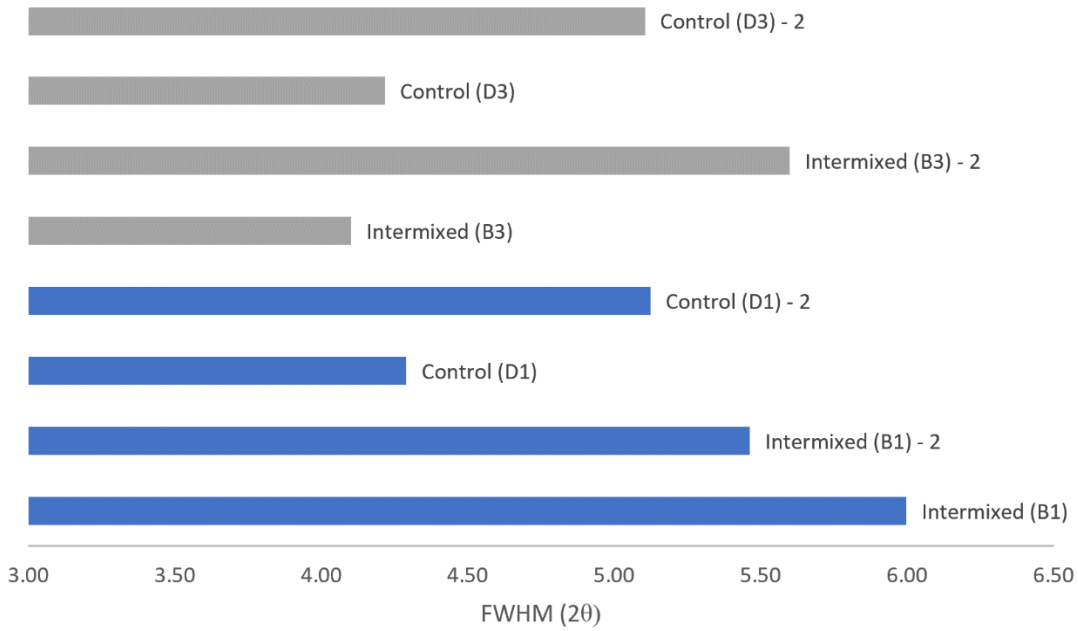

Figure 21: Full-width half maximum (FWHM) of 22° 2θ peak in both intermixed experiments and coordinating controls. Graph shows variability in closed systems with near identical environments.

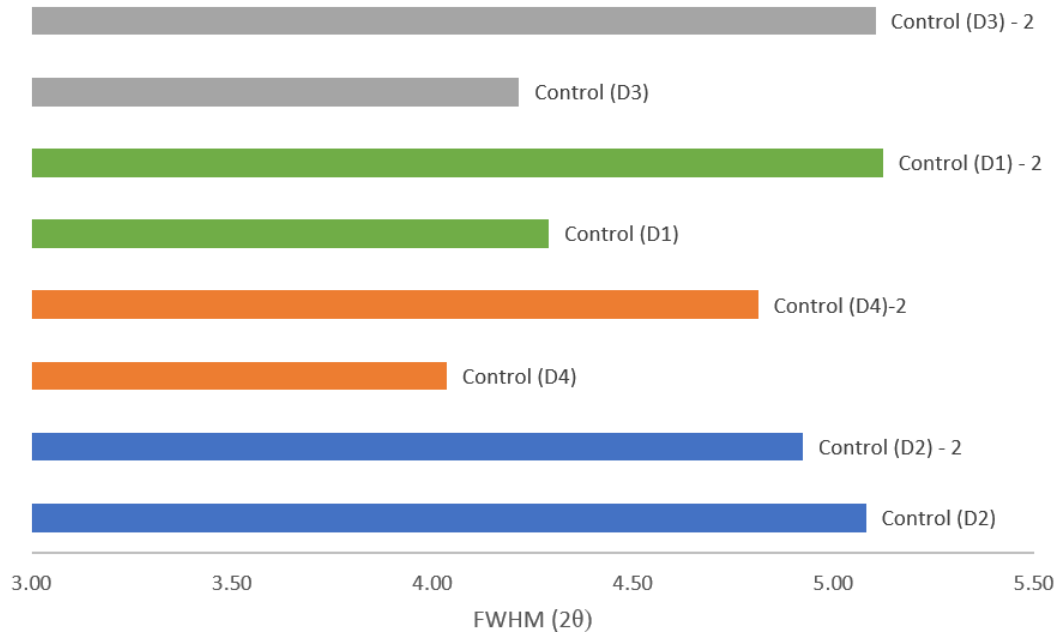

Figure 22: Full-width half maximum (FWHM) of 22° 2θ controls across all experiments. Value variability illustrates range of possible values for collected samples in near identical environments.

6.2.3 Fourier-Transform Infrared

Each experiment has its 450 cm^{-1}, 800 cm^{-1}, and 1060 cm^{-1} peak locations (associated with the Si-O bending, Si-O symmetrical stretching, and Si-O-Si stretching mode, respectively) mapped as described in the methods section. An example plot from the opal-A standard is presented in figure 23.

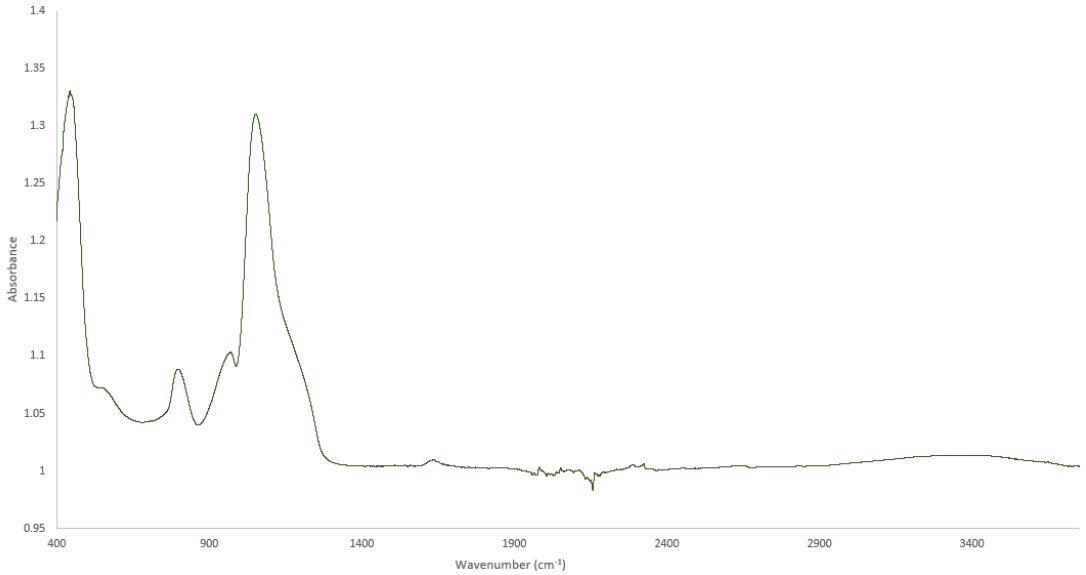

Figure 23: Example spectra of silica in Fourier-transform infrared (opal-A standard). Notable peaks are located at 450 cm^{-1}, 800 cm^{-1} and 1060 cm^{-1} corresponding to the Si-O bending, Si-O symmetrical stretching, and Si-O-Si stretching mode of Si-O, respectively.

In stratified experiment "B2" and associated controls, each sample location exhibit a Si-O bending mode at 445 cm^{-1} with a notable exception at the organic-silica interface (0.0 cm), where the peak was located at 418 cm^{-1}. Symmetrical stretching modes are generally the same for each experimental location and controls with values ranging from 797-800 cm^{-1}. The Si-O-Si stretching mode exhibits more variability, with

the organic-silica interface exhibiting a mode at 1030 cm^{-1}. This Si-O-Si stretching mode appears to shift to higher wavenumbers the more distal from the silica-organic interface, with values of 1050 cm^{-1} at 0.1 cm, to 1054 cm^{-1} at 2.0 cm. More distal values seem to correspond to organic free controls, with Si-O-Si stretching modes at 1058 cm^{-1}. These values are presented in table 5 and comparison graphs are in appendix G.

In stratified experiment "B4" and "D4" controls, Si-O bending modes were observed at 445-448 cm^{-1} for all locations, with the notable exception of the organic-silica interface, where the peak is modestly shifted to 418.0 cm^{-1}. Symmetrical stretching mode positions are consistent across all samples and coordinating controls, with peak positions ranging from 797 cm^{-1} to 800 cm^{-1}. All samples and coordinating controls show a Si-O-Si stretching mode from 1054-1058 cm^{-1}, with the silica-organic interface showing a peak at 1030 cm^{-1}. These values are presented in table 5.

Intermixed experiment "B1" and "B3" with coordinating controls show Si-O bending modes at 441-445 cm^{-1} with the notable exception of the B3 sample at 433 cm^{-1}. Like previous samples, the symmetrical stretching mode shows little variability, with all positions at 800 cm^{-1} in both intermixed experiments and corresponding controls. The stretching mode seems to be at slightly smaller peak positions in intermixed experiments, ranging from 1051-1054 cm^{-1}, where the corresponding controls have peak positions ranging from 1054-1058 cm^{-1}. These values are presented in table 5.

Stratified "B2"	Bending (cm^{-1})	Stretching (cm^{-1})	Si-O-Si Stretch (cm^{-1})
0.0 cm	418	797	1030
0.1 cm	445	798	1050
0.2 cm	445	798	1047
1.0 cm	445	799	1054
2.0 cm	445	799	1054
Control (D2)	445	800	1058
Control (D2) -2	448	799	1058
Stratified "B4"	Bending (cm^{-1})	Stretching (cm^{-1})	Si-O-Si Stretch (cm^{-1})
0.0 cm	418	797	1030
0.1 cm	445	799	1054
0.2 cm	448	800	1058
1.0 cm	448	800	1058
2.0 cm	445	800	1058
Control (D4)	445	799	1058
Control (D4) - 2	448	799	1058
Intermixed	Bending (cm^{-1})	Stretching (cm^{-1})	Si-O-Si Stretch (cm^{-1})
B1	445	800	1054
B1 - 2	445	799	1054
B3	433	799	1051
B3 - 2	445	799	1054
Control (D1)	445	799	1058
Control (D1) - 2	441	799	1054
Control (D3)	445	799	1058
Control (D3) - 2	445	800	1058

Table 5: Fourier-transform infrared peak positions for various Si-O and Si-O-Si modes. Si-O bending and symmetrical stretching modes are located around 450 cm^{-1} and 800 cm^{-1} while the Si-O-Si stretching mode is located around 1060 cm^{-1}

6.3 Humic Acid Results

Analysis of humic acid substance in stratified experiments was conducted to determine how humic acid changes over the course of 12 weeks of high temperature and pressure. Samples were collected from the humic acid layers of both stratified experiments and compared to the unreacted humic acid standard. Figure 24 shows the x-ray diffractogram for the humic acid standard and sampled humic acid in stratified experiments “B2” and “B4. Major and minor peak location for both the standard and stratified experiment are presented in table 6. The humic acid standard shows large peaks at 12.4° 2θ, 20.7° 2θ, 24.9° 2θ, and 26.6° 2θ, with various minor peaks. After heating for twelve weeks at 200^{o} C, the major peak at a 20.7° 2θ and minors peak at 11.6° 2θ, 39.6° 2θ, 42.6° 2θ and 50.3° 2θ were removed. An additional peak of 27.6° 2θ is present after heating, but it is associated with halite formation. Individual graphs of each humic acid substance with peak removed are in appendix H.

In FT-IR spectra, humic acid peak locations appear to be consistent before and after heating, with a double peak location at 418 cm^{-1} and 464 cm^{-1}. A shoulder is also present at 534 cm^{-1}. Additional notable peaks are present at 792 cm^{-1} and 912 cm^{-1} with a large double peak located at 1006 cm^{-1} and 1028 cm^{-1}. The most notable difference between the heated and unheated humic acid material is the reduction of the large OH vibration mode mound at 2800-3400 cm^{-1}. These spectra are presented in figure 25.

	Standard (2θ)	Stratified Experiment (2θ)
Major Peaks	12.4	12.4
	20.7	Removed
	24.9	24.9
	26.6	26.6
Minor Peaks	11.6	Removed
	19.9	19.9
	20.4	20.4
	21.3	21.3
	29.1	29.1
	30.1	30.1
	35.4	35.4
	36.1	36.1
	36.7	36.7
	37.9	37.9
	38.6	38.6
	39.6	Removed
	42.6	Removed
	50.3	Removed
	55.3	55.3
	60.2	60.2
	62.5	62.5
	65.3	65.3
	68.4	68.4

Table 6: Major and minor peaks present in the humic acid standard and sampled humic acid from stratified experiments after experimentation.

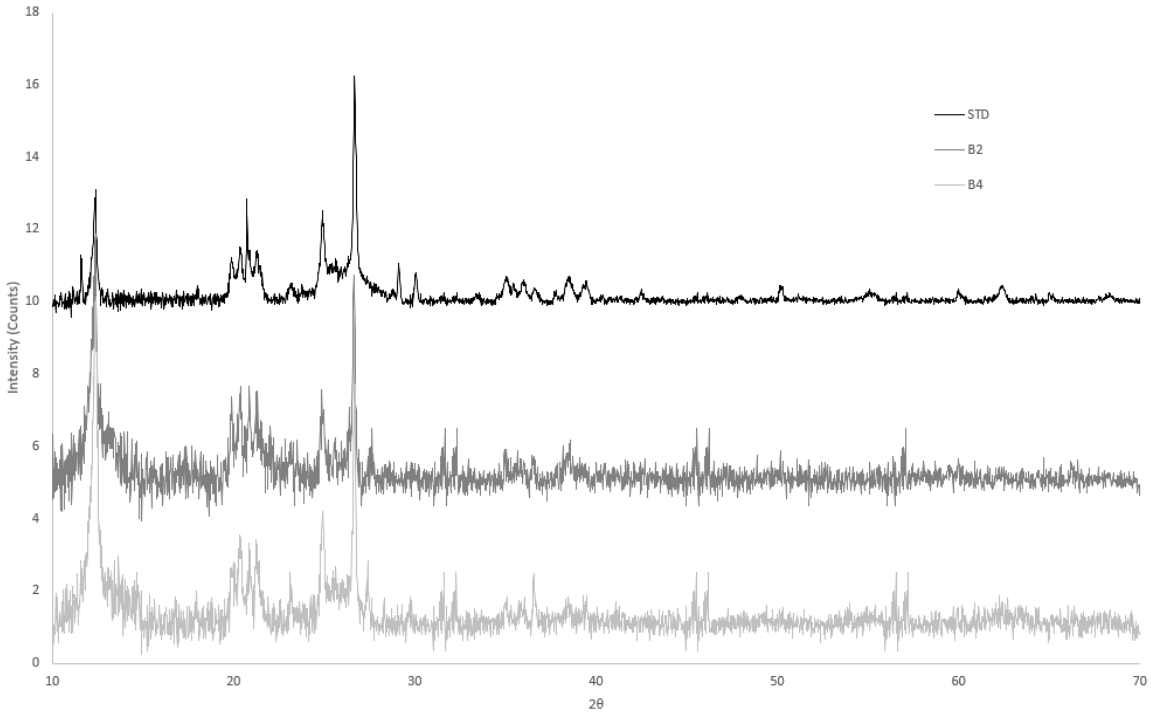

Figure 24: X-Ray diffractogram of humic acid standard and humic acid from stratified experiments (labeled "B2" and "B4") with halite peaks removed. Many major and minor peaks are removed after prolong heating, resulting in a more simplified structure.

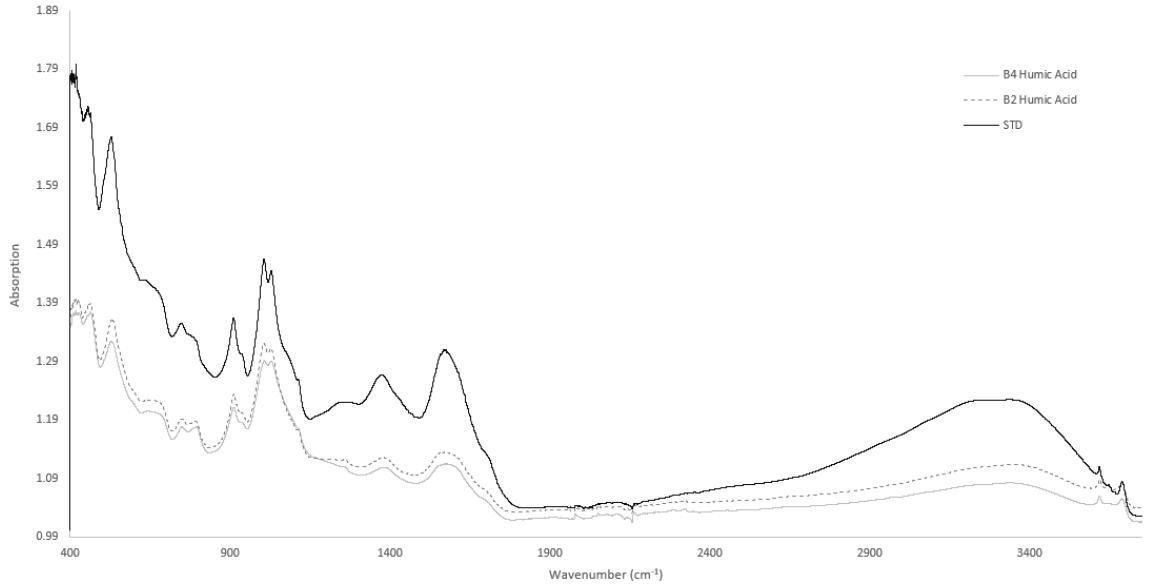

Figure 25: Humic acid standard and stratified experiment humic acid Fourier-transform Infrared spectra.

CHAPTER 7

DISCUSSION

7.1 Bulk Diagenetic Experiments

7.1.1 X-Ray Diffraction

Changed in the FWHM of the broad peak in silica XRD patterns suggest that internal ordering is occurring inside the silica gel as incremental heating occurs. The R^2 value of the trendline suggests a strong correlation between FWHM and heating time. Although it appears that FWHM decreased with each subsequent two weeks of heating, an increase in the FWHM does occur after the sixth week before it continues to reduce again. Additionally, large reductions in the FWHM occur after the 10-week sample. Despite the apparent internal ordering of opal-A, no peak consistent with opal-CT was the observed at 36° 2θ, so it is unlikely that any opal-CT has precipitated in these samples. These results, suggesting incremental shifts in opal-A structure with heating time, are not completely unexpected. Others have noted the narrowing of the 22° 2θ as paracrystalline ordering occurs within the silica gel (Keller and Isaacs, 1985; Elzea et al., 1994; Curtis et al., 2019; Liesegang and Tomaschek, 2020). Our study, however, attempted to look at incremental timesteps of this sequence to track changes in the structure. What was unexpected in our results is the apparent lack of any opal-CT precipitation over the studied timeframe. It is possible the inclusion of a 16-week or

longer experiment would provide better insight on this alteration of the silica gel; however, time did not permit an additional experiment of this length.

7.1.2 Fourier-Transform Infrared

Tracking the peak position of various bands in FT-IR yielded interesting results. The Si-O bending mode located around 450 cm^{-1} provides insight on the modes transition from opal-A to opal-CT internally. Although it has been previously noted the Si-O bending mode progresses towards a peak position of 470 cm^{-1} (Rice et al, 1995; Curtis et al., 2019), our results suggest this transition is not as smooth as previously noted. Generally, the location of the band does appear to shift initially but fails to shift any significant amount during heating. Furthermore, the shift present at the 10-week sample deviates radically before returning to its original 449 cm^{-1} in the 12-week sample.

Unlike the Si-O bending mode, the Si-O symmetrical stretching mode at 800 cm^{-1} appears to remain stagnant for much of the heating process. However, the 12-week sample does shift toward peak positions that mirror opal-CT's Si-O symmetrical stretching mode. It is possible that this motion is within a standard range of fluctuation associated with the symmetrical stretching mode of Si-O, suggesting the motion of the molecule is not reactive to heating for parts of the diagenetic process. The Si-O symmetrical stretching mode appears to be the least reactive of the motions in FT-IR in this study.

The Si-O-Si stretching mode, located around 1060 cm^{-1}, appears to show the most promise in tracking the change of opal-A to opal-CT. Peak locations appear to shift rapidly over the course of the first four weeks of heating as the peak shifts from 1051 cm^{-1} to 1062 cm^{-1}. These values plateau for most of the sequential heating until they shift back to lower wavenumbers for the 12-week sample. Although peak locations plateau, it does indicate that using the Si-O-Si stretching band in FT-IR might be a useful method to characterize early changes in silica.

7.1.3 Raman Spectroscopy

Raman spectroscopy has proven to be a difficult technique to use for characterizing opal structure. The most immediate issue during this technique was the transparent nature of the silica. This transparency caused the Raman laser to penetrate the silica and read nearby molecules. This proved particularly troublesome when using any plastics to contain the sample, as carbon signals from the plastics overshadow the opal signatures. Additionally, the transparency prevented the 1-micron spot size from analyzing an individual silica grain, resulting in the inclusion of measurements of nearby grains. This inclusion of other grain measurements is challenging when attempting to map changes in silica or analyze different silica grain. Finally, oversaturation due to fluorescence was an issue when scanning silica grains (Curtis et al., 2019). Attempts to use a higher wavelength laser (785 nm) at a lower power setting to reduce the effects of this saturation proved beneficial but with mixed success. Although some samples worked

(10 and 12-week sample), only the standards of opal-A and opal-CT produced readable signals. It is possible that water in the solution was incorporated more readily into the structure at earlier timesteps since opal absorbs water naturally. This incorporation was potentially later counterbalanced by the heating at longer timesteps, causing removal of structural water.

Three notable peaks were present in the Raman results: a broad band located around 300-450 cm^{-1}, a weak peak around 620 cm^{-1}, and a peak around 800-900 cm^{-1}. As suggested by Curtis et al. (2019), it is difficult to assign a mode to the Si-O-Si signatures in these ranges. However, we can see some shifts occurring in peak locations most notable after the phase transition to opal-CT. The first broad band has a central peak in the broad hump for each opal-A variant that seems to shift slightly to lower Raman values. This migration of peaks seems to follow the trend toward an opal-CT peak at 375 cm^{-1}, however, the peak located in the center of the broad hump is removed. The minor peak located at 665 cm^{-1} rapidly shifts to the values similar to opal-CT, suggesting those Si-O modes mirror opal-CT more closely than opal-A. Finally, in non-opal-CT samples, two peaks appear around 800-900 cm^{-1}. These peaks disappear after the formation of opal-CT and seem to morph into a singular peak at 790 cm^{-1}.

7.2 Spatially Resolved Experiments

7.2.1 X-Ray Diffraction

Based on the appearance of the 36° peak, it is possible that opal-CT formation has occurred at some locations within the stratified experiments “B2” and “D2”, and within the control experiment “D2”. However, this formation of opal-CT appears to be sporadic, as seen by its formation in stratified experiments and one of the four controls. The appearance of opal-CT has no systematic relationship with distance from the organic layer. This result suggests we cannot prove or disprove hypothesis one (more opal-CT formation with increasing distance from organic matter). The doublet near 4.0 Å is necessary to determine the ordering and complexity of opal-CT (see Figures 3 and 4), but those peaks were not observed. Therefore, we are unable to prove or disprove hypothesis three (newly formed opal-CT will be more ordered in intermixed experiments than stratified). If future analyses with larger datasets definitively conclude that opal-CT does not form in intermixed experiments but does in stratified experiments, , it would suggest that opal-CT formation is inhibited by close proximity to organic matter, supporting hypothesis one. Conversely, if formation of opal-CT appears sporadic in intermixed experiments as well as the controls, then there would be no clear relationship between opal diagenesis and organic matter proximity and hypothesis one would be invalidated.

X-ray diffraction of stratified experiments seems to suggest that the proximity to the silica-organic interface does not affect the FWHM of the 22° 2θ peak. This

interpretation suggests hypotheses two (ordering of opal-A in relation to proximity) was not proven, as we do not see any significant link between proximity to organic material and opal internal structuring. Most samples fall within the range of FWHM defined by their corresponding controls, suggesting that we did not see an effect of organic matter on opal ordering. However, with stratified experiment “B2”, the 0.1 cm sample falls outside this envelope with a much larger FWHM, which could suggest less ordering is occurring inside the silica. This trend is not present in the “B4” experiment, possibly due to the higher concentration of more ordered silica gels sampled in the same collection. This issue highlights the downside of bulk powder XRD as the primary mode of analysis in characterizing microtextural samples. XRD is unable to perform precise measurements at small spot sizes, offering only a broad glimpse of the material analyzed.

Results from intermixed experiments provided mixed interpretations of the ordering occurring within the silica gel. In these more intimately mixed samples, it was hypothesized (see hypothesis two) that less ordering overall would occur due to the more immediate interactions with humic acid. While intermixed experiment “B1” seems to corroborate this prediction, with larger FWHM from 5.46-6.0° 2θ as compared to its controls (“D1”), the “B3” experiment exhibited a much larger range of values from 4.10-5.60° 2θ. Using the mean of the intermixed samples, with a FWHM of 5.29° 2θ, and comparing it to the controls, with an average of 4.68° 2θ, we can see more ordering is occurring in the control samples which are unabated by organic material. Although this difference is notable, more samples are needed to determine if this is consistent for these samples. Finally, although the controls displayed internal variability within each sample,

almost all control experiments exhibited the same distribution of FWHM values. This variability may suggest internal structure of opal-A changes at variable rates, independent heating over a fixed duration. Furthermore, samples analyzed after prolonged periods of little disruption (example: control (D3) - 2) all had less-ordered FWHM of the 22° 2θ peak. This may suggest that leaving samples undisturbed for month-long time frames may affect the internal structure over time.

7.2.2 Fourier-Transform Infrared

As previously discussed for bulk experiments, FT-IR Si-O modes are found at three locations: the Si-O bending mode at 450 cm^{-1}, the Si-O symmetrical stretching mode at 800 cm^{-1}, and the Si-O-Si stretching mode at 1060 cm^{-1}. For stratified experiments, both the Si-O bending and symmetrical stretching mode seems to be relatively stable for all locations, including in corresponding controls. In both experiments, however, the silica-organic interface shows peak locations at lower wavenumbers for the bending mode. It is possible that this change in peaks is due to the influence of humic acid sampled in this zone; however, these values are not present in pure humic acid samples. The Si-O-Si stretching mode in both samples show some trends toward higher peak locations in both stratified experiments, suggesting that migration of the Si-O-Si stretching mode shifts with proximity to organic material. This is witnessed as peaks closer to the silica-organic interface mirror values closer to stock silica gel and more distal samples shift toward control experiments.

FT-IR analysis of intermixed experiments showed mixed results, in the efficacy of various Si-O modes as markers for phase transition. Both intermixed and control experiments did not exhibit much variability in peak locations for both the Si-O bending and symmetrical stretching modes. However, the Si-O-Si stretching mode at 1060 cm^{-1} did appear to be consistently lower in intermixed experiments as compared to control experiments. This shift in the Si-O-Si stretching mode suggests structural change in the opal may be inhibited by the interaction of organic material in the sample, further corroborating the stratified experiment results. However, without markers of phase transition (i.e. peak associated with opal-CT), it is not possible to determine to what extent the organic material inhibits this transition.

7.3 Humic Acid Analysis

The use of XRD is challenging when trying to characterize organic molecules due to the complex nature of the molecule in conjuncture with its non-fixed structure (Pollack et al., 1971; Gerasimowicz et al., 1986; Fründ et al., 1989; Sirotiak and Bartošová, 2016). Our analysis of humic acid does provide some insight into the changing molecular structure after prolonged heating. The removal of some peaks seems to indicate breakdown of the molecule. However, only a minor number of peaks are removed, suggesting that these conditions may have broken down humic acids' aromatic structure, leaving simpler C-H structures, as noted by previous authors (e.g., Pollack et al., 1971; Chang et al., 2006; Sirotiak and Bartošová, 2016). No clear characterization of these

peaks, however, are present in literature, and mixed results seem prevalent, suggesting this method of analysis is not ideal for classification.

Generally, peak locations in FT-IR are unmoved during heating of the humic acid. Most peak inclusions are located between 400-1000 cm^{-1}, corresponding to the aromatic rings of humic acid (Sirotiak and Bartošová, 2016). The lack of any shifting in this section suggests the breakdown of the aromatic ring has not occurred, at least not in a significant quantity. These results are potentially at odds with the XRD data, suggesting the XRD was able to detect minor structural changes in the aromatic ring, while FT-IR can only detect the complete breakdown of this ring. Another possible explanation for this variability might be the results of XRD's ability to detect changes in smaller grain sizes, changes that occurred due to degradation of the humic acid over experimentation, while FT-IR cannot. Gerasimowicz et al. (1986) suggested the z-dimensional bending mode of C-H may be located near 950 cm^{-1}, which does not appear to be present in either sample, suggesting this mode may only occur after further structural changes.

7.4 Monterey Formation and Implications

If this study is correct, and micro proximity to organic material does not play a significant role in the process of silica diagenesis, then any configuration of silica and organic matter will result in inhibition of silica during diagenesis. This result might also suggest grain size and distribution of organic matter in siliceous sedimentary rocks might play a minimal role in controlling silica phase transitions. Zones in the Monterey

Formation where organic material is rich might show inhibition of phase transitions, regardless of the proximity to organic material. Additionally, if microtextural interactions are not a key mechanism in the phase transitions of silica during diagenesis, then packets of strata in the Monterey Formation could be characterized by their formation temperatures based solely on the combination of phases of silica present, the detrital content and the organic input. This excludes the arrangement of those inputs in any strata, suggesting bulk lithology and organic input are the dominant mechanisms for phase transition.

Additionally, if microtextural heterogeneity does not influence phase transition, then observed deviations in silica minerology could be used as a proxy for nearby organic matter. Alternatively, these results could suggest the use of geophysical markers of silica as a proxy with temperatures and organic matter content for oil reservoir locations. These suggestions could have sweeping impacts on the use of hydrocarbon analysis of the Monterey Formation. The lack of link in this study might suggest knowing the phases of silica present in the strata of the Monterey Formation can be used to determine the maturation of a nearby hydrocarbon reservoir, by using the simplistic analysis of Keller and Isaacs (1985) and Hinman (1990).

It is possible we can apply our characterization of humic acid as early work for structural changes to humic acid during heating and apply it to humic acid present inside the Monterey Formation. Although this natural analogue is present in the formation, kerogen and marine algae are the main input of organic compounds in the Monterey and

are more structurally complex, resulting in the need of additional study using those organic compounds (Isaacs, 1985; Isaacs and Petersen, 1987; Behl, 1999).

Because the identification of opal-CT in our experiments was not definitive, and because the putative opal-CT detections were sporadic and did not follow the distribution we hypothesized, additional insight on the controls on the opal-A to opal-CT transition are needed. If the intermixed experiments show lack of opal-CT in all locations of the experiments, those results suggest intimate mixture of silica and organics play a role in the inhibition of silica diagenesis, due to the close interactions of silica and organics. If those intermixed experiments do show sporadic formation of opal-CT, as well as in controlled experiments, then it can be concluded that microtextural interactions of opal-CT does not appear to play a role in silica diagenesis. To determine a better understanding of this mechanism, this study should be repeated on a larger set of samples within each experiment.

7.5 Future Work

The work presented here should act as a guide for future studies. In addition to some observations about shifts in the diffraction and spectroscopic peaks of silica during early stages of diagenesis, this work acts as a proof-of-concept of experimental design. Determining the time at which diagenesis occurs for opal-A to completely change into opal-CT will allow for better interpretations of these microtextural interactions in stratified experiments. Additionally, determining this window will allow for further

analysis of how bulk opal-A changes before diagenesis. Numerous additional samples are also needed at previously collected timesteps to determine data consistency. Humic acid changes at various timesteps could provide more insight into the structural changes of humic acid during heating as well as analysis using other organic compounds found in the Monterey Formation. Finally, locating natural analogues to our studies (where organic matter and silica occur in distinct configurations and/or grain sizes) in the Monterey Formation could provide strong natural analogues to supplement the work of this study.

CHAPTER 8

CONCLUSION

Structural analysis of amorphous material like opaline silica is frequently challenging due to the lack of repeating fixed structure. Previous work has identified silica phase transitions and tracked environmental conditions that influence the temperature at which those changes occur. The experiments in this thesis were designed to explore the potential influence of microtextural interaction between silica and organics on silica phase transitions, an understudied topic in the literature. In bulk experiments we observed shifts in XRD 22° 2θ peak FWHM and in FT-IR Si-O-Si peak location with heating, suggesting internal ordering within opal-A. Future studies are required to fully determine the efficacy of the above measurements for tracking opal diagenesis before the first phase transition.

Opal-CT formation may have precipitated sporadically in some of our spatially resolved experiments; however, with the lack of additional peaks around 22° 2θ these results are inconclusive. Therefore, we were unable to prove or disprove our hypothesis 1 (more opal-CT formation the more distal from organics) and our hypothesis 3 (opal-CT formation will be more ordered in closely mixed experiments). Our second hypothesis appears to be unmet as no correlation was observed between proximity to organic material and the ordering of the opal-A 22° 2θ peak; however, future studies should determine the consistency of this claim. Structural degradation of humic acid with heating was observed by XRD but not FT-IR, suggesting that XRD might be able to

determine minor structural changes to humic acid, while FT-IR only detects large structural changes.

REFERENCES CITED

Behl, Richard J. "Since Bramlette (1946): The Miocene Monterey Formation of California revisited." *Classic Cordilleran Concepts: A View from California: Geological Society of America, Special Paper* 338 (1999): 301-313.

Behl, Richard J. "Chert spheroids of the Monterey Formation, California (USA): early-diagenetic structures of bedded siliceous deposits." *Sedimentology* 58, no. 2 (2011): 325-351.

Bennett, Richard H., Barbara Ransom, Miriam Kastner, Roy J. Baerwald, Matthew H. Hulbert, William B. Sawyer, Harold Olsen, and Michael W. Lambert. "Early diagenesis: impact of organic matter on mass physical properties and processes, California continental margin." *Marine Geology* 159, no. 1-4 (1999): 7-34.

Bodnar, Robert J. "Petroleum migration in the Miocene Monterey Formation, California, USA: constraints from fluid-inclusion studies." *Mineralogical Magazine* 54, no. 375 (1990): 295-304.

Bohrmann, Gerhard, Andrea Abelmann, Rainer Gersonde, Hans Hubberten, and Gerhard Kuhn. "Pure siliceous ooze, a diagenetic environment for early chert formation." *Geology* 22, no. 3 (1994): 207-210.

Bramlette, Milton Nunn. *The Monterey Formation of California and the origin of its siliceous rocks*. Vol. 212. US Government Printing Office, 1946.

Compton, John S. "Porosity reduction and burial history of siliceous rocks from the Monterey and Sisquoc Formations, Point Pedernales area, California." *Geological Society of America Bulletin* 103, no. 5 (1991): 625-636.

Chang Chien, S. W., M. C. Wang, J. H. Hsu, and K. Seshaiah. "Influence of fertilizers applied to a paddy− upland rotation on characteristics of soil organic carbon and humic acids." *Journal of agricultural and food chemistry* 54, no. 18 (2006): 6790-6799.

Crawford, F. D. "Petroleum Potential of Santa Maria Province, California: Region 2." (1971): 316-328.

Curtis, Neville J., Jason R. Gascooke, Martin R. Johnston, and Allan Pring. "A review of the classification of opal with reference to recent new localities." *Minerals* 9, no. 5 (2019): 299.

Day, Rachel, and Brian Jones. "Variations in water content in opal-A and opal-CT from geyser discharge aprons." *Journal of Sedimentary Research* 78, no. 4 (2008): 301-315.

DePaolo, Donald J., and Kenneth L. Finger. "High-resolution strontium-isotope stratigraphy and biostratigraphy of the Miocene Monterey Formation, central California." *Geological Society of America Bulletin* 103, no. 1 (1991): 112-124.

Drees, Richard L., Larry P. Wilding, Neil E. Smeck, and Abu L. Senkayi. "Silica in soils: quartz and disordered silica polymorphs." *Minerals in soil environments* 1 (1989): 913-974.

Dunham, J. B., B. W. Bromley, and V. J. Rosato. "Geologic controls on hydrocarbon occurrence within the Santa Maria basin of western California." *Economic geology, US: Boulder, Colorado, Geological Society of America, Geology of North America* (1991): 431-446.

Dunkel, Catherine A., and Kenneth A. Piper, eds. *1995 National Assessment of United States Oil and Gas Resources: Assessment of the Pacific Outer Continental Shelf Region*. US Department of the Interior, Minerals Management Service, Pacific OCS Region, Office of Resource Evaluation, 1997.

Elzea, J. M., I. E. Odom, and W. J. Miles. "Distinguishing well ordered opal-CT and opal-C from high temperature cristobalite by X-ray diffraction." *Analytica Chimica Acta* 286, no. 1 (1994): 107-116.

Flörke, O. W., Floerke OW, and Segnit ER. "The genesis of hyalite." (1973).

Flörke, O. W., H. Graetsch, K. Röller, B. Martin, and R. Wirth. "Nomenclature of micro- and non-crystalline silica minerals." *Neues Jahrbuch für Mineralogie, Abhandlungen* 163 (1991): 19-42.

Fründ, R., H-D. Lüdemann, Francisco Javier Gonzalez-Vila, G. Almendros, J. C. Del Rio, and F. Martin. "Structural differences between humic fractions from different soil types as determined by FT-IR and 13 C-NMR studies." *Science of the total environment* 81 (1989): 187-194.

Gerasimowicz, Walter V., D. Michael Byler, and Heino Susi. "Resolution-enhanced FT-IR spectra of soil constituents: humic acid." *Applied spectroscopy* 40, no. 4 (1986): 504-507.

Ghisoli, C., F. Caucia, and L. Marinoni. "XRPD patterns of opals: A brief review and new results from recent studies." *Powder Diffraction* 25, no. 3 (2010): 274-282.

Glass, B. P. "Tektites." *Journal of non-crystalline solids* 67, no. 1-3 (1984): 333-344.

Graetsch, Heribert. "Structural characteristics of opaline and microcrystalline silica minerals. In Silica." *Reviews in mineralogy* 29 (1994): 209-232.

Graham, S. A., and L. A. Williams. "Tectonic, depositional, and diagenetic history of Monterey Formation (Miocene), central San Joaquin basin, California." *AAPG bulletin* 69, no. 3 (1985): 385-411.

Heaney, Peter J. "Structure and chemistry of the low-pressure silica polymorphs." Review in Mineralogy: Silica" vol. 29 (1994) 1-40.

Herdianita, N. R., P. R. L. Browne, K. A. Rodgers, and K. A. Campbell. "Mineralogical and textural changes accompanying ageing of silica sinter." *Mineralium deposita* 35, no. 1 (2000): 48-62.

Hinman, Nancy W. "Chemical factors influencing the rates and sequences of silica phase transitions: effects of organic constituents." *Geochimica et Cosmochimica Acta* 54, no. 6 (1990): 1563-1574.

Hinman, Nancy W. "Sequences of silica phase transitions: effects of Na, Mg, K, Al, and Fe ions." *Marine Geology* 147, no. 1-4 (1998): 13-24.

Ingle, James C. "Summary comments on Neogene biostratigraphy, physical straigraphy, and paleo-oceanography in the marginal northeastern Pacific Ocean." (1973).

Ingle Jr, James C. "Origin of Neogene diatomites around the North Pacific rim." (1981): 159-179.

Ingle, J. C. "Cenozoic paleobathymetry and depositional history of selected sequences within the southern California continental borderland." *Cushman Laboratory for Foraminiferal Research, Special Publication* 19 (1980): 163-195.

Isaacs, Caroline M. "Lithostratigraphy of the Monterey Formation, Goleta to Point Conception, Santa Barbara coast, California." (1981): 9-23.

Isaacs, Caroline M. "Porosity reduction during diagenesis of the Monterey Formation, Santa Barbara coastal area, California." (1981): 257-271.

Isaacs, Caroline M. "Influence of rock composition on kinetics of silica phase changes in the Monterey Formation, Santa Barbara area, California." *Geology* 10, no. 6 (1982): 304-308.

Isaacs, Caroline M. "Abundance versus rates of accumulation in fine-grained strata of the Miocene Santa Barbara Basin, California." *Geo-Marine Letters* 5, no. 1 (1985): 25-30.

Isaacs, C. M., and N. F. Petersen. "Petroleum the miocene Monterey formation, California." In *Siliceous sedimentary rock-hosted ores and petroleum*, pp. 83-116. 1987.

Jones, J. B., J. V. Sanders, and E. R. Segnit. "Structure of opal." *Nature* 204, no. 4962 (1964): 990-991.

Jones, JB T., and E. R. Segnit. "The nature of opal I. Nomenclature and constituent phases." *Journal of the Geological Society of Australia* 18, no. 1 (1971): 57-68.

Kastner, Miriam, J. B. Keene, and J. M. Gieskes. "Diagenesis of siliceous oozes—I. Chemical controls on the rate of opal-A to opal-CT transformation—an experimental study." *Geochimica et Cosmochimica Acta* 41, no. 8 (1977): 1041-1059.

Kastner, Miriam, and J. M. Gieskes. "Opal-A to opal-CT transformation: a kinetic study." In *Developments in Sedimentology*, vol. 36, pp. 211-227. Elsevier, 1983.

Keller, Margaret A., and Caroline M. Isaacs. "An evaluation of temperature scales for silica diagenesis in diatomaceous sequences including a new approach based on the Miocene Monterey Formation, California." *Geo-Marine Letters* 5, no. 1 (1985): 31-35.

Knauth, L. Paul, and Samuel Epstein. "The nature of water in hydrous silica." *American Mineralogist* 67, no. 5-6 (1982): 510-520.

Knauth, L. Paul. "Petrogenesis of chert." *Rev. Mineral.* 29 (1994): 233-256.

Lewin, Joyce C. "The dissolution of silica from diatom walls." *Geochimica et Cosmochimica Acta* 21, no. 3-4 (1961): 182-198.

Liesegang, Moritz, and Ralf Milke. "Australian sedimentary opal-A and its associated minerals: Implications for natural silica sphere formation." *American Mineralogist* 99, no. 7 (2014): 1488-1499.

Liesegang, Moritz, and Frank Tomaschek. "Tracing the continental diagenetic loop of the opal-A to opal-CT transformation with X-ray diffraction." *Sedimentary Geology* 398 (2020): 105603.

Lippincott, Ellis R., Alvin Van Valkenburg, Charles E. Weir, and Elmer N. Bunting. "Infrared studies on polymorphs of silicon dioxide and germanium dioxide." *J. Res. Natl. Bur. Stand* 61, no. 1 (1958): 61-70.

Lynne, Bridget Y., and Kathleen A. Campbell. "Diagenetic transformations (opal-A to quartz) of low-and mid-temperature microbial textures in siliceous hot-spring deposits, Taupo Volcanic Zone, New Zealand." *Canadian Journal of Earth Sciences* 40, no. 11 (2003): 1679-1696.

MacKinnon, Thomas C. "Origin of the Miocene Monterey Formation In California." *Oil in the California Monterey Formation* (1989): 1.

Magoon, Leslie B., and Caroline M. Isaacs. "Chemical characteristics of some crude oils from the Santa Maria basin, California." (1983): 201-211.

Murray, M. J., and J. V. Sanders. "Close-packed structures of spheres of two different sizes II. The packing densities of likely arrangements." *Philosophical Magazine A* 42, no. 6 (1980): 721-740.

Murata, K. J., and J. K. Nakata. "Cristobalitic stage in the diagenesis of diatomaceous shale." *Science* 184, no. 4136 (1974): 567-568.

Murata, K. J., and R. R. Larson. "Diagenesis of Miocene siliceous shales, Temblor range, California." *J. Res. US Geol. Surv* 3, no. 5 (1975): 553-566.

Naidja, A., P. M. Huang, D. W. Anderson, and C. Van Kessel. "Fourier transform infrared, UV-visible, and X-ray diffraction analyses of organic matter in humin, humic acid, and fulvic acid fractions in soil exposed to elevated CO 2 and N fertilization." *Applied spectroscopy* 56, no. 3 (2002): 318-324.

Obradovich, J. D., and C. W. Naeser. "Geochronology bearing on the age of the Monterey Formation and siliceous rocks in California." (1981): 87-95.

O'Keefe, John A. "Natural glass." *Journal of non-crystalline solids* 67, no. 1-3 (1984): 1-17.

Ostrooumov, Mikhail, Emmanuel Fritsch, Bernard Lasnier, and Serge Lefrant. "Spectres Raman des opales; aspect diagnostique et aide a la classification." *European Journal of Mineralogy* 11, no. 5 (1999): 899-908.

Pollack, Sidney S., Harro Lentz, and Wolfgang Ziechmann. "X-ray diffraction study of humic acids." *Soil Science* 112, no. 5 (1971): 318-324.

Rice, S. B., H. Freund, W. L. Huang, J. A. Clouse, and C. M. Isaacs. "Application of Fourier transform infrared spectroscopy to silica diagenesis; the opal-A to opal-CT transformation." *Journal of Sedimentary Research* 65, no. 4a (1995): 639-647.

Rodgers, K. A., P. R. L. Browne, T. F. Buddle, K. L. Cook, R. A. Greatrex, W. A. Hampton, N. R. Herdianita et al. "Silica phases in sinters and residues from geothermal fields of New Zealand." *Earth-Science Reviews* 66, no. 1-2 (2004): 1-61.

Sanders, J. V. "Colour of precious opal." *Nature* 204, no. 4964 (1964): 1151-1153.

Sanders, J. V. "Diffraction of light by opals." *Acta Crystallographica Section A: Crystal Physics, Diffraction, Theoretical and General Crystallography* 24, no. 4 (1968): 427-434.

Sanders, J. V. "Close-packed structures of spheres of two different sizes I. Observations on natural opal." *Philosophical Magazine A* 42, no. 6 (1980): 705-720.

Sangster, A. G., and M. J. Hodson. "Silica in higher plants." *Silicon biochemistry* (1986): 90-107.

Siever, Raymond, and R. A. Scott. "Organic geochemistry of silica." *Organic geochemistry* 14 (1963): 579-595.

Simpson, Tracy L., and Benjamin E. Volcani, eds. *Silicon and siliceous structures in biological systems*. Springer Science, 1981.

Sirotiak, Maroš, and Alica Bartošová. "Changes in structure and content humic substances in soil during the laboratory simulated fires." *TRANSACTIONS of the VŠB–Technical University of Ostrava, Safety Engineering Series* 11, no. 1 (2016): 42-48.

Sodo, A., A. Casanova Municchia, S. Barucca, F. Bellatreccia, G. Della Ventura, F. Butini, and M. A. Ricci. "Raman, FT-IR and XRD investigation of natural opals." *Journal of Raman Spectroscopy* 47, no. 12 (2016): 1444-1451.

Smallwood, A. G., P. S. Thomas, and A. S. Ray. "Characterisation of sedimentary opals by Fourier transform Raman spectroscopy." *Spectrochimica Acta Part A: Molecular and Biomolecular Spectroscopy* 53, no. 13 (1997): 2341-2345.

Tatzel, Michael, Friedhelm von Blanckenburg, Marcus Oelze, Jan A. Schuessler, and Gerhard Bohrmann. "The silicon isotope record of early silica diagenesis." *Earth and Planetary Science Letters* 428 (2015): 293-303.

Weiss, Armin, and A. Herzog. "Isolation and characterization of a silicon-organic complex from plants." In *Biochemistry of silicon and related problems*, pp. 109-127. Springer, Boston, MA, 1978.

Woodring, Wendell Phillips, Milton Nunn Bramlette, and William Stephen Webster Kew. *Geology and paleontology of Palos Verdes Hills, California*. Vol. 207. US Government Printing Office, 1946.

Wyckoff, Ralph WG. "Crystal structure of high temperature cristobalite." *American Journal of Science* 54 (1925): 448-459.

APPENDIX A

X-RAY DIFFRACTION OF BULK SILICA EXPERIMENTS

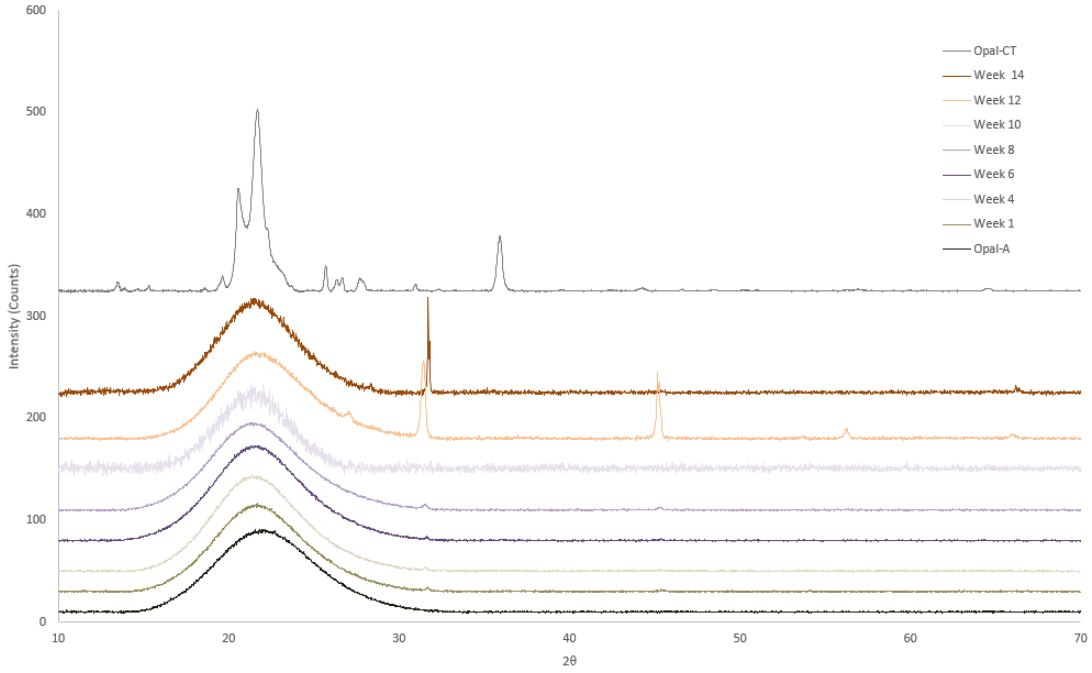

Figure 26: Compiled Graph of X-ray diffractograms of bulk silica experiments.

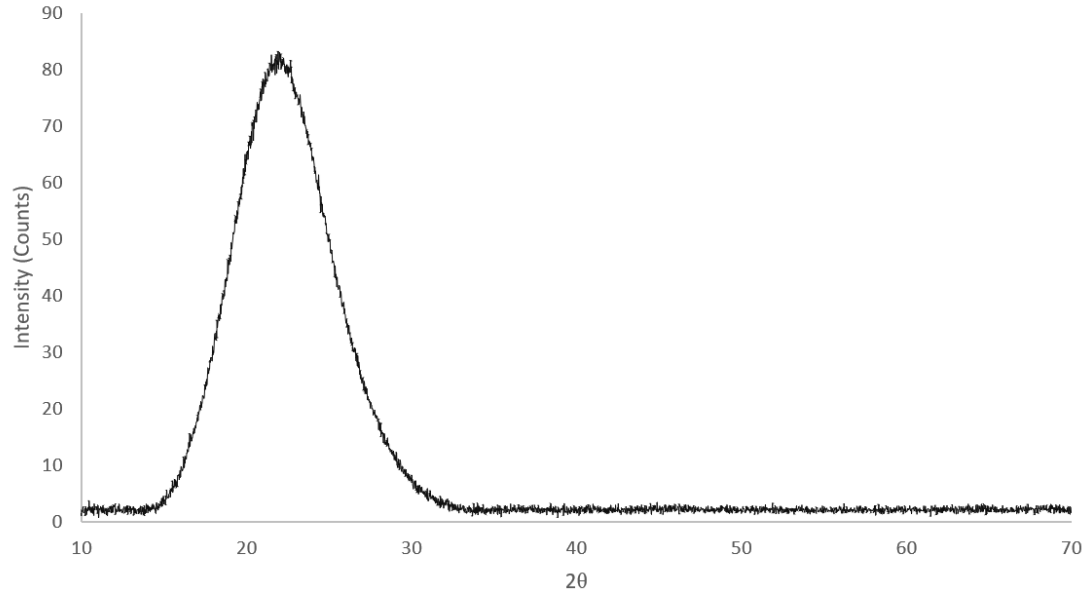

Figure 27: X-ray diffractogram of opal-A standard (silica gel).

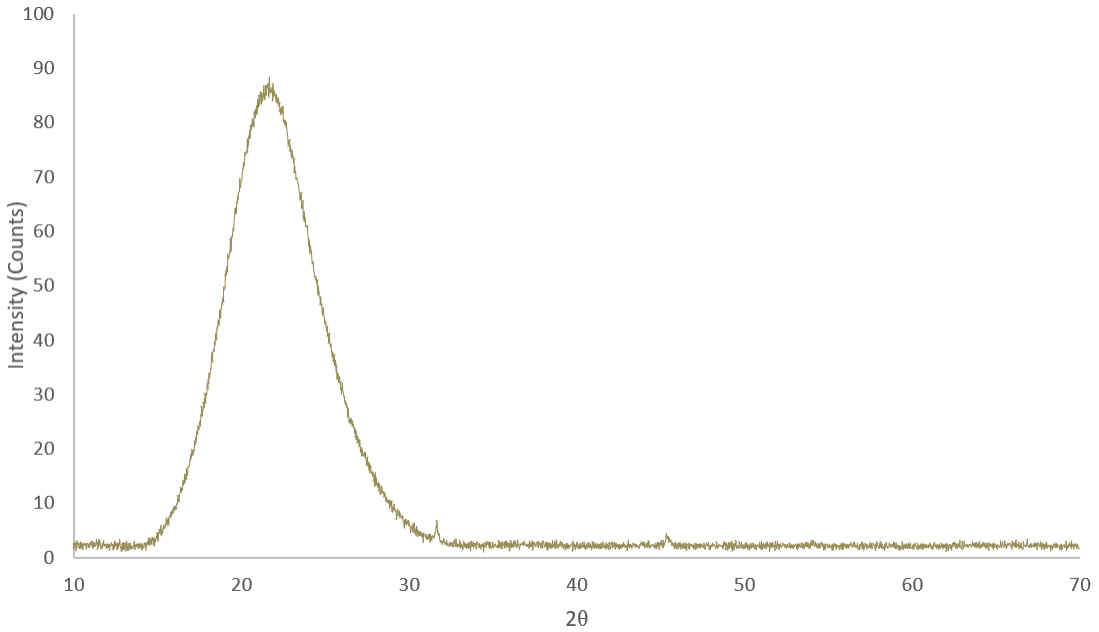

Figure 28: X-ray diffractogram of 1-week sample.

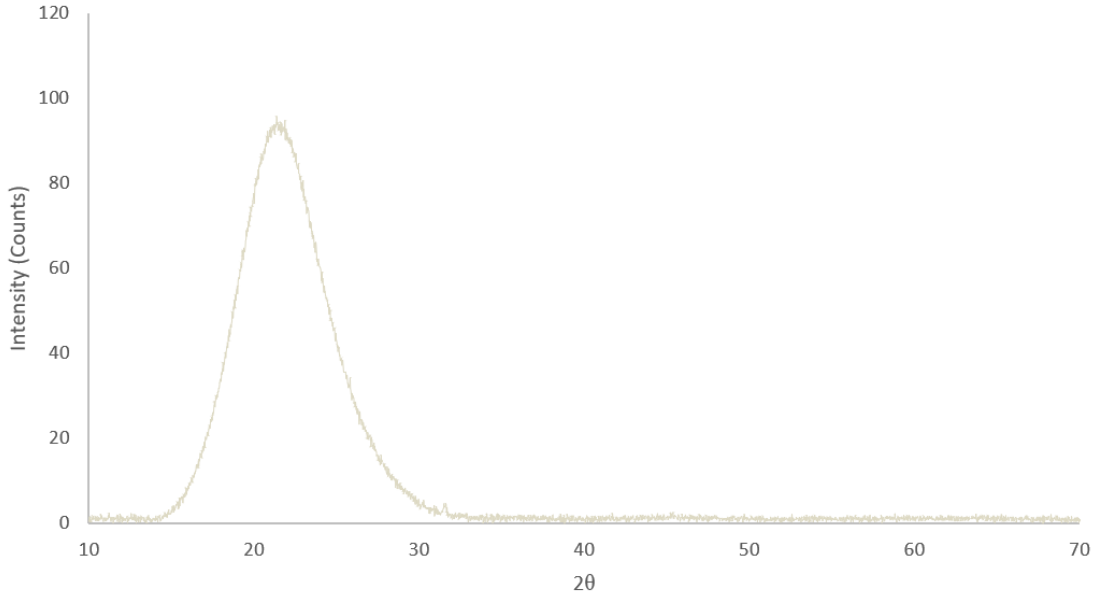

Figure 29: X-ray diffractogram of 4-week sample.

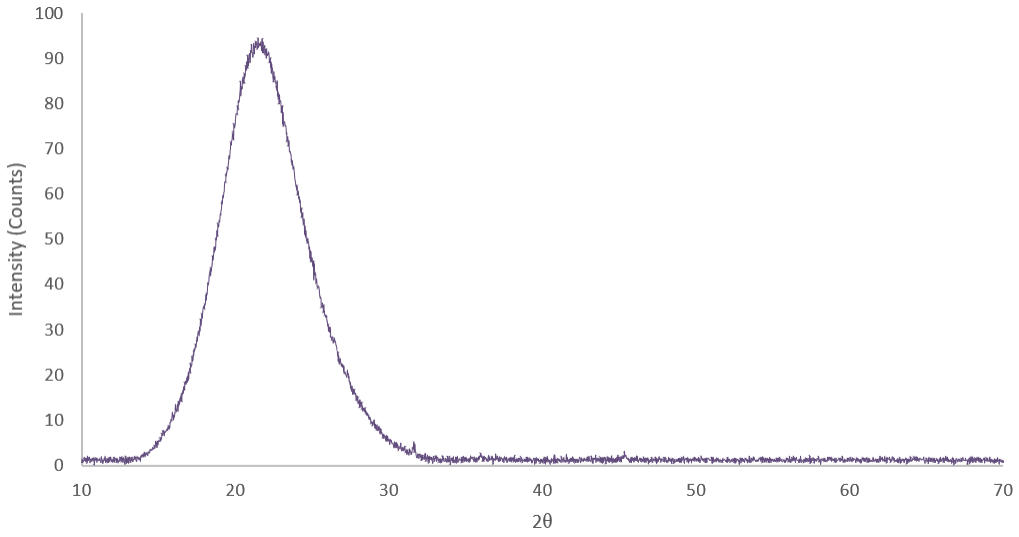

Figure 30: X-ray diffractogram of 6-week sample.

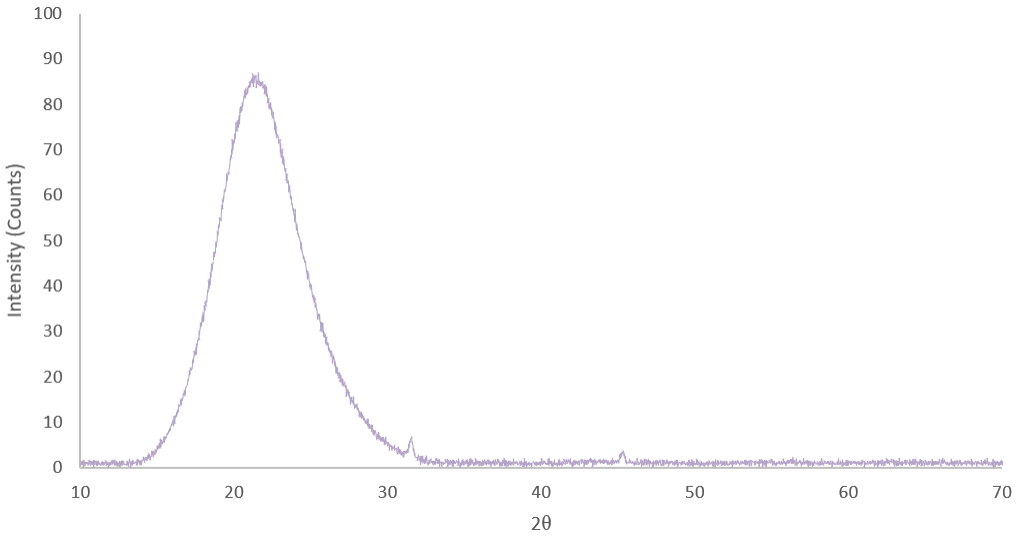

Figure 31: X-ray diffractogram of 8-week sample.

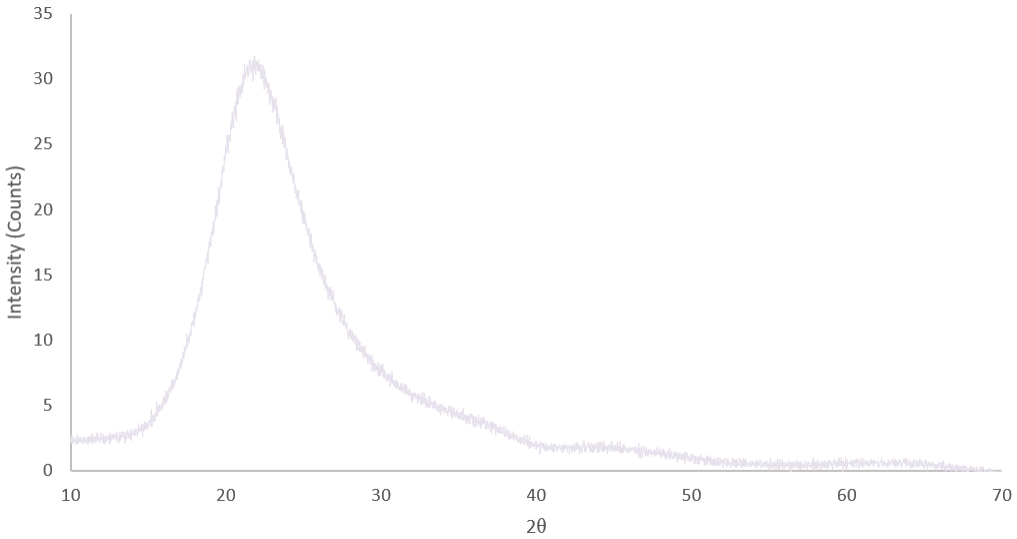

Figure 32: X-ray diffractogram of 10-week sample.

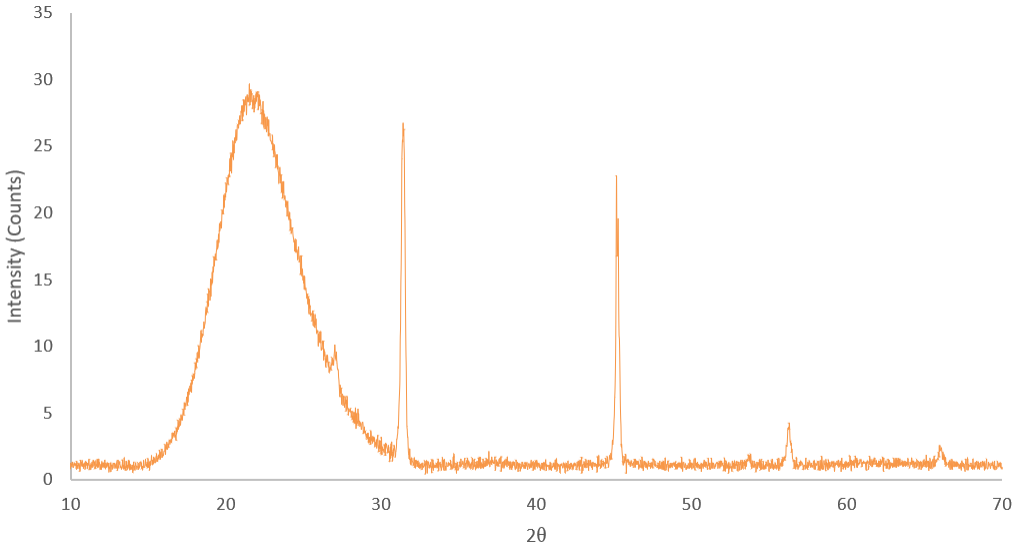

Figure 33: X-ray diffractogram of 12-week sample.

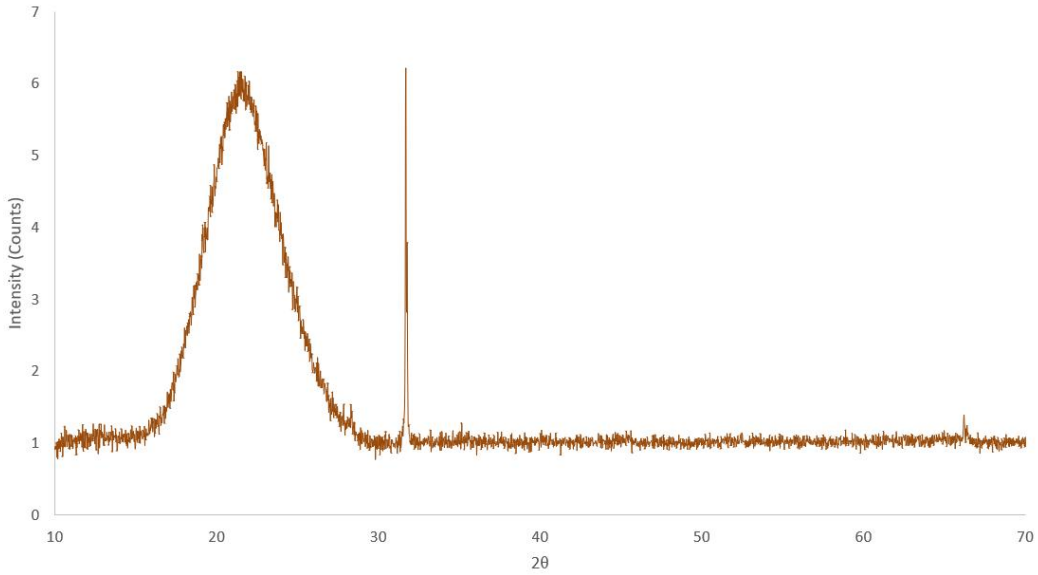

Figure 34: X-ray diffractogram of 14-week sample.

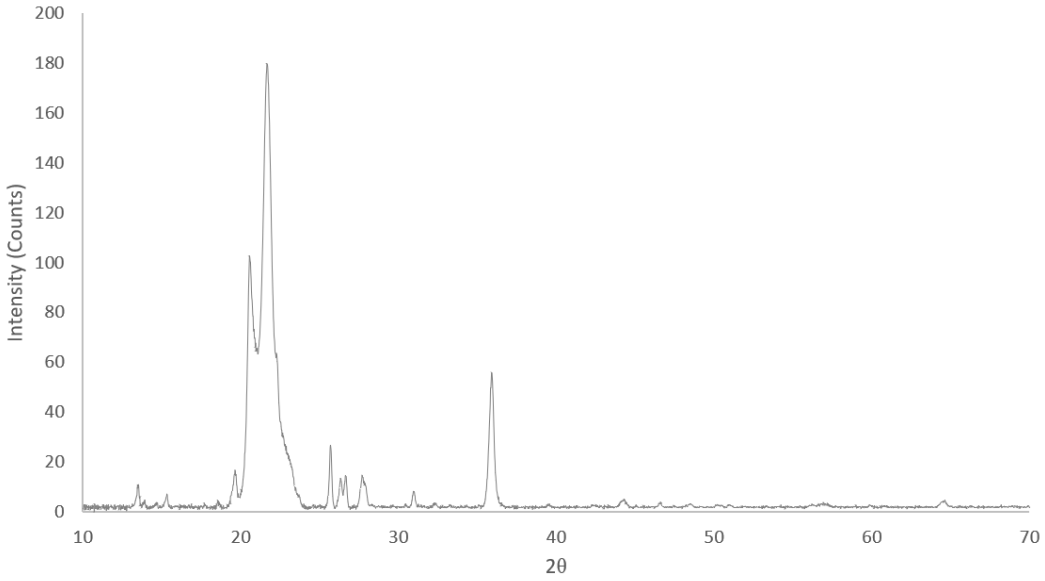

Figure 35: X-ray diffractogram of opal-CT standard.

APPENDIX B

PEAK FITTING OF BULK X-RAY DIFFRACTION

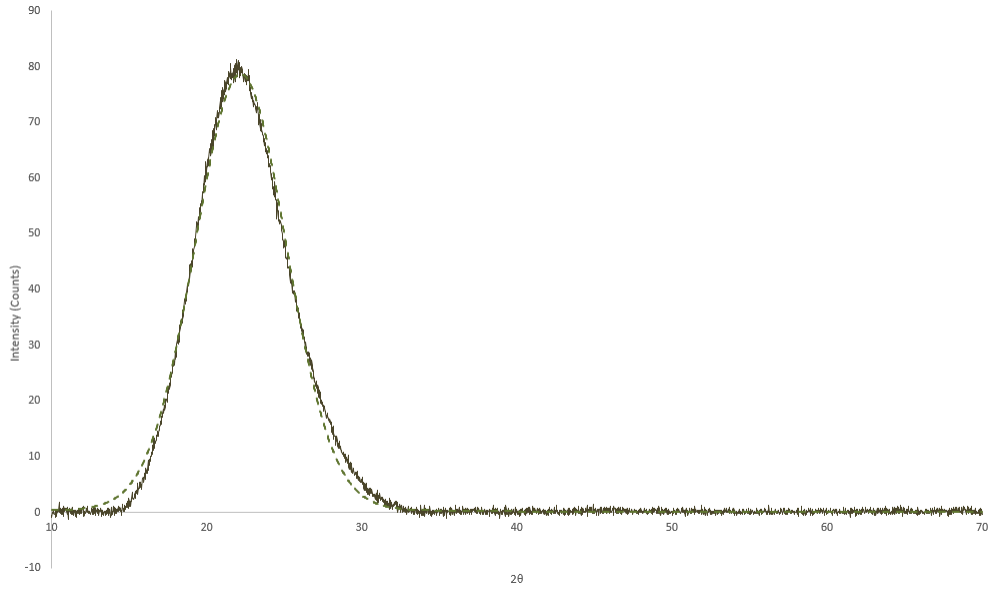

Figure 36: Peak fitting (dotted line) of opal-a standard (silica gel).

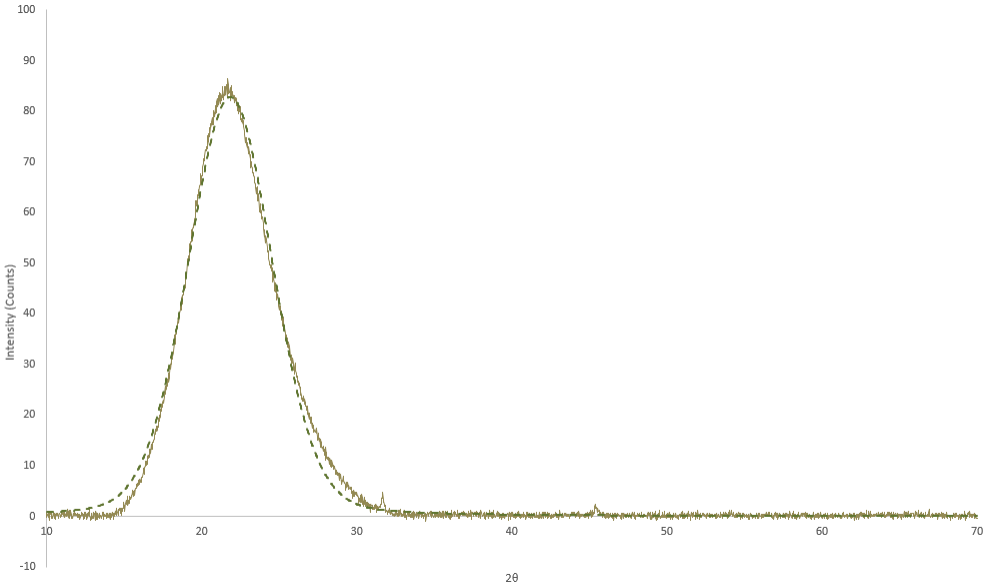

Figure 37: Peak fitting (dotted line) of 1-week sample.

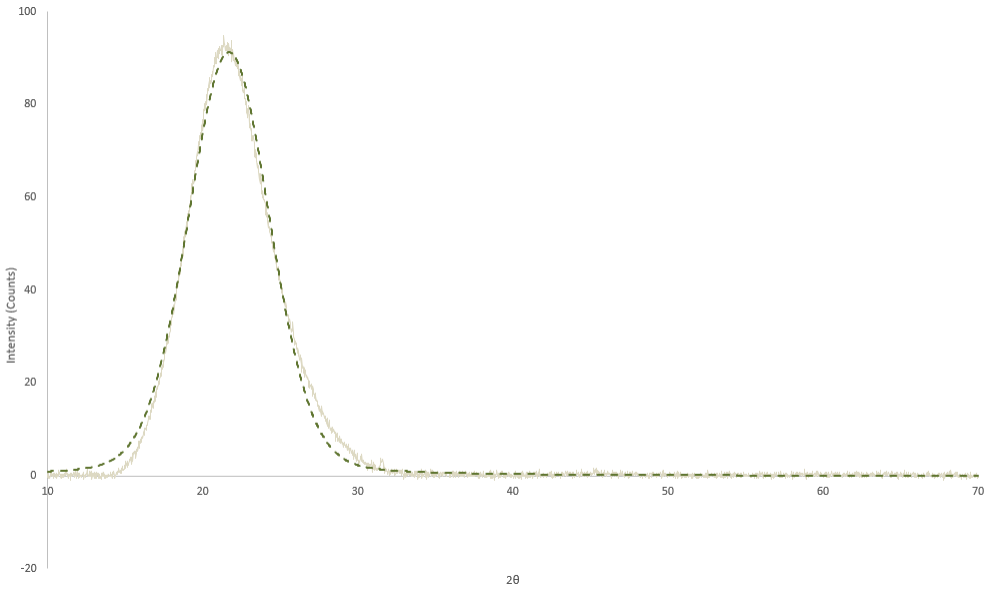

Figure 38: Peak fitting (dotted line) of 4-week sample.

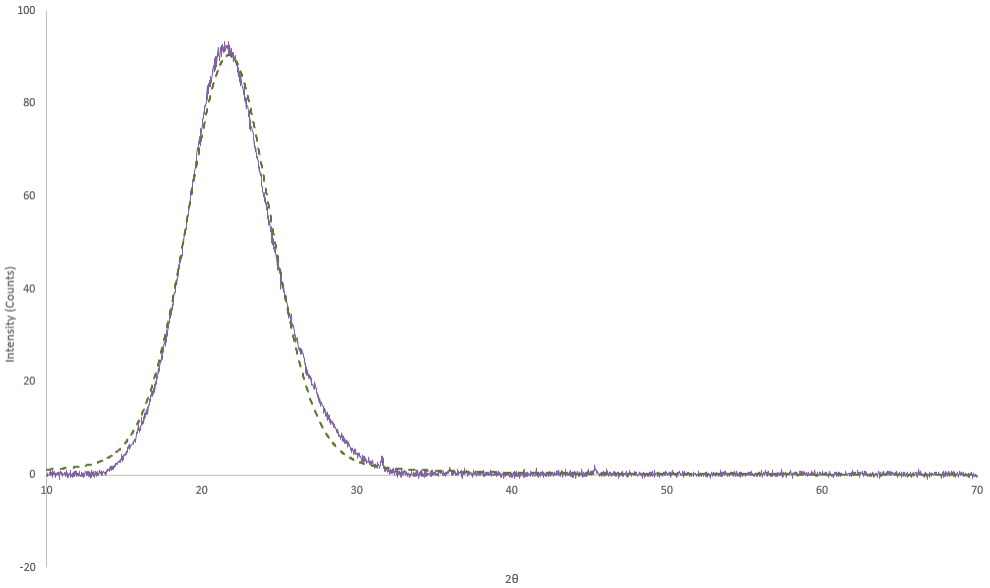

Figure 39: Peak fitting (dotted line) of 6-week sample.

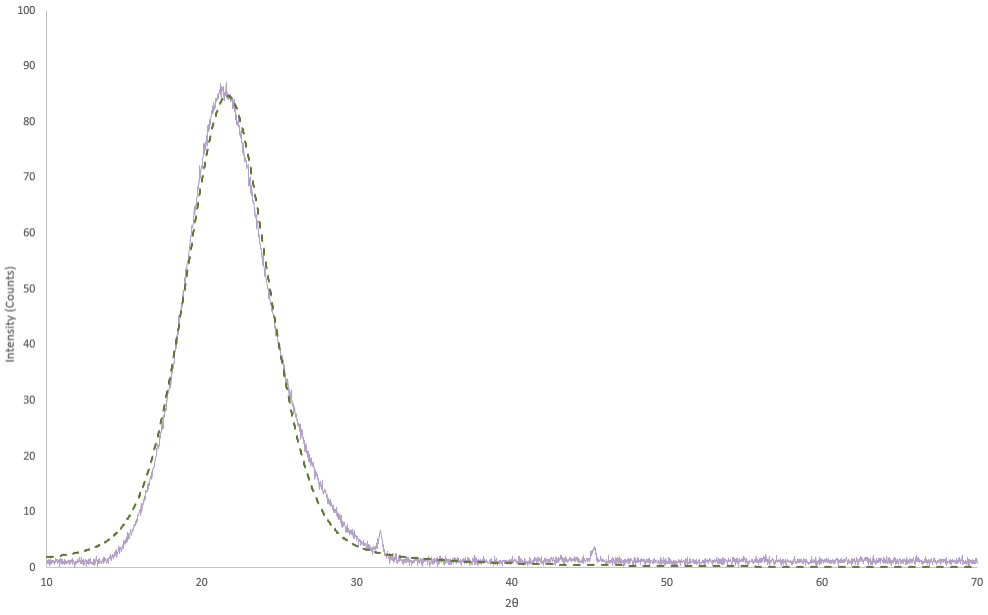

Figure 40: Peak fitting (dotted line) of 8-week sample.

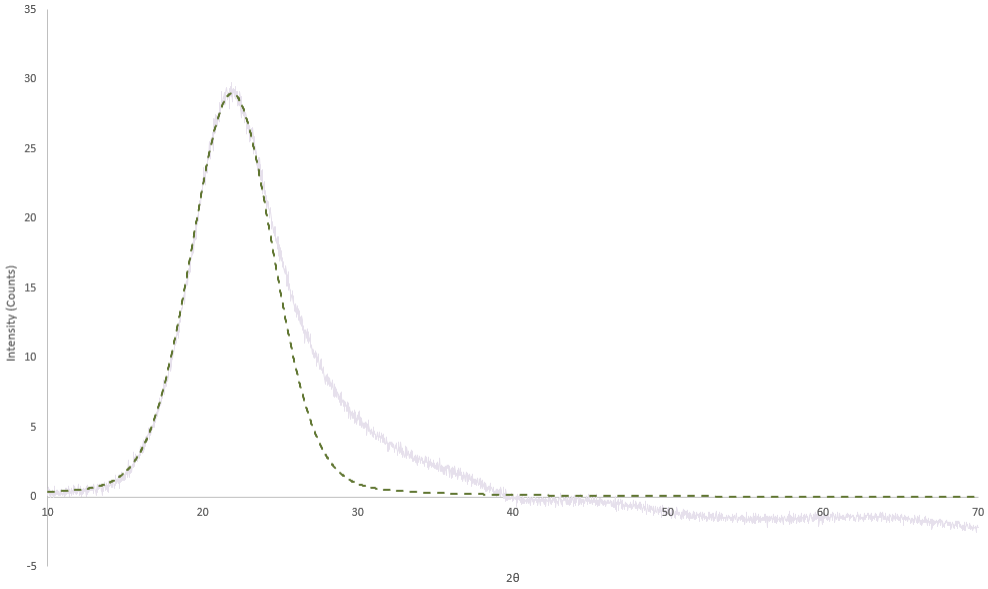

Figure 41: Peak fitting (dotted line) of 10-week sample.

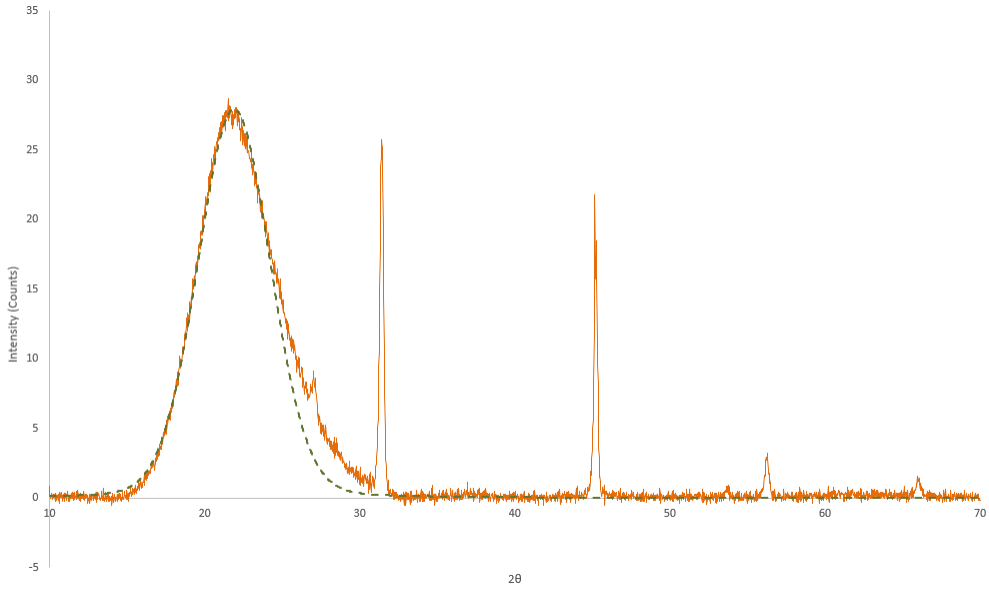

Figure 42: Peak fitting (dotted line) of 12-week sample.

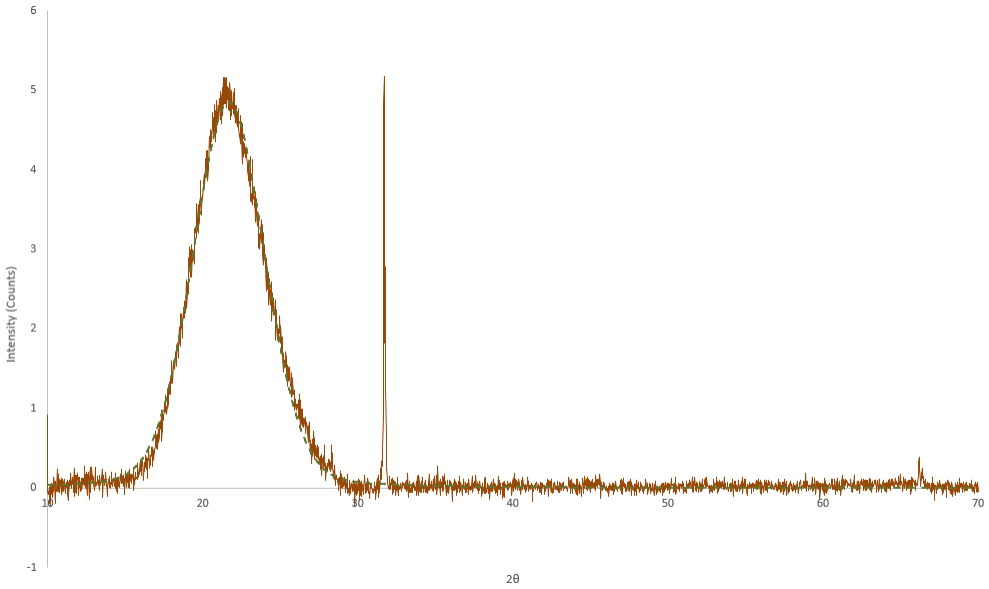

Figure 43: Peak fitting (dotted line) of 14-week sample.

APPENDIX C

FOURIER-TRANSFORM INFRARED OF BULK EXPERIMENTS

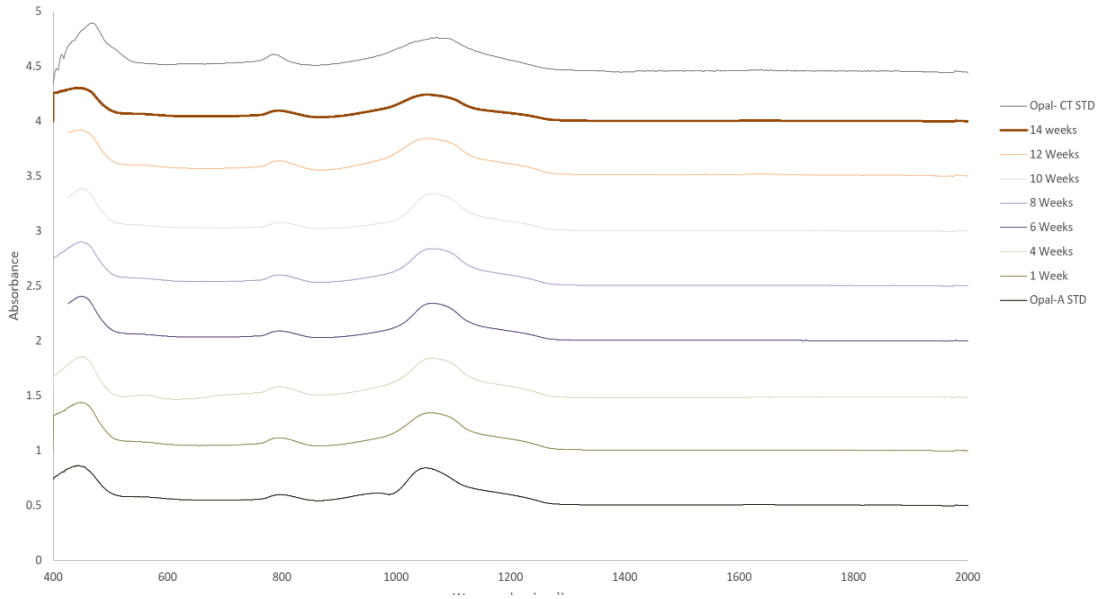

Figure 44: Compiled Fourier-transform infrared spectroscopy of all bulk experiment samples (offset in the vertical).

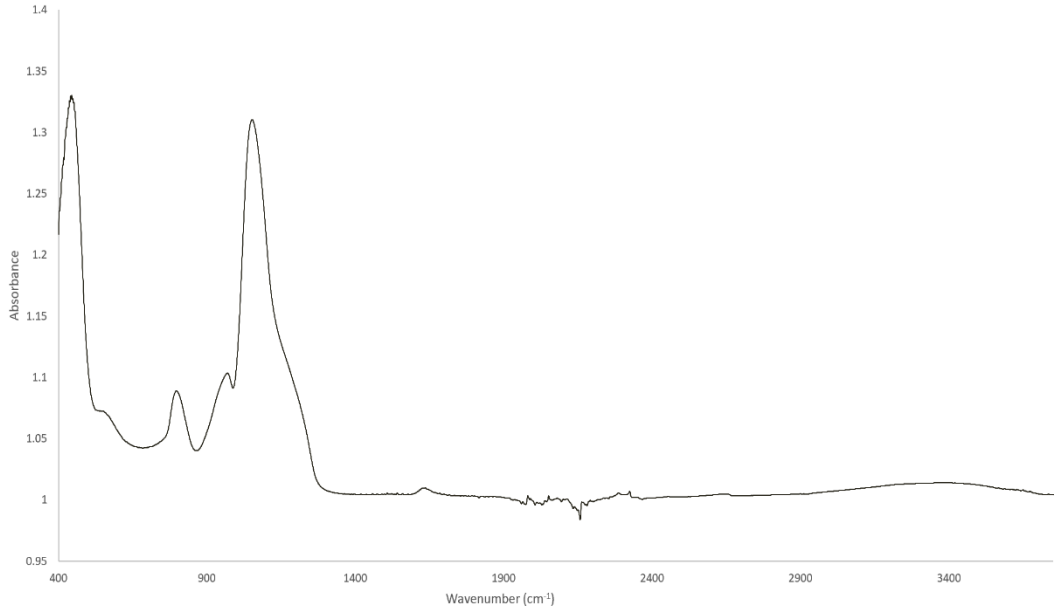

Figure 45: Fourier-transform infrared spectroscopy of the opal-A standard.

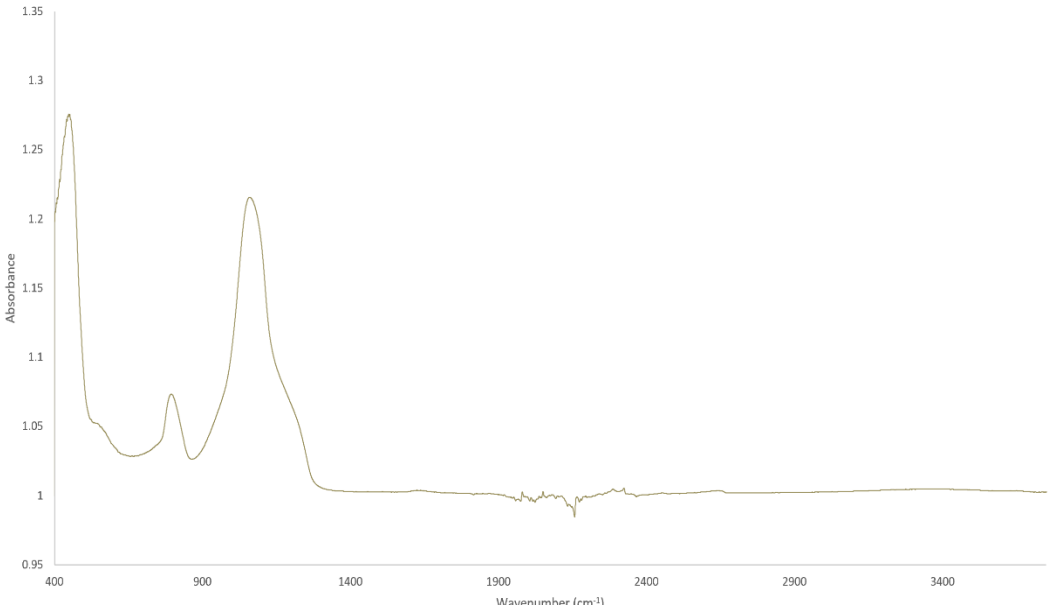

Figure 46: Fourier-transform infrared spectroscopy of week-1 sample.

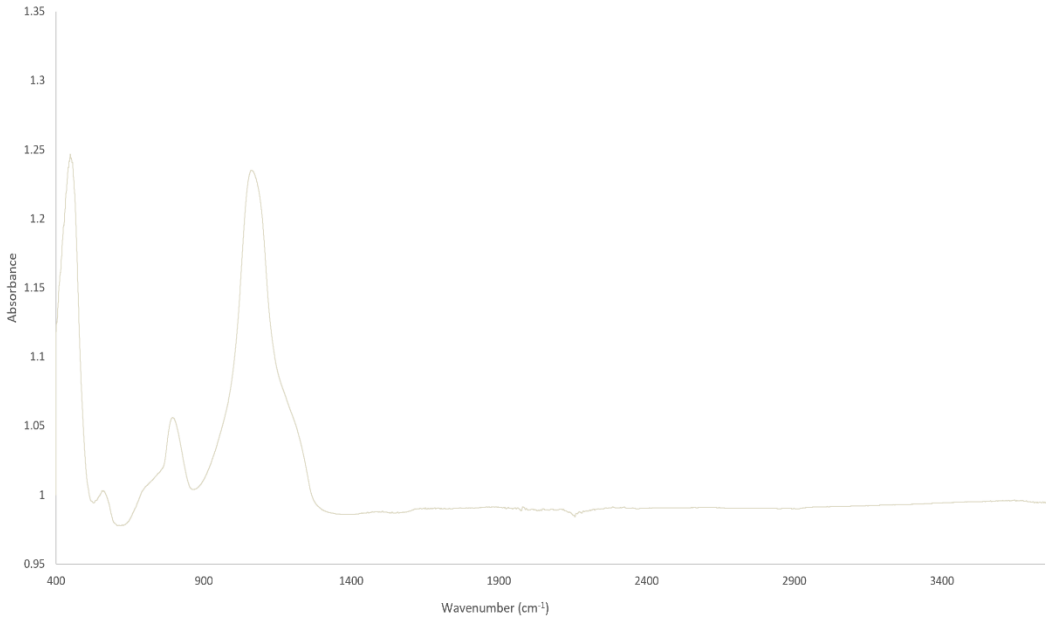

Figure 47: Fourier-transform infrared spectroscopy of week-4 sample.

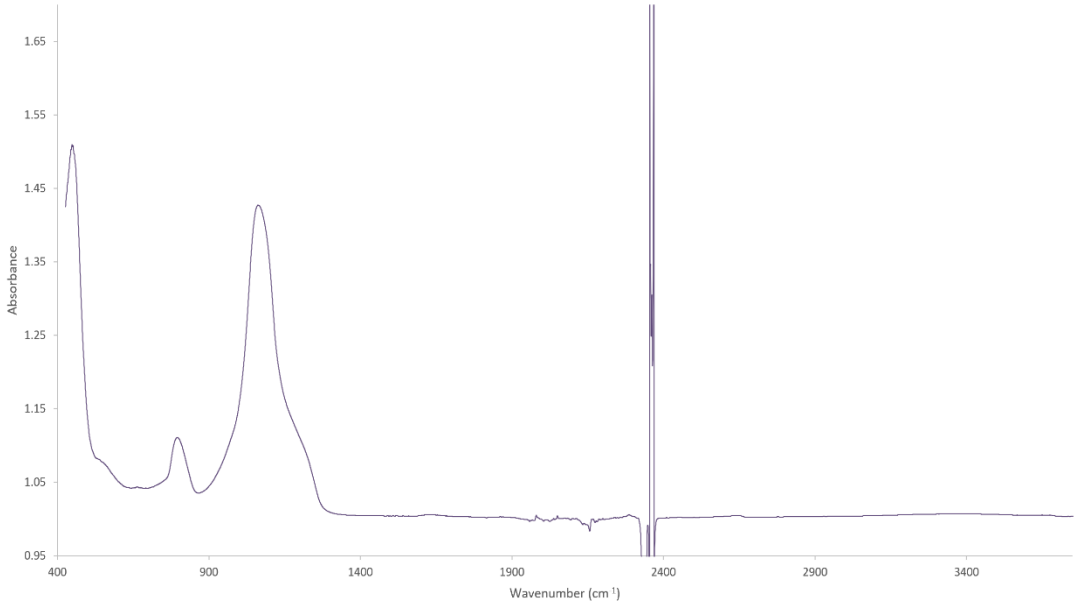

Figure 48: Fourier-transform infrared spectroscopy of week-6 sample. Large spike around 2400 cm^{-1} is an artifact from experimentation.

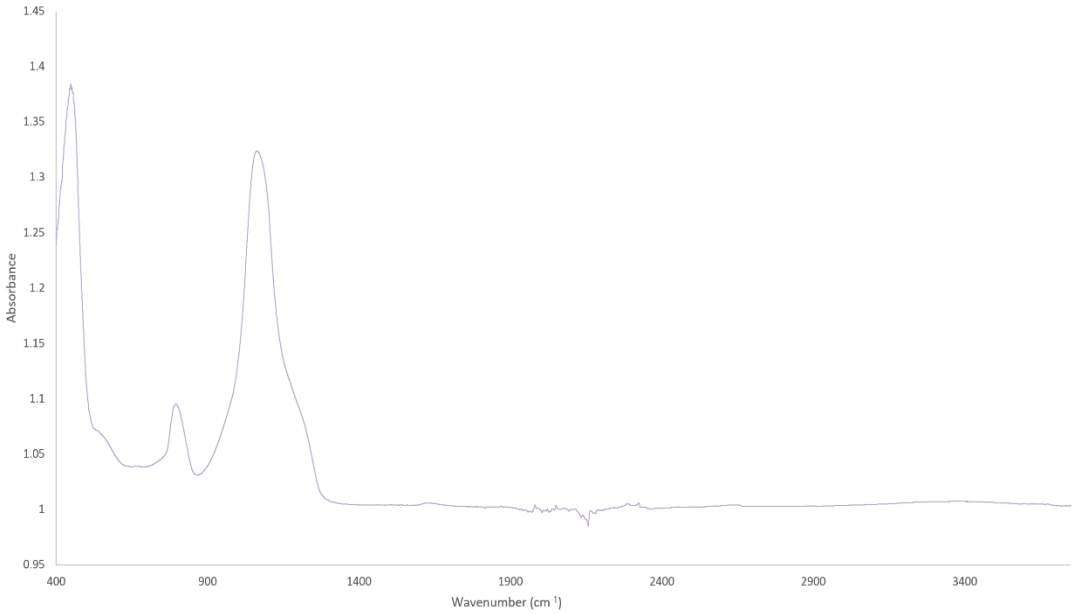

Figure 49: Fourier-transform infrared spectroscopy of week-8 sample.

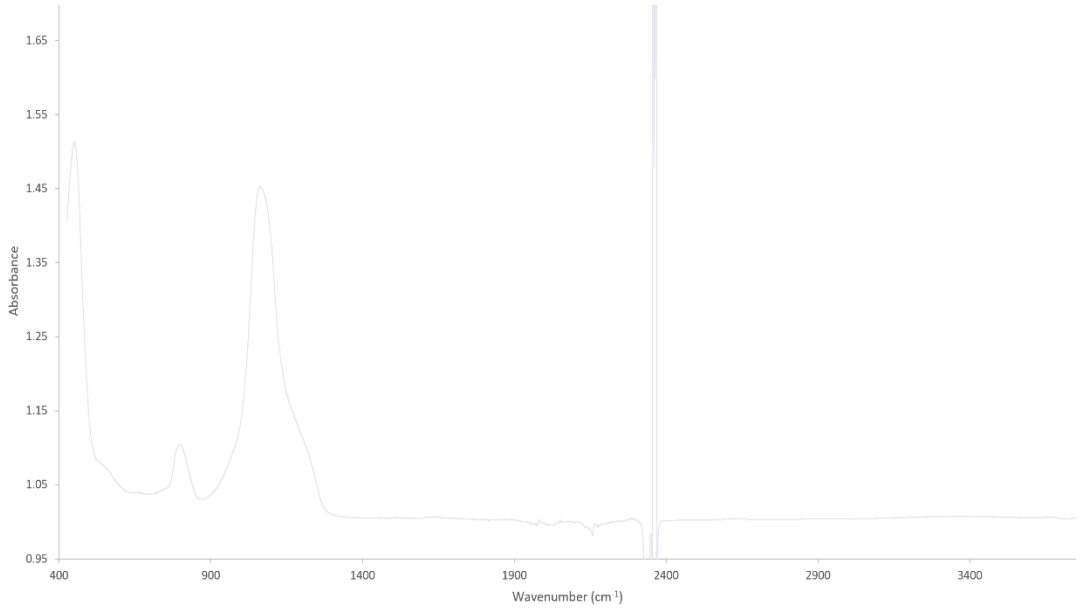

Figure 50: Fourier-transform infrared spectroscopy of week-10 sample. Large spike around 2400 cm^{-1} is an artifact from experimentation.

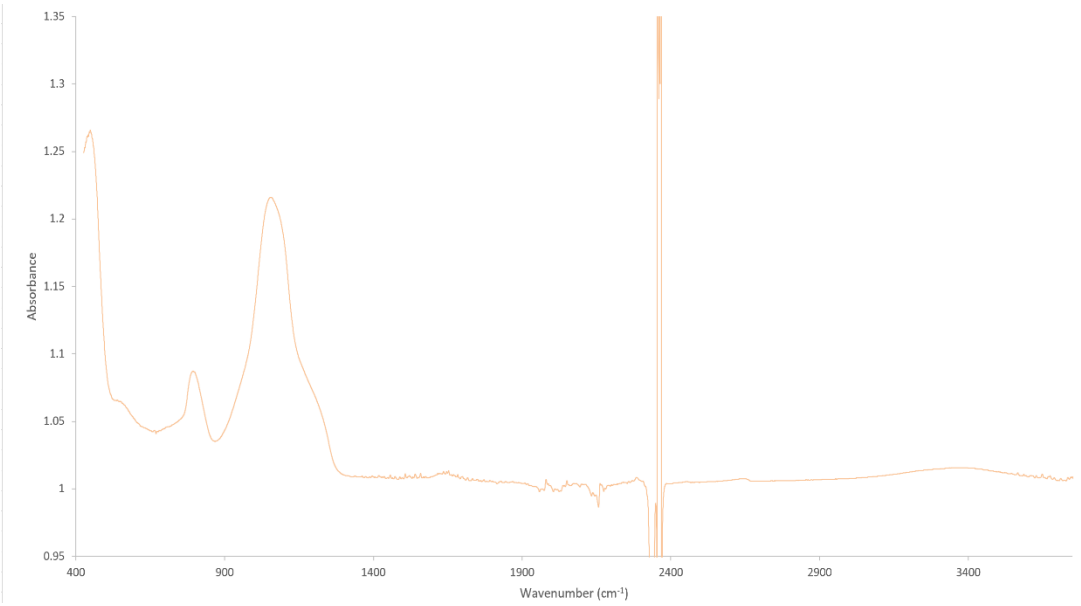

Figure 51: Fourier-transform infrared spectroscopy of week-12 sample. Large spike around 2400 cm^{-1} is an artifact from experimentation.

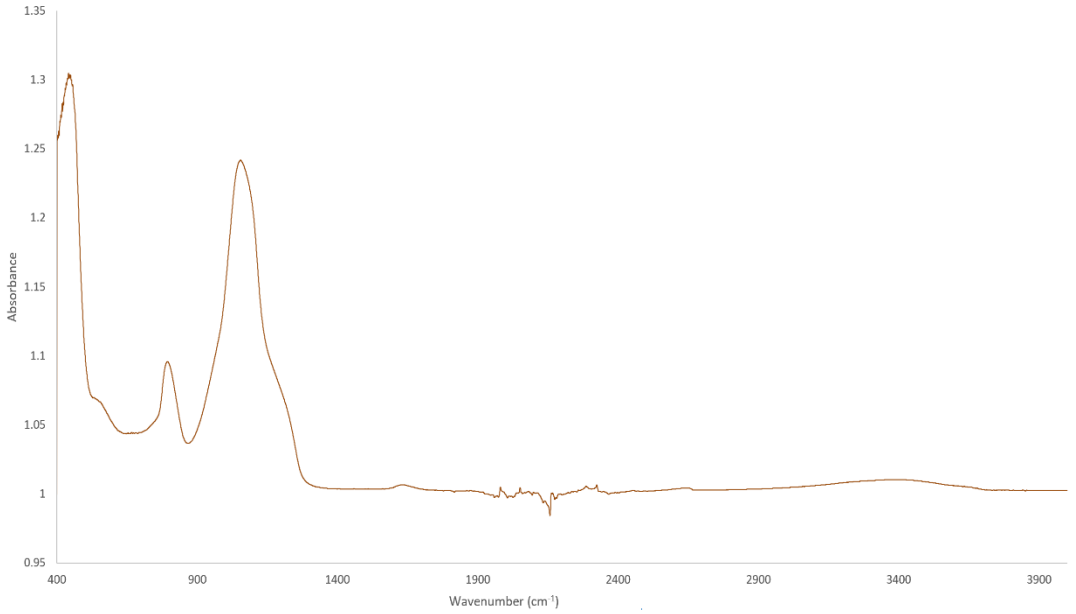

Figure 52: Fourier-transform infrared spectroscopy of week-14 sample. Large spike around 2400 cm^{-1} is an artifact from experimentation.

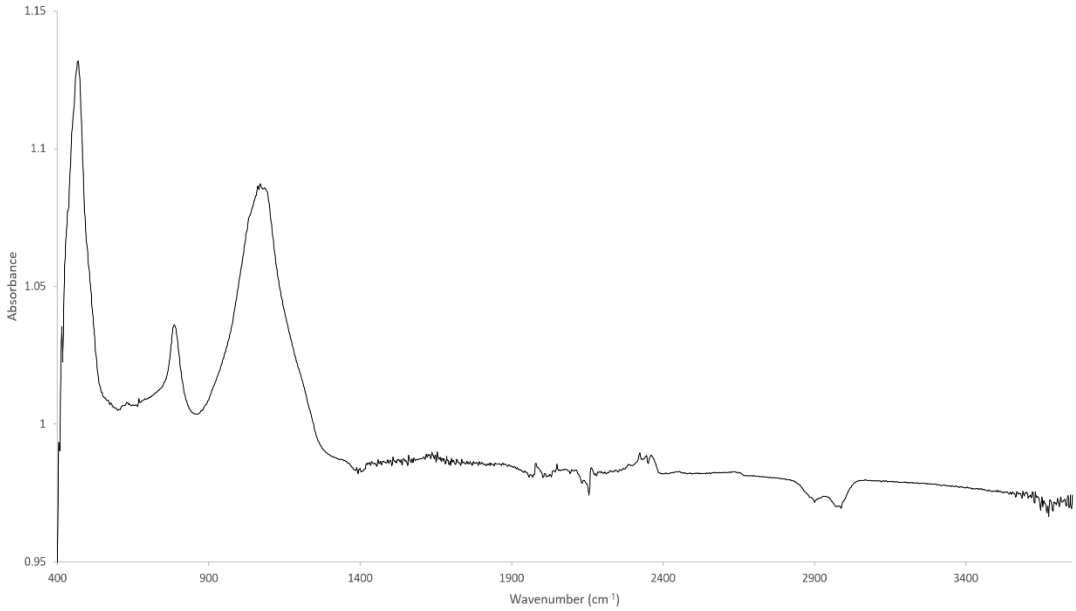

Figure 53: Fourier-transform infrared spectroscopy of the opal-CT standard.

APPENDIX D

RAMAN SPECTROSCOPY RESULTS OF BULK EXPERIMENTS

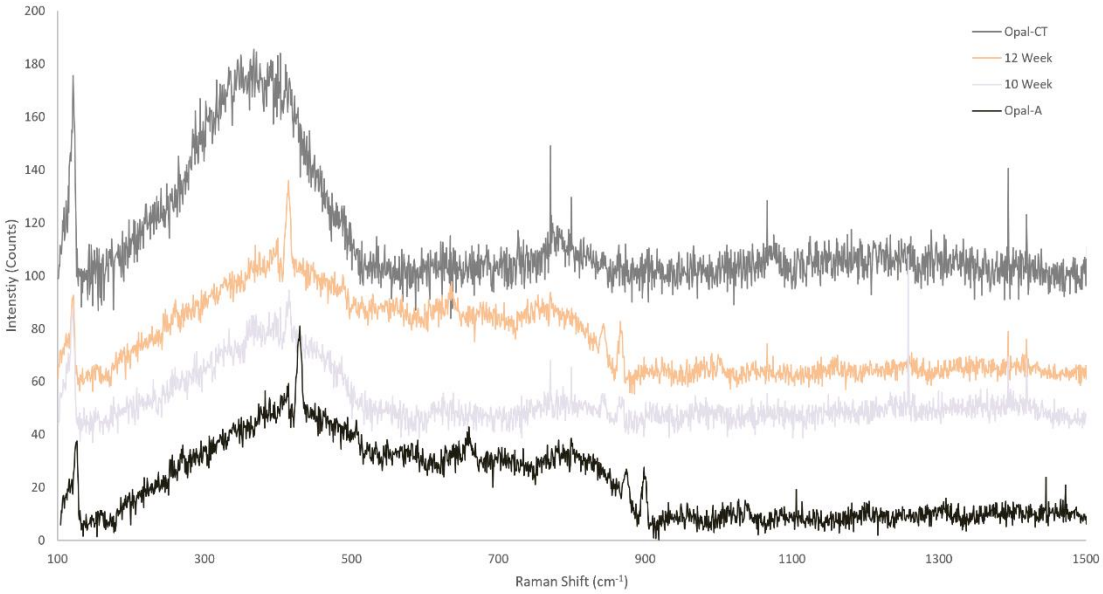

Figure 54: Raman spectroscopy of bulk experiments (offset in the vertical).

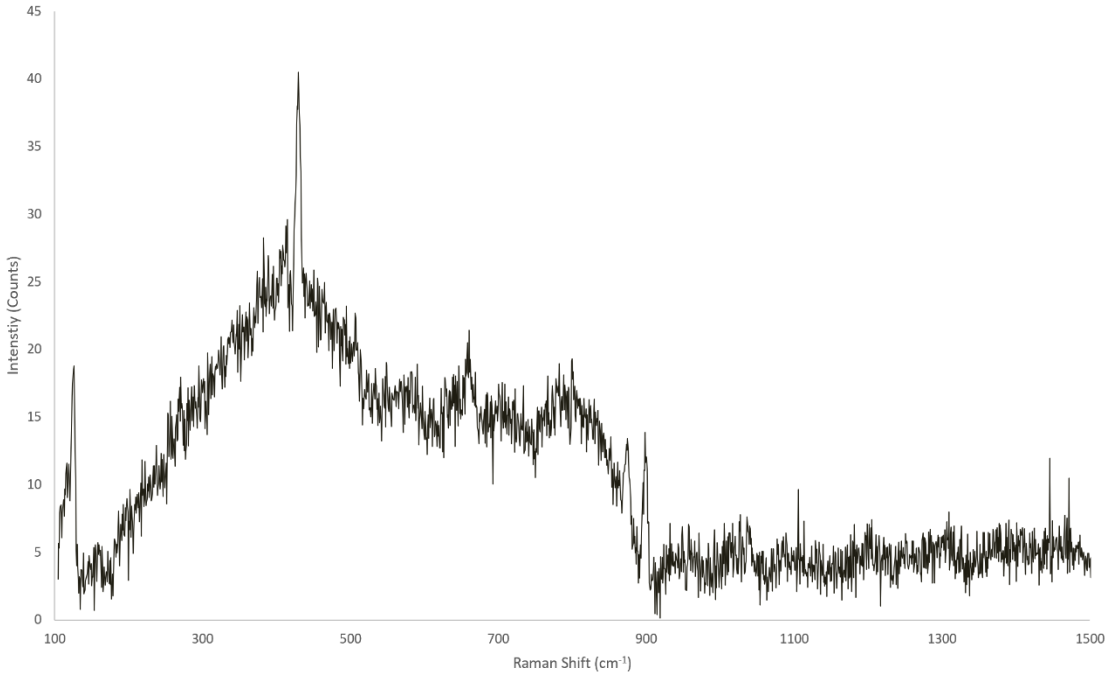

Figure 55: Raman spectroscopy of opal-A standard.

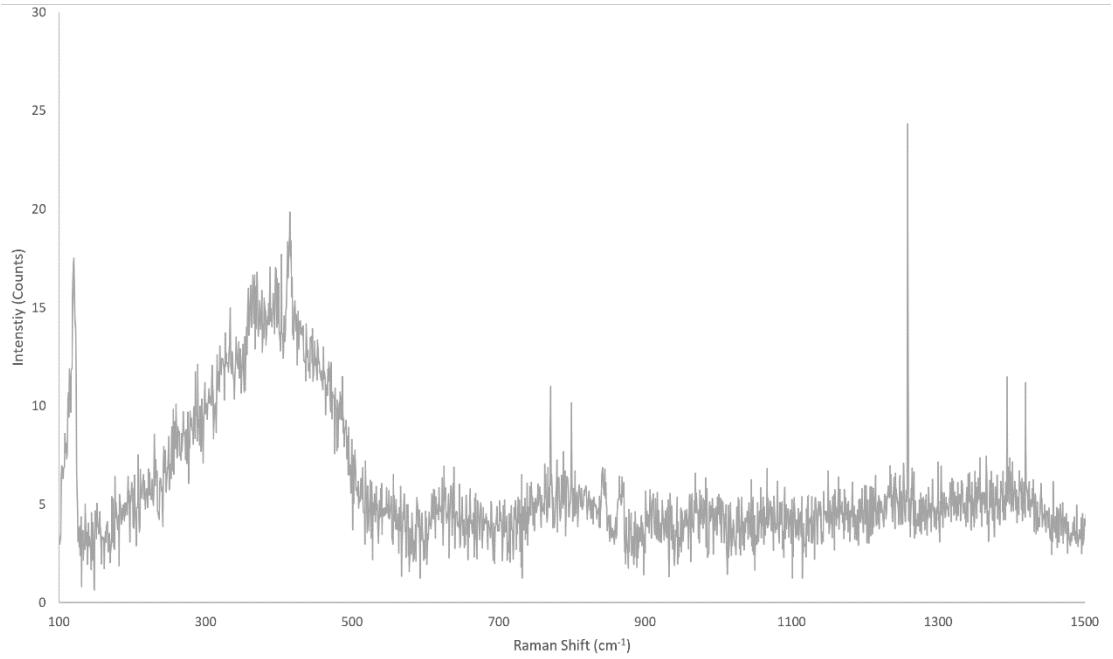

Figure 56: Raman spectroscopy of week-10 sample.

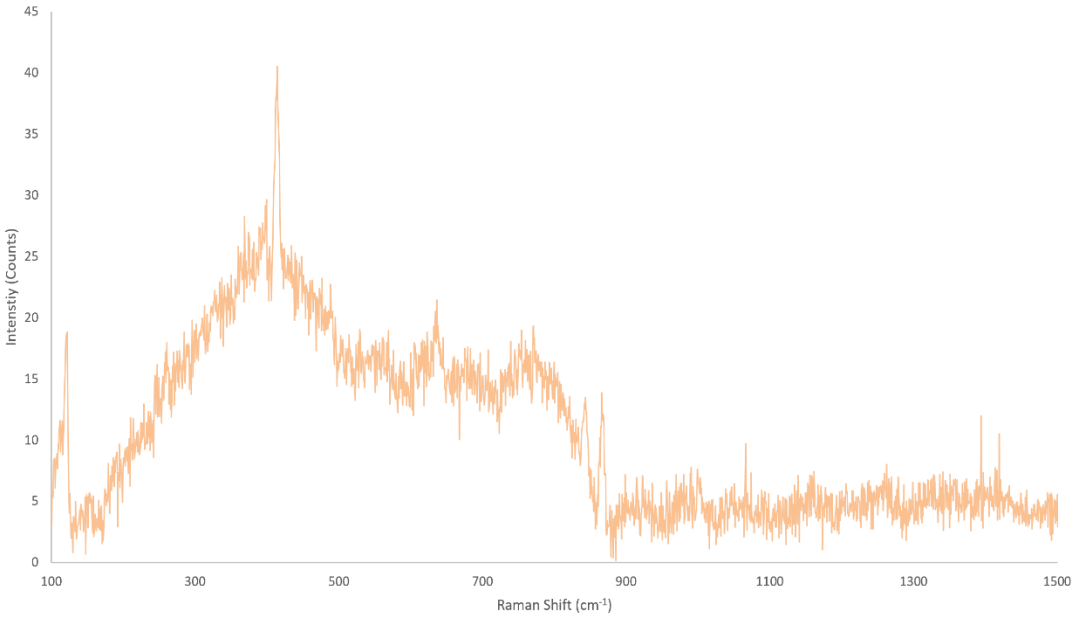

Figure 57: Raman spectroscopy of week-14 sample.

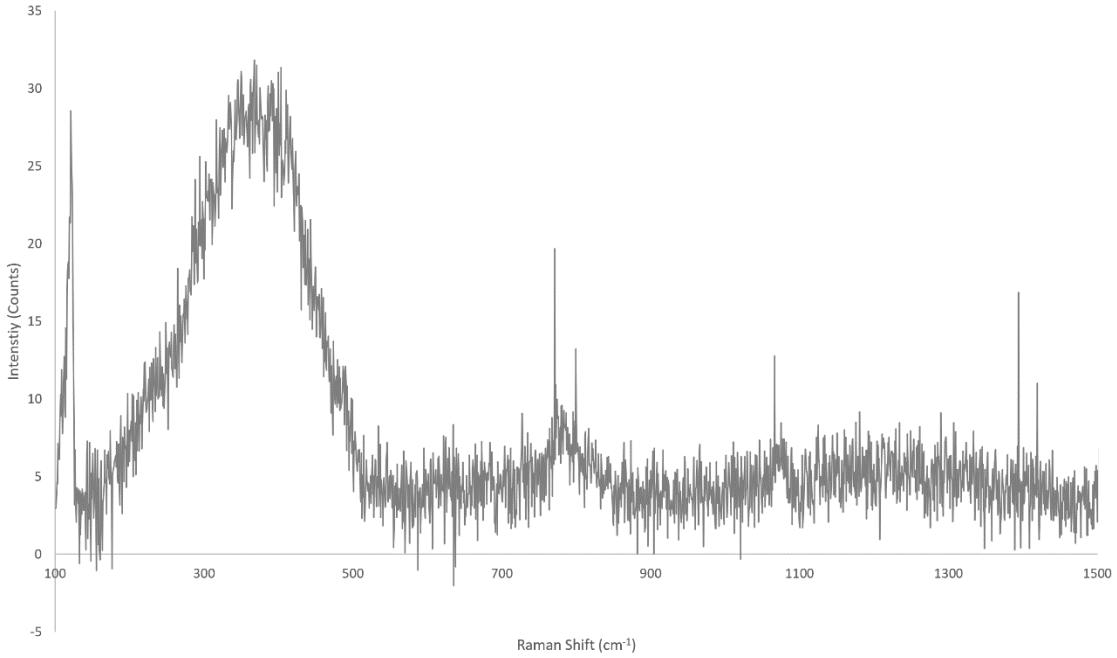

Figure 58: Raman spectroscopy of the opal-CT standard.

APPENDIX E

SPATIALLY RESOLVED X-RAY DIFFRACTOGRAMS WITH HALITE PEAKS

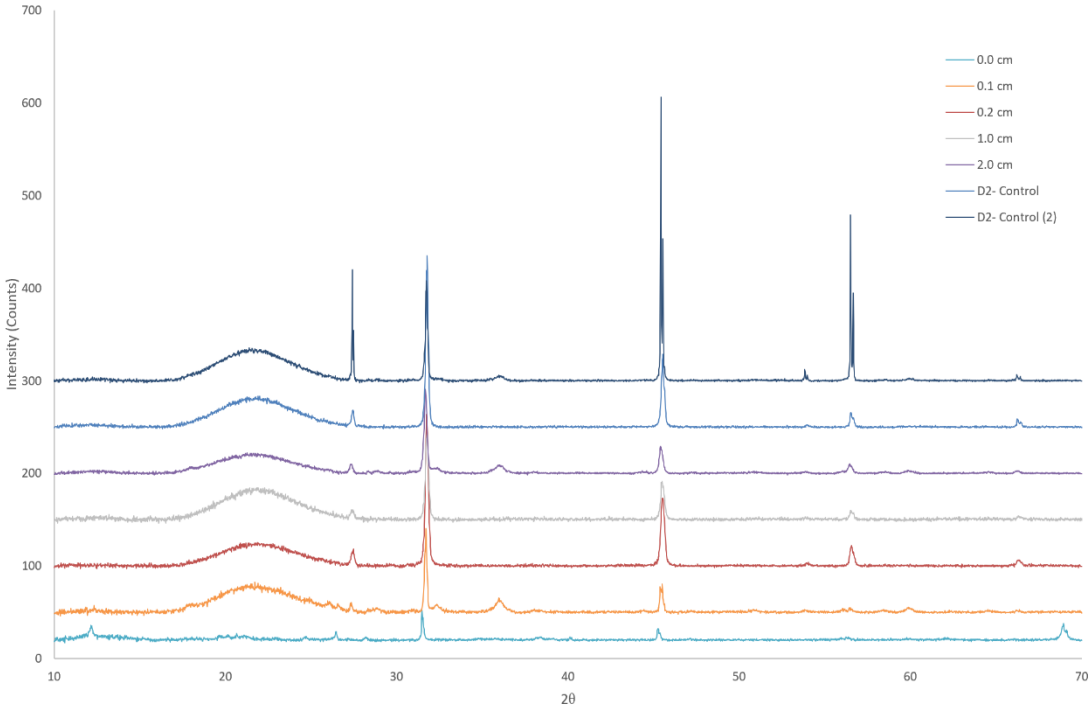

Figure 59: Compiled X-ray diffraction results of stratified experiment "B2" with coordinating controls "D2".

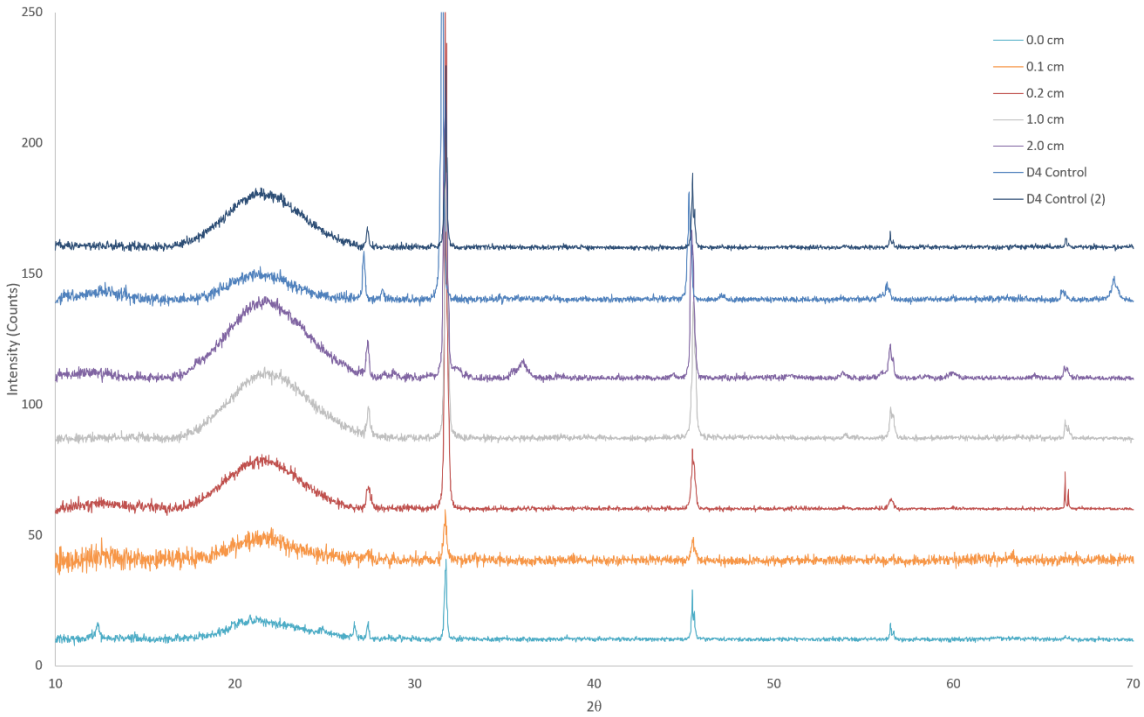

Figure 60: Compiled X-ray diffraction results of stratified experiment "B4" with coordinating controls "D4".

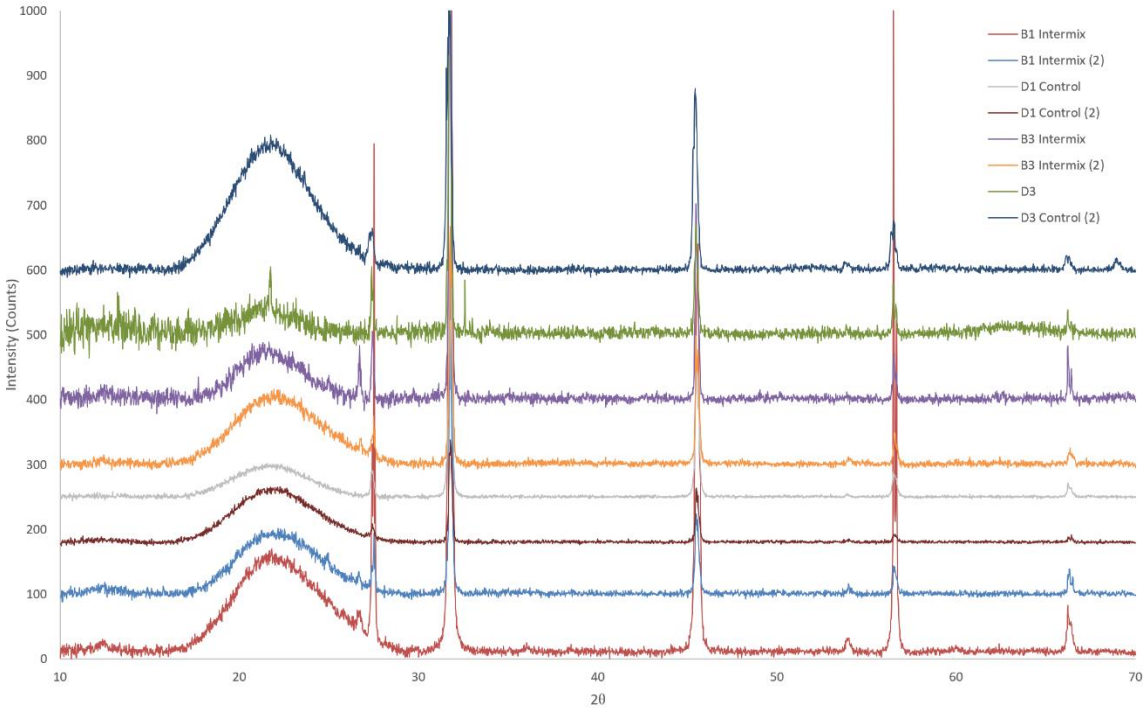

Figure 61: Compiled X-ray diffraction results of intermixed experiments "B1" and "B3" with coordinating controls "D1" and "D3".

APPENDIX F

SPATIALLY RESOLVED X-RAY DIFFRACTOGRAMS WITH HALITE PEAKS MASKED

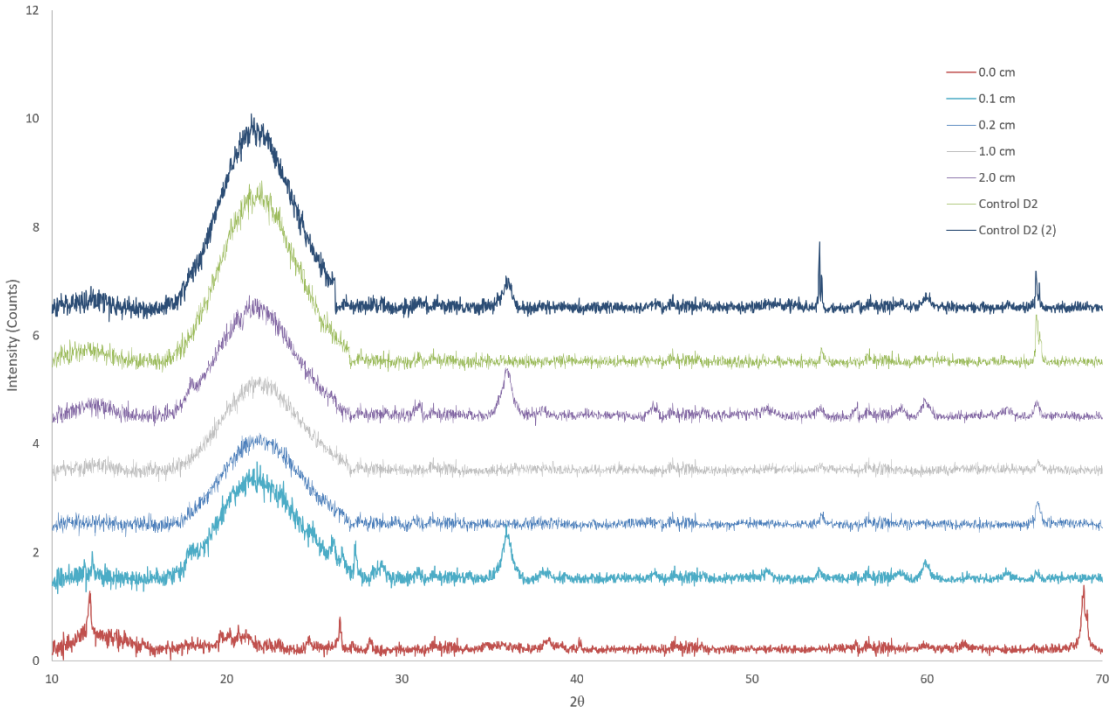

Figure 62: Compiled X-ray diffraction results of stratified experiment “B2” with coordinating controls “D2” with halite peaks masked.

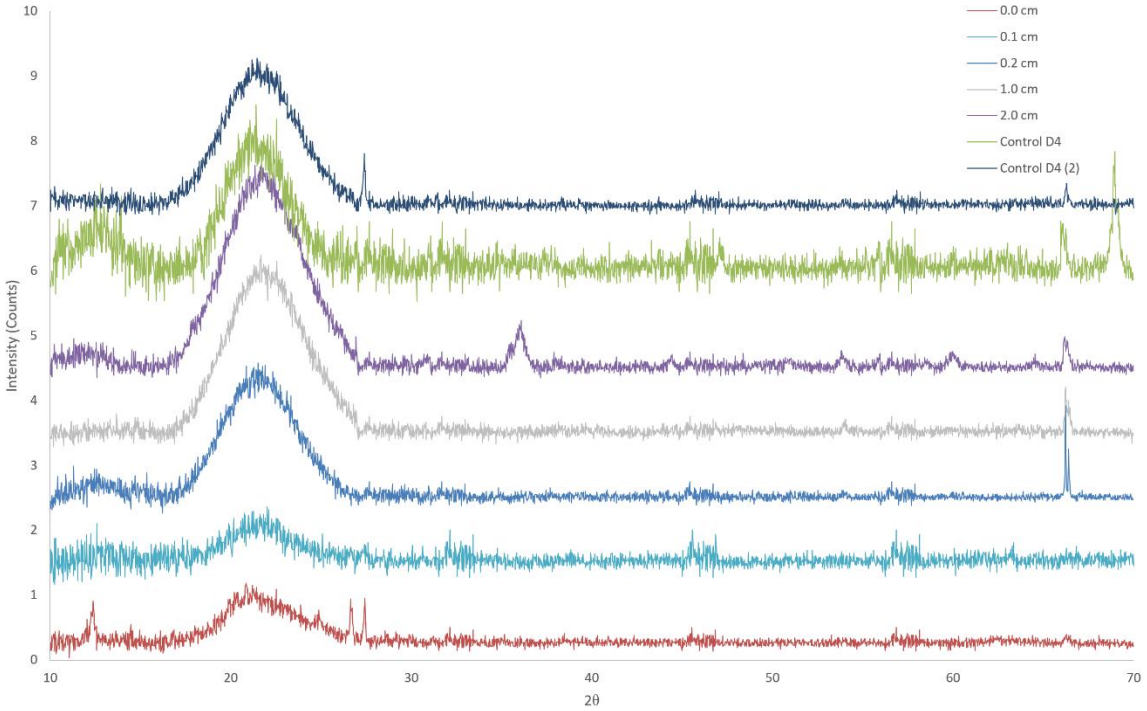

Figure 63: Compiled X-ray diffraction results of stratified experiment "B4" with coordinating controls "D4" with halite peaks masked.

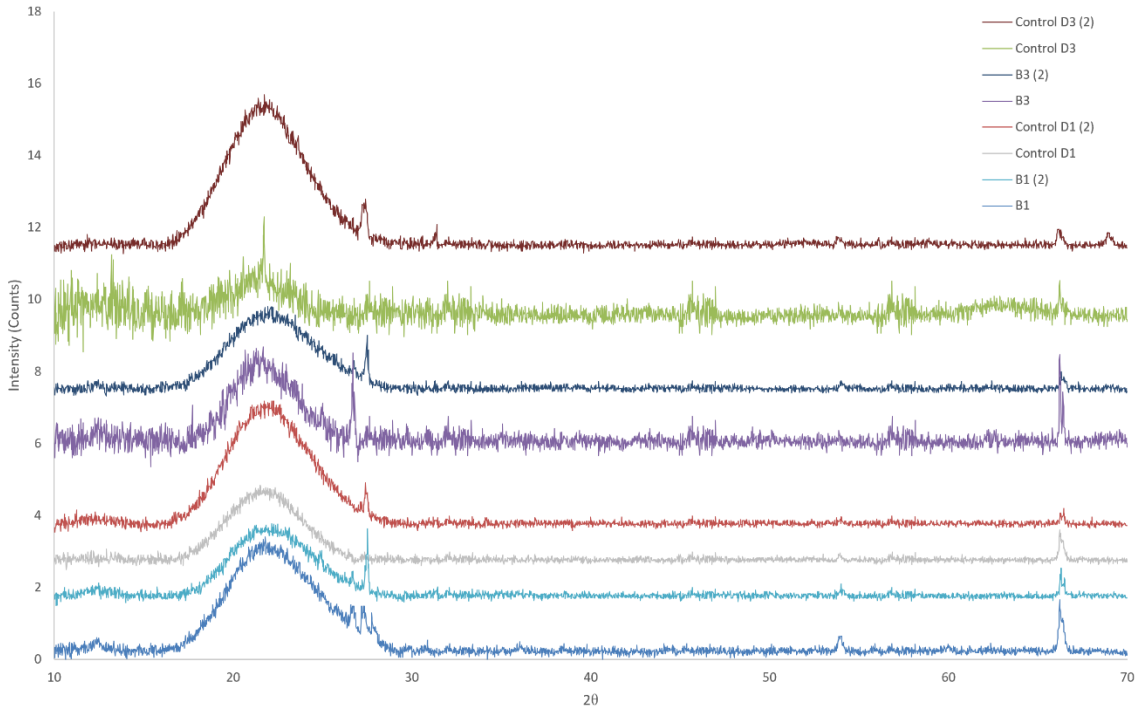

Figure 64: Compiled X-ray diffraction results of intermixed experiments "B1" and "B3" with coordinating controls "D1" and "D3" with halite peaks masked.

APPENDIX G

FOURIER-TRANSFORM INFRARED SPECTROSCOPY OF SPATIALLY RESOLVED EXPERIMENTS

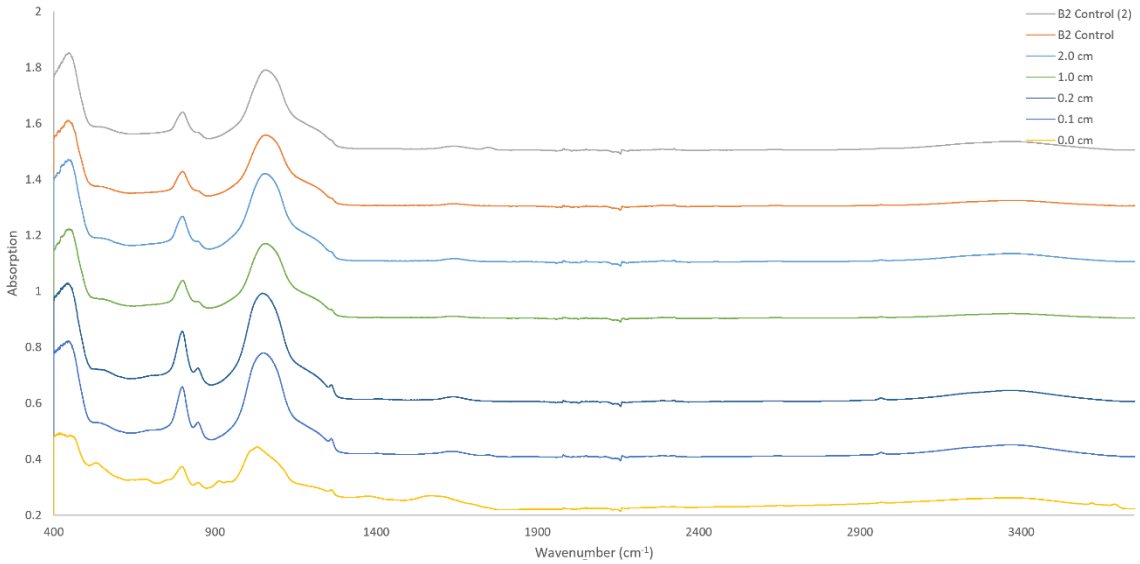

Figure 65: Compiled Fourier-transform infrared spectroscopy results of stratified experiment "B2" with coordinating controls "D2".

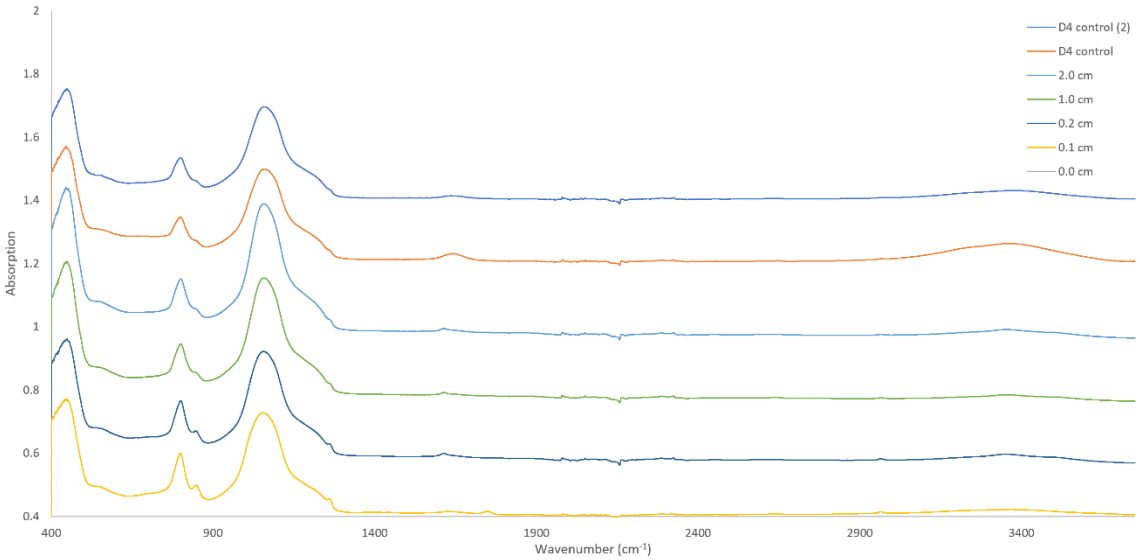

Figure 66: Compiled Fourier-transform infrared spectroscopy results of stratified experiment "B4" with coordinating controls "D4".

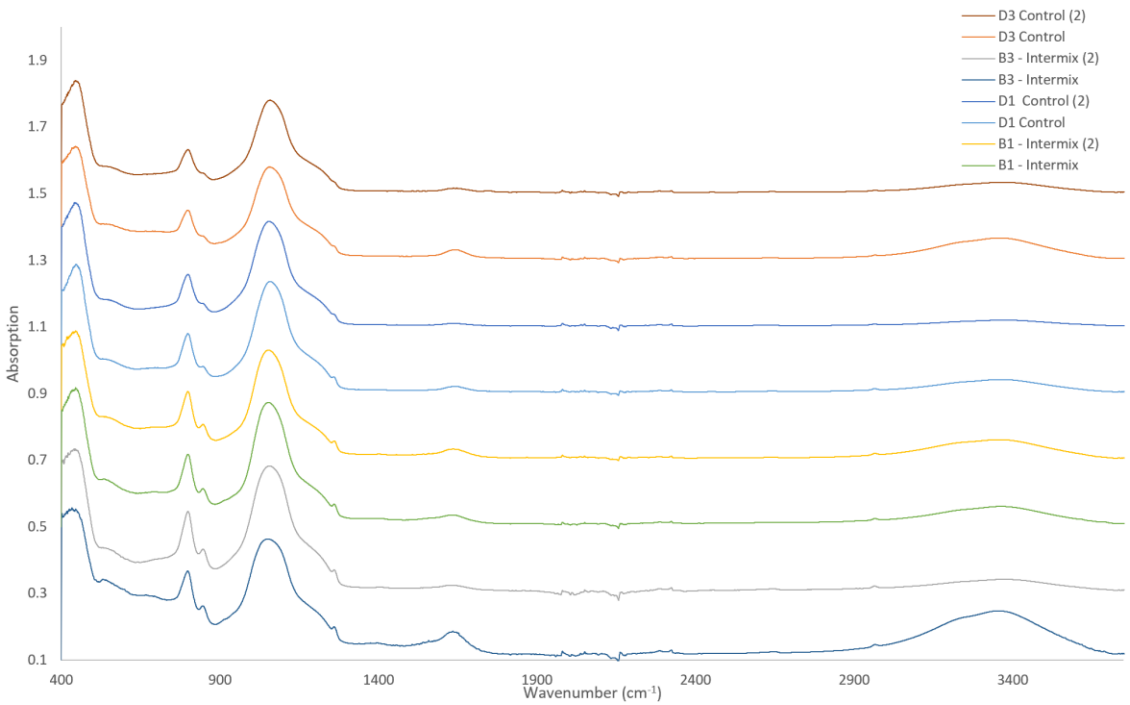

Figure 67: Compiled Fourier-transform infrared spectroscopy results of intermixed experiments “B1” and “B3” with coordinating controls “D1” and “D3”.

APPENDIX H

X-RAY DIFFRACTOGRAMS OF HUMIC ACID EXPERIMENTS

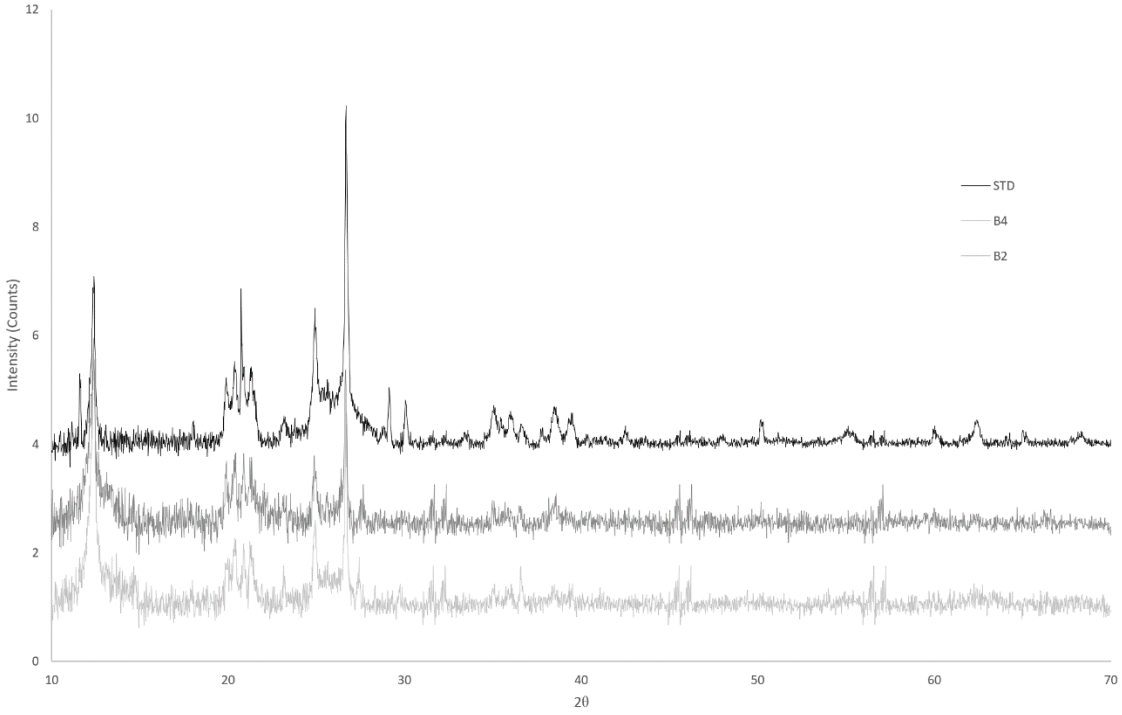

Figure 68: Compiled X-ray diffraction results of humic acid standard and humic acid from stratified experiments “B2” and “B4”.

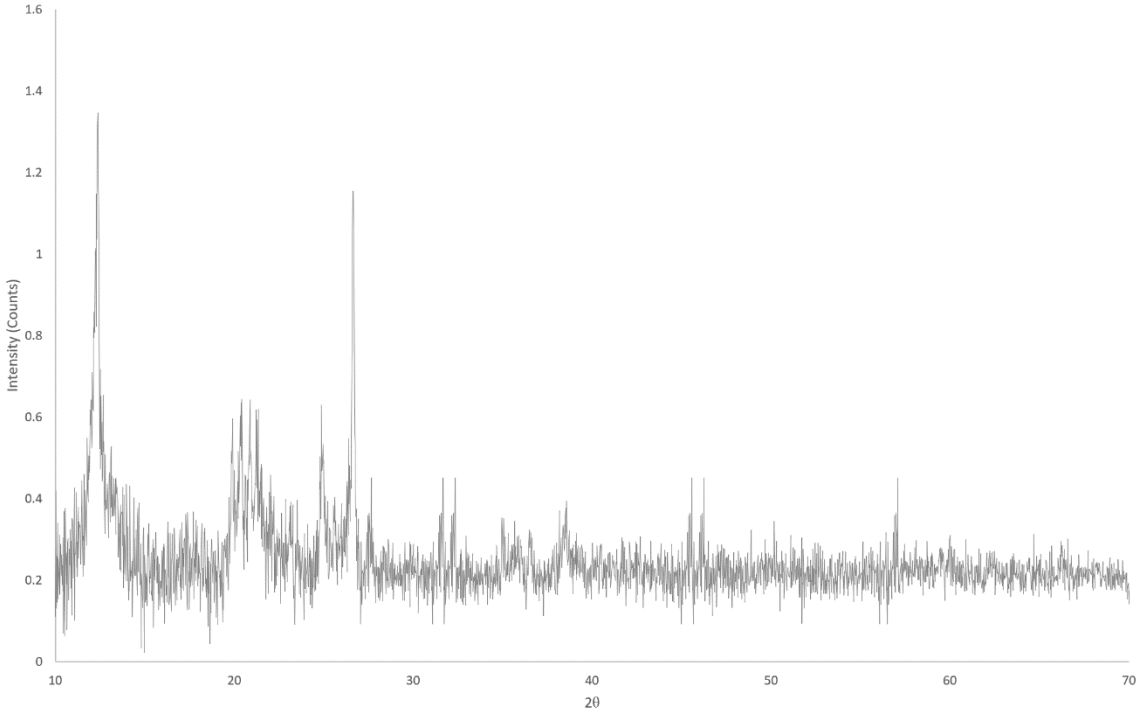

Figure 69: X-ray diffraction results of humic acid from stratified experiments “B2”.

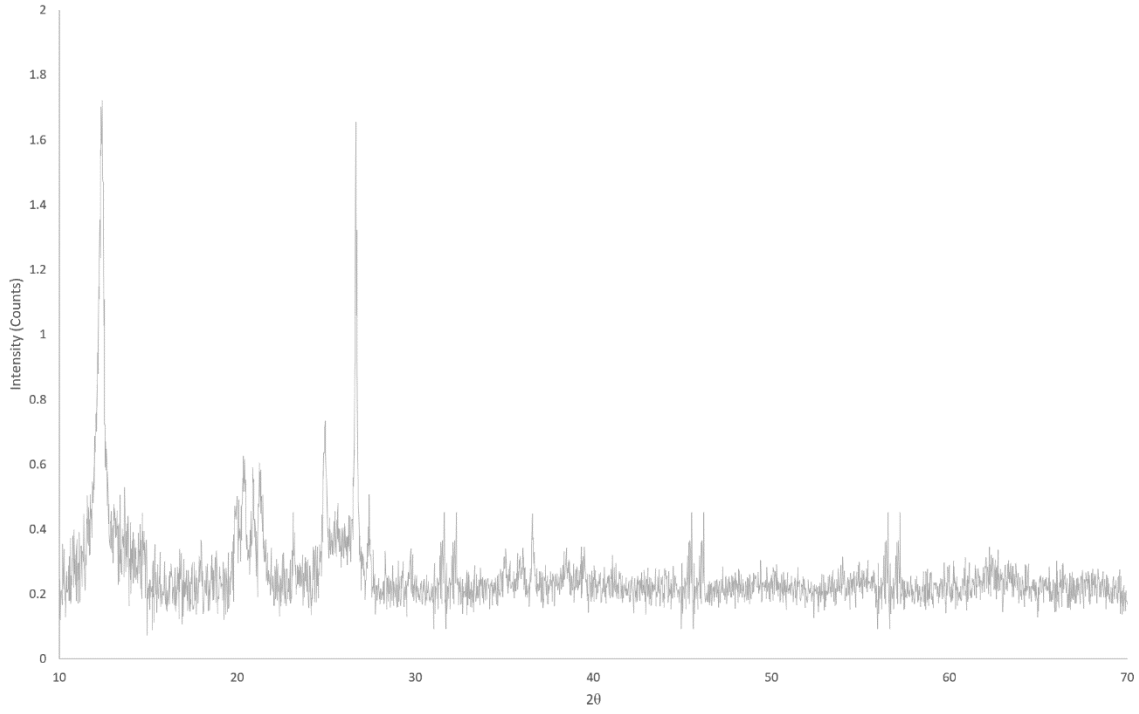

Figure 70: X-ray diffraction results of humic acid from stratified experiments “B4”.

APPENDIX I

FOURIER-TRANSFORM INFRARED SPECTROSCOPY RESULTS OF HUMIC ACID EXPERIMENTS

Figure 71: Compiled Fourier-transform infrared spectroscopy of humic acid standard and humic acid from stratified experiments "B2" and "B4".

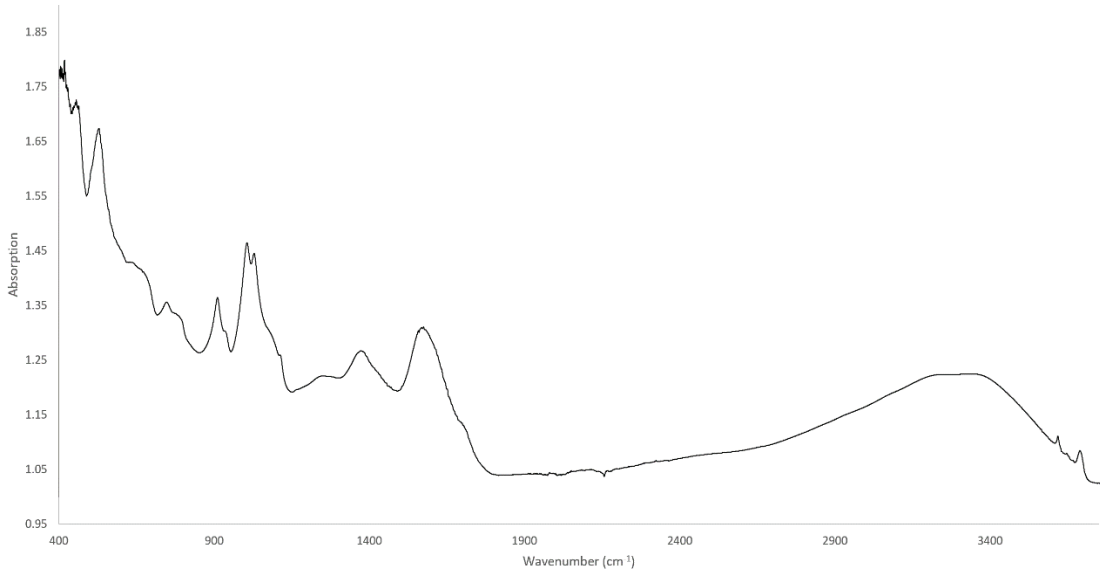

Figure 72: Fourier-transform infrared spectroscopy of humic acid standard.

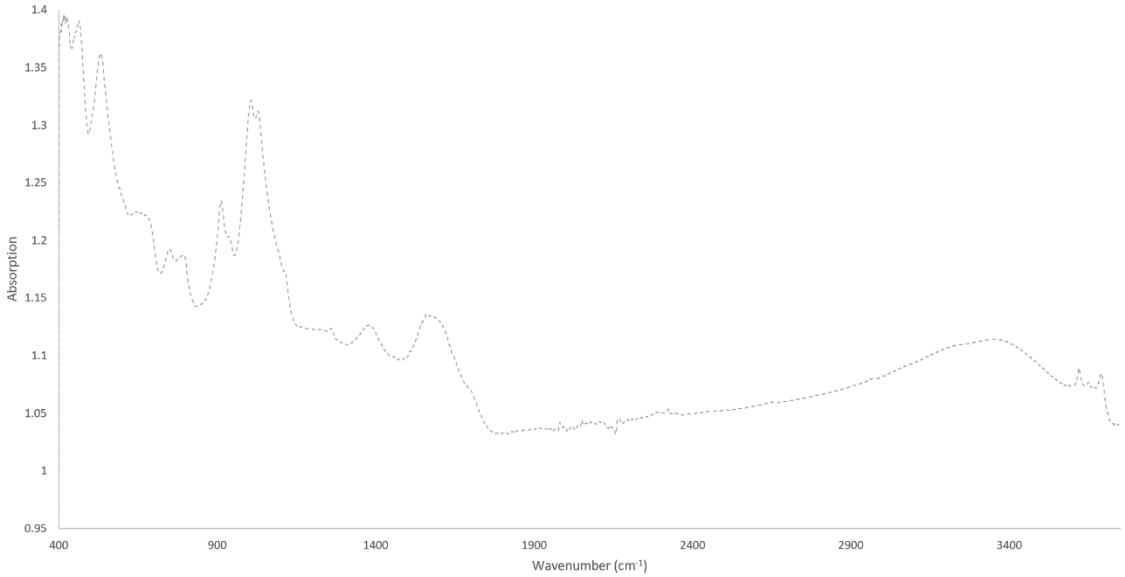

Figure 73: Fourier-transform infrared spectroscopy of humic acid from stratified experiment “B2”.

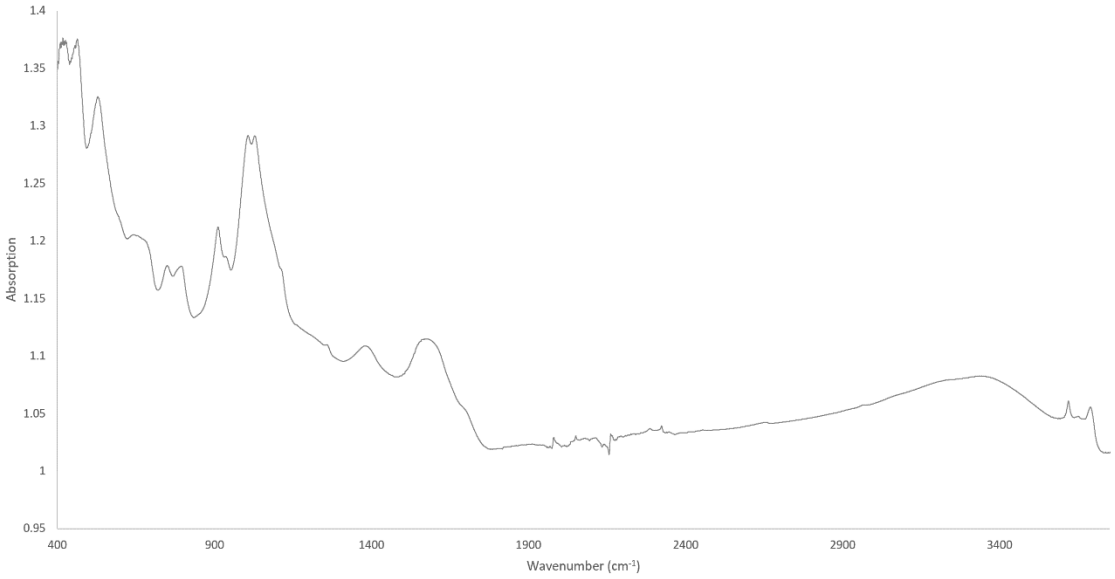

Figure 74: Fourier-transform infrared spectroscopy of humic acid from stratified experiment “B4”.